Non-equilibrium Dynamics and Quantum Magnetism in 1D Optical Lattices

Von der Fakultät für Mathematik und Physik der
Gottfried Wilhelm Leibniz Universität Hannover

zur Erlangung des Grades

**Doktorin der Naturwissenschaften
Dr. rer. nat.**

genehmigte Dissertation von
M.Sc. Karen Rodríguez

geboren am 01. November 1980 in Bogotá, Kolumbien

2011

Referent   : Prof. Dr. Luis Santos
Korreferent   : Prof. Dr. Temo Vekua
Tag der Promotion   : 25.01.2011

To Arturo

Abstract

In this Thesis we examine the properties of ultra-cold strongly-correlated quantum gases in optical lattices. Nowadays, spectacular progresses allow for an unprecedented degree of control of interparticle interactions, dimensionality, doping, disorder, etc., which permit the detailed analysis of many-body phenomena as e.g. the realization of the superfluid to Mott insulator transition in bosonic lattice gases [1], the 3D fermionic Mott insulator [2, 3] or the Tonks gas [4]. These advances make strongly-correlated gases an extraordinary scenario for the study of condensed matter physics, quantum optics, and quantum information. Cold lattice gases are often proposed as quantum simulators mimicking, for instance, the Hubbard and Heisenberg models. In this Thesis, we analyze, by means of numerical and analytical methods, relevant topics related to the dynamics and ground-state properties of lattice gases. This Thesis can be divided in two parts.

Non integrable systems out-of-equilibrium constitute an interesting field recently opened by the possibilities offered by cold gases. We concentrate, in Part I, on the correlation-dynamics of one-dimensional Bose gases with strong interactions loaded in one-dimensional time-dependent optical lattices. We show that the evolution is characterized by a transient non-equilibrium state in which quasi-local correlation functions have already converged into a new equilibrium whereas long-range correlations and the quasi-condensate fraction present still a significant time dependence. Additionally, we have analyzed the formation at a longer time scale of a new equilibrium from an initial gas at zero temperature. We also address the issue of adiabaticity by considering the fidelity with respect to the ground state of the final configuration, we have shown that even rather mild ramps do not fully guarantee a perfect loading of the new ground state.

Spinor gases, formed by particles with various available Zeeman substates, constitute an ideal system for investigating the interplay between external and internal (spin) degrees of freedom. As a result of this interplay, the ground state physics of spinor lattice gases is very rich, providing novel scenarios for quantum magnetism, which we study in this Thesis in Part II.

In particular, we analyze the influence of the quadratic Zeeman coupling (QZE) of repulsively interacting spin-3/2 fermions and spin-1 bosons. We concentrate on the hard-core Mott regime (one particle per site) and thus the problems reduce to the analysis of low-energy effective spin Hamiltonians with super-exchange interactions.

Spin-3/2 fermions are the smallest spin fermionic systems that exhibit, in the hard-core regime, spin-changing collisions and hence sensitivity against a quadratic Zeeman coupling whose crucial role must be taken into account

for the study of high spins systems. In spite of its experimental relevance, the quadratic field is mostly ignored in the analysis of the magnetic properties. We study the Mott insulator phase diagram for spin-3/2 fermions as a function of the spin-changing collisions and the QZE. We have shown that the external field preserves an SU(2) $\otimes$ SU(2) symmetry and for large enough fields the ground state of the system is an isotropic Heisenberg antiferromagnetic (IHAFM) phase. Moreover, tuning the quadratic field to lower values the system undergoes, depending on the scattering lengths, either a Kosterlitz-Thouless transition into a gapped dimerized (spin Peierls) phase or a commensurate-incommensurate transition into a gapless spin liquid phase. The rich resulting phase diagram can be observed experimentally in four-component fermions in optical lattices under similar entropy constraints to those required for Néel order in spin-1/2 gases.

Furthermore, we analyze field-induced phase transitions of spin-1 lattice bosons for both ferromagnetic and antiferromagnetic interactions. We show that for a large enough negative QZE the system is in a large-D (polar) phase. By increasing the QZE but keeping it sign, the system undergoes in the ferromagnetic regime a Kosterlitz-Thouless transition into a XY-ferromagnet phase. Further increasing to positive values, the system undergoes a first-order phase transition into a fully polarized Ising-ferromagnet. In the antiferromagnetic regime, starting in the large-D phase, and modifying the QZE the system enters a dimerized phase via an Ising transition or, advancing towards positive fields, a XY-nematic phase through a Kosterlitz-Thouless transition. We have performed 1D numerical simulations to determine the nature and the precise location of the phase transitions. Our numerical results are in excellent quantitative agreement with analytical predictions retrieved from an effective field theory description. The obtained phase diagram can be studied in experiments with e.g. ultra-cold Rb and Na atoms in optical lattices.

Keywords: Ultracold Quatum Gases, Spinor gases, Quantum Magnetism.

Zusammenfassung

Diese Arbeit untersuchen werden die Eigenschaften ultrakalter stark korrelierter Quantengase in optischen Gittern untersucht. Durch bahnbrechende Fortschritte ist es heutzutage möglich, im Experiment Eigenschaften eines Vielteilchensystems zu kontrollieren. So können z. B. die Wechselwirkungen zwischen Teilchen, die Dimensionalität des Systems und die Unordnung präzise eingestellt werden. In den letzten Jahren wurden so Vielteilchen-Phänomene wie der Übergung vom Superfluid zum Mott-Isolator in bosonischen Gittergasen [1], der 3D fermionische Mott-Isolator [2, 3] und das Tonks-Gas [4] beobachtet und analysiert. Somit können mit Experimenten an stark korrelierten Gasen Fragestellungen der Festkörperphysik, der Quantenoptik und der Quanteninformation untersucht werden. Kalte Gittergase wurden auch als Quantensimulatoren vorgeschlagen, die z. B. das Hubbard- und das Heisenberg-Modell simulieren. In dieser Arbeit untersuchen wir mit Hilfe numerischer und analytischer Methoden Fragestellungen der Dynamik und der Eigenschaften des Grundzustandes von Gittergasen. Die Arbeit gliedert sich in zwei Teile.

Nichtintegrable Systeme fern vom Gleichgewicht sind ein Forschungsgebiet, welches durch neue Experimente an kalten Gasen vorangebracht wurde. Im ersten Teil der Arbeit untersuchen wir die Dynamik der Korrelationen in eindimensionalen stark wechselwirkenden Bosegasen in 1D zeitabhängigen optischen Gittern. Es wird gezeigt, dass die Dynamik durch einen transienten Nichtgleichgewichtszustand charakterisiert wird. In diesem Zustand sind die quasilokalen Korrelationen bereits zum Gleichgewicht konvergiert, während langreichweitige Korrelationen und der Anteil des Quasikondensats immer noch zeitabhängig sind. Darüberhinaus untersuchen wir die Bildung eines neuen Gleichgewichtszustandes auf gröeren Zeitskalen von einem Anfangszustand bei Temeratur Null aus. Wir diskutieren die Frage der Adiabazität durch Angabe der Fidelität bezüglich des Grundzustandes der Endkonfiguration und zeigen, dass selbst langsame Potentialrampen ein perfektes Einsetzen des neuen Grundzustandes nicht grantieren.

Spinorgase, die aus Teilchen mit mehreren Zeeman-Niveaus bestehen, sind ein ideales System zur Untersuchung der Wechselwirkungen zwischen äueren und inneren (Spin) Freiheitsgraden. Diese Wechselwirkungen liefern eine reichhaltige Physik bei den Grundzuständen. Im zweiten Teil der Arbeit untersuchen wir neue Szenarios für den Quantenmagnetismus in diesen Systemen. Der Einfluss des quadratischen Zeemaneffektes (QZE) bei abstoend wechselwirkenden Spin-3/2 Fermionen und Spin-1 Bosonen wird behandelt. Wir untersuchen hauptsächlich das Mott Regime mit hard-core Wechselwirkung (ein Teilchen pro Gitterplatz), so dass die Probleme sich auf die Analyse von effektiven Modellen reduzieren.

Spin-3/2 Fermionen sind die kleinsten fermionischen Systeme, die bei hard-core Wechselwirkungen Spinflips zulassen. Somit sind sie auch vom quadratischen Zeemaneffekt abhängig, dessen Rolle bei der Untersuchung von Systemen mit hohen Spin berücksichtigt werden muss. Obwohl der quadratische Zeemaneffekt experimentell relevant ist, wird er meist bei der Analyse magnetischer Eigenschaften ignoriert. Wir untersuchen das Phasendiagramm der Mott-Isolator Phase für Spin 3/2-Fermionen in Abhängigkeit von spinändernder Streuung und vom QZE. Es wird gezeigt, dass das externe Feld die SU(2) ⊗ SU(2) Symmetrie bei groen Feldern erhält; der Grundzustand des Systems ist ein Heisenberg Antiferromagnet. Bei kleineren Feldern hat das System, abhängig von den Streulängen, einen Kosterlitz-Thouless Phasenübergang in eine dimerisierte (Spin Peierls) Phase bzw. einen Phasenübergang zu einer Spin-Liquid-Phase vom commensurate-incommensurate Typ. Das resultierende Phasendiagramm kann experimentell in vier-Komponenten Fermionen in optischen Gittern beobachtet werden, unter ähnlichen Bedingungen an die Entropie wie bei der Néel-Ordnung bei Spin-1/2 Gasen.

Weiterhin untersuchen wir feldinduzierte Phasenübergänge von Spin-1 Gitterbosonen für ferromagnetische und antiferromagnetische Wechselwirkungen. Wir zeigen, dass für groe negative QZE das System in einer polaren Phase ist. Bei Vergöerung des quadratischen Zeemaneffektes findet im ferromagnetischen Regime ein Phasenübergang vom Kosterlitz-Thouless Typ in eine XY-Phase statt. Bei positiven Werten des QZE geht das System in eine dimerisierte Phase über (Übergang vom Ising Typ) bzw. wieder in eine nematische XY-Phase. Unsere eindimensionalen numerischen Simulationen konnten den Typ und die genaue Stelle der Phasenübergänge aufzeigen. Diese Ergebnisse sind in guter quantitativer Übereinstimmung mit analytischen Vorhersagen aus Beschreibungen durch effektive Feldtheorien. Das Phasendiegramm kann experimentell z. B. an ultrakalten Rb und Na Atomen studiert werden.

Schlagwörter: Ultrakalte Quantengase, Spinorgase, Quantenmagnetismus.

Contents

Introduction

In this Thesis, we focus our interest in both bosonic and fermionic particles in the quantum degenerate regime. Before getting into the main core of the present work, it is important to establish a framework reviewing some relevant experimental and theoretical results which could serve as an introduction and stimulate further reading. We concentrate on the achievements reached in the ultra-cold atoms experiments due to the implementation of the optical lattices. These lattices provide a novel realization of strongly correlated quantum systems, since they are suitable to simulate conventional condensed matter problems under extremely well-controlled conditions. The reason is the large degree of tunability of almost all the system parameters such as the potential, interactions, absence of disorder and doping, to mention only a few. Thus, besides the intrinsic interest in these systems, they are often proposed as quantum simulators. The most important example in this respect is mimicking the Hubbard model, allowing researchers to explore its relevance for high-temperature superconductivity, for instance. The reduction from Hubbard to Heisenberg model performing perturbation analysis is a very common tool in the studies of discrete quantum systems, such as spin chains. We study both Hubbard and Heisenberg models, and therefore they are reviewed in this introduction. In Chapter 2 we describe the numerical tools employed throughout the present work. In Chapter 3, the Hubbard model is used for the description of a cold atomic Bose gas loaded on a time-dependent optical lattice. Furthermore, we discuss the correlation dynamics of the strongly-correlated one-dimensional superfluid besides adiabaticity concerns.

Particles with hyperfine states also play a crucial role in the understanding of condensed matter systems such as the magnetically-ordered phases in low-dimensions. Those problems are the object of study in Chapters 4 and 5 regarding fermionic particles and subsequently Chapter 6 for bosons.

1.1 Quantum degenerate gases

Trapped atomic gases at very low temperatures became, in the past years, a center of attention in quantum optics, atomic and condensed matter physics. The greatest achievement has been the Bose-Einstein condensation (BEC) [5–9]. This phenomenon was predicted in 1924-25 [10, 11] and was observed in 1995, for the first time, in a series of experiments on dilute vapors of alkali

atoms cooled down to extremely low temperatures (a few nanokelvins) [12–14]. In such experiments the anisotropic expansion of the gas revealed the importance of the interparticle interaction. The BEC can be described theoretically, for the weakly interacting regime, within the framework of the Gross-Pitaevskii equation and the Bogoliubov theory [8, 9]. Due to the big impact of the BEC achievement, the Nobel prize was awarded to the pioneering groups in 2001 [15, 16].

Soon after the realization of the BEC, Fermi gases were in the focus of high interest for experimentalists and theoreticians. However, the achievement of Fermi degeneracy was delayed due to the difficulties to reach low enough temperatures. In 1999 quantum degeneracy in trapped Fermi gases was achieved [17–19].

Creation of BECs. Bose-Einstein condensates of alkali atoms are produced in a multistage process involving laser cooling, trapping and evaporative cooling in a magnetic trap. A thermal atomic beam escapes from an oven and is trapped and pre-cooled in a magneto-optical trap (MOT) using the laser cooling technique. In this technique atoms are shined with three pairs of counter-propagating laser beams, which are slightly red-detuned for a particular atomic absorption line. Atoms moving in any direction at the intersection of the laser beams see the light blue-shifted into the resonance, so that, they absorb a photon in that direction slowing down their motion due to momentum conservation. The further emission of the absorbed photon occurs in a random direction and averages to zero momentum change. In such way, the cloud is cooled down to around μK. The recoil energy of the emitted photon limits the further reduction of the temperature. In the next stage, the atoms are collected at the center of a weak quadrupole magnetic field and further cooled using evaporative cooling techniques. Resonant radio frequency radiation from a small coil inside a vacuum chamber is used to couple the hottest atoms to untrapped sublevels that are expelled from the trap, while the remaining atoms rethermalize at a lower temperature via collisions. Temperatures of the order of nanokelvins are achieved in this case. Note that at the temperatures required to observe the BEC, the equilibrium configuration of the system is a solid phase. However, in the experiments, the ultra-cold gases are preserved in a metastable phase due to its very dilute character, which makes the three-body losses rare events.

Reaching Fermi degeneracy. After degenerate bosons were observed, it naturally followed an interest on studying fermions in the degenerate regime. As it was pointed out, collisions between atoms are necessary to redistribute the energy in the gas while the hottest atoms of the cloud are escaping. This method fails for fermions because they, unlike bosons, obey the Pauli-exclusion
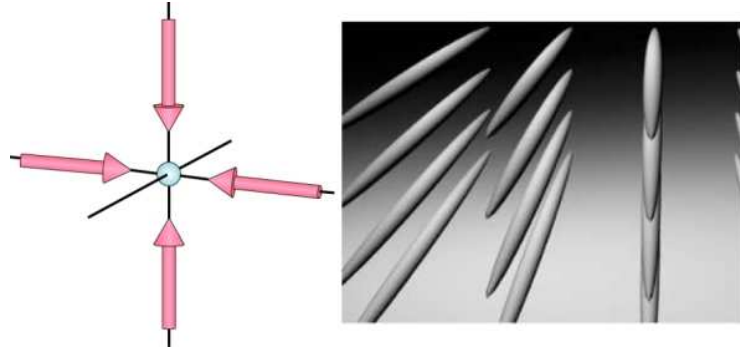
FIGURE 1.1: Two dimensional optical lattice potentials formed by superimposing two orthogonal standing waves. For this configuration, the atoms are confined to an array of tightly confining 1D potential tubes.

principle. This prevents them to occupy the same quantum state, therefore the lack of collisions disrupts the evaporative cooling for fermionic gases. One solution to it is to make the fermions distinguishable. For instance, preparing them into different internal states using the spin degrees of freedom. Another solution is to place the fermionic cloud in contact with a refrigerating colder cloud. This is done by cooling two atomic species, one bosonic and one fermionic, simultaneously. The bosons are evaporatively cooled to very low temperatures and, while they keep colliding with the fermions, the two gases remain in thermal contact. Then, as the temperature of the bosons drops so does the temperature of the fermions. This form of cooling is known as sympathetic cooling and has been used to create dual BECs [20] and also quantum degenerate boson/fermion mixtures [21–23].

1.1.1   Ultra-cold gases in optical lattices

In the following, we discuss the implications of confining cold atoms by laser light into configurations of a reduced dimensionality or in periodic lattices, thus enhancing the effects of interactions. In this way, the regime of strong interactions has become experimentally accessible [24–26], leading to a variety of strongly correlated states of matter. From the many-body point of view this is a more sophisticated regime, since interaction-induced many-body effects have to be taken into account. Strongly-correlated atomic gases in optical lattices constitute one of the most active fields in the physics of ultra-cold gases. Nowadays, spectacular progresses allow for an unprecedented degree of control of interactions between atoms, dimensionality, doping, disorder, etc., which permit the detailed analysis of many-body phenomena [27, 28].

Optical lattices. A periodic potential is generated by overlapping two counterpropagating laser beams. Due to the interference between the two laser beams, an optical standing wave with period $\lambda/2$ is formed with λ the

wavelength of the laser light. In this standing wave the atoms can be trapped. More generally, by choosing the two laser beams to interfere under an angle different from 180°, it is also possible to realize periodic potentials with larger period [29, 30]. Nowadays, using different laser arrangements one, two and three dimensional geometries are experimentally available. In particular two orthogonal optical standing waves create an array of one-dimensional (1D) potential tubes (see Fig. 1.1). In this array the atoms can only move along the weakly confining axis of the potential tube, thus showing effectively a 1D quantum behavior, since the radial motion is completely frozen for low-enough temperatures. For typical experimental parameters, the harmonic trapping frequencies along the tube are very weak on the order of $10 - 100$ Hz, while in the radial direction the trapping frequencies can become as high as up to 100 kHz. In this manner, it is possible to realize quantum wires with neutral atoms, which allow the study of strongly correlated gases in one dimension [4, 31–34].

The presence of the lattice leads to Hubbard-type models [35]. Atomic physics provides a whole toolbox to engineer various types of Hamiltonians for 1D, 2D and 3D Bose and Fermi systems, as we will see below.

1.2 The Hubbard model

The Hubbard model [36], that describes strongly correlated systems, is of great physical interest. From the condensed-matter point of view, high-temperature superconductivity, for example, can be described by the 2D repulsive Hubbard model near the half-filled band [37]. Since fermions, and consequently the Fermi-Hubbard model (FHM) are the main topic in Chapters 4 and 5, let us, in this introductory part, concentrate in the Bose-Hubbard model (BHM) studying its derivation, characteristics and ground state phases.

The starting point is the Hamiltonian operator for bosonic atoms in an external trapping potential

$$
\begin{aligned}
\hat{H} = \int d^3x \; \hat{\psi}^\dagger(\vec{x}) \left(-\frac{\hbar^2}{2m}\vec{\nabla}^2 + V_0(\vec{x}) + V_T(\vec{x}) \right) \hat{\psi}(\vec{x}) \\
+\frac{1}{2} \, \frac{4\pi a_s \hbar^2}{m} \int d^3x \; \hat{\psi}^\dagger(\vec{x})\hat{\psi}^\dagger(\vec{x})\hat{\psi}(\vec{x})\hat{\psi}(\vec{x}),
\end{aligned}
\tag{1.1}
$$

where $\hat{\psi}(\vec{x})$ is the boson field operator, $V_0(\vec{x})$ is the optical lattice potential and $V_T(\vec{x})$ describes an additional slowly varying external trapping potential, see Fig. 1.2. In the simplest case, the optical lattice potential has the form

$$
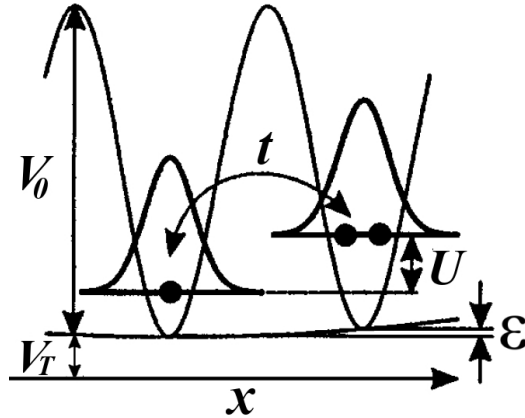V_0(\vec{x}) = \sum_{j=1}^{d} V_0 \sin^2(kx_j),
\tag{1.2}
$$

FIGURE 1.2: Schematic realization of the Hubbard model in an optical lattice. See text and Ref. [35].

where d is the lattice dimension and $k = \frac{2\pi}{\lambda}$ is the lattice wave vector, corresponding to a lattice period $a = \lambda/2$. The lattice depth is given by V_0 which is proportional to the laser intensity. The interaction potential between the atoms is approximated by a short-range pseudopotential with a_s the s-wave scattering length and m the mass of the atoms. At low temperatures, atoms are restricted to the lowest vibrational level at each site. Their kinetic energy is then frozen, except for the small tunneling amplitude to neighboring sites. The associated single-particle eigenstates in the lowest band are Bloch wave functions $\zeta_{\eta\vec{q}}(\vec{x})$. They are characterized by a discrete band index η and a quasimomentum $\vec{q}$ within the first Brillouin zone of the reciprocal lattice [38]. Since Bloch functions are multiplied by a pure phase factor $exp(\imath\vec{q}\cdot\vec{x}_i)$, upon translation by one lattice vector $\vec{x}_i$, they are extended over the whole lattice. An alternative single-particle basis, which is useful for describing the hopping of particles among discrete lattice sites, is provided by the Wannier functions $w_\eta(\vec{x} - \vec{x}_i)$. They are connected with the Bloch functions by a Fourier transform on the lattice

$$\zeta_{\eta,\vec{q}}(\vec{x}) = \sum_{\vec{x}_i} w_\eta(\vec{x} - \vec{x}_i)e^{\imath\vec{q}\cdot\vec{x}_i}. \tag{1.3}$$

Note that, the Wannier functions depend only on the relative distance $\vec{x} - \vec{x}_i$ and, at least for the lowest bands, they are well localized on the individual lattice sites. By choosing a convenient normalization, they obey the orthonormality relation

$$\int d^3x \ w_\eta^*(\vec{x} - \vec{x}_i)w_{\eta'}(\vec{x} - \vec{x}_i') = \delta_{\eta,\eta'}\delta_{\vec{x}_i\vec{x}_i'}. \tag{1.4}$$

We assume that the energies involved in the system are small compared to the excitation energies of the second band. The field operator $\hat{\psi}(\vec{x})$, which destroys a particle at an arbitrary point $\vec{x}$ is expanded in the Wannier basis,

keeping only the lowest vibrational states (we restrict ourselves to the first band $\eta = 1$),

$$\hat{\psi}(\vec{x}) = \sum_i \hat{b}_i w(\vec{x} - \vec{x}_i). \tag{1.5}$$

Thus, the Hamiltonian in Eq. (1.1) reduces to the Bose-Hubbard Hamiltonian,

$$\hat{H} = -t \sum_{\langle i,j \rangle} \hat{b}_i^\dagger \hat{b}_j + \sum_i \epsilon_i \hat{n}_i + \frac{U}{2} \sum_i \hat{n}_i (\hat{n}_i - 1), \tag{1.6}$$

where the operator $\hat{n}_i = \hat{b}_i^\dagger \hat{b}_i$ counts the number of bosons at the lattice site i, the annihilation and creation operators $\hat{b}_i$ and $\hat{b}_i^\dagger$ obey the canonical commutation relations $[\hat{b}_i, \hat{b}_j^\dagger] = \delta_{ij}$. The parameters t, U and ϵ_i are given by

$$
\begin{aligned}
t &= \int d^3x \; w^*(\vec{x} - \vec{x}_i) \left[-\frac{\hbar^2}{2m} \vec{\nabla}^2 + V_0(\vec{x}) \right] w(\vec{x} - \vec{x}_j), \\
U &= \frac{4\pi a_s \hbar^2}{m} \int d^3x \; |w(\vec{x})|^4, \quad \text{and} \\
\epsilon_i &= \int d^3x \; V_T(\vec{x}) |w(\vec{x} - \vec{x}_i)|^2 \approx V_T(\vec{x}_i).
\end{aligned}
\tag{1.7}
$$

The hopping matrix element between adjacent sites i, j is given by t, this term is non-negligible only to nearest neighbors. U corresponds to the strength of the on-site repulsion of two atoms on the lattice site i, and ϵ_i describes an energy offset of each lattice site. Note that in deriving Eq. (1.6) we have neglected additional terms as nearest-neighbor interactions which are typically very small at least in short-range interacting gases.

1.3 The superfluid-Mott insulator transition.

The Bose-Hubbard model describes the competition between the kinetic energy t, which is gained by delocalizing particles over lattice sites, and the repulsive on-site interaction U, which disfavors having more than one particle at any given site. In an optical lattice loaded with cold atoms, the ratio U/t between these two energies can be changed by varying the optical lattice depth.

In order to illustrate the properties of systems described by the Bose-Hubbard Hamiltonian Eq. (1.6), we will discuss important limiting cases. Here we assume a homogeneous system at zero temperature without any potential apart from the periodic lattice (i.e. $\epsilon_i = 0$). Therefore, for a given mean atom number per site $\bar{n}$, the ground state properties of the Hamiltonian are completely determined by the parameters t and U. The existence and properties of the quantum phase transition that the BHM exhibits as a function of U/t,

are well studied. In cold bosonic atoms, the Hubbard model was introduced by Fisher *et al.* [39] to describe the destruction of superfluidity due to strong interactions and disorder.

1.3.1 Superfluid phase.

In the limit, $t \gg U$, the many-body ground state is described by a BEC where all atoms are in the lowest energy single-particle state. That is, the Bloch wave function with zero quasi-momentum, $\vec{q} = 0$. Therefore, the atoms are spread out over the entire lattice, with long-range phase coherence. The ground state wave function is the sum of the Wannier wave functions (1.3) at each lattice site i with constant phase. According to Eq. (1.5) we can write the one particle ground state as $|\psi\rangle = \beta \sum_i \hat{b}_i^\dagger |0\rangle$, where β is a normalization factor. Thus the ground state for N particles on L lattice sites is given by

$$|\psi\rangle_N \propto \frac{1}{\sqrt{L}} \left(\sum_{i=1}^{L} \hat{b}_i^\dagger \right)^N |0\rangle. \tag{1.8}$$

In the limit of large system size, $(L, N \to \infty)$ with constant average occupation number $\bar{n} = \frac{N}{L}$, this state becomes separable into a product of single site states. At each site i, a superposition of Fock states $|m\rangle_i = (\hat{b}_i^\dagger)^m |0\rangle$ with all possible occupations m is present. While the average density is well defined and constant over the lattice, the atom number determined by measuring each individual site is randomly distributed. In this situation the ground state can be expressed as

$$|\psi\rangle = \prod_i |\psi\rangle_i, \tag{1.9}$$

consisting of a product of states $|\hat{\psi}\rangle_i$ for each site i where now $|\psi\rangle_i$ are eigenstates of the $\hat{b}_i$. An appropriate basis is given by the coherent states [40, 41],

$$|\hat{\psi}(\bar{n})\rangle_i = e^{-\frac{|\alpha_i|^2}{2}} \sum_{m=0}^{\infty} \frac{\alpha_i^m}{\sqrt{m!}} |m\rangle_i, \tag{1.10}$$

where α_i denotes the wave function phase and the expectation value of the atom number $\bar{n} = |\alpha_i|^2$ at site i. The atom number distribution of this coherent state follows a Poissonian distribution. Furthermore, this state has a macroscopic phase. It is this macroscopic phase that allows the wave functions from different lattice sites to interfere with each other during time-of-flight (TOF) experiments (see Fig. 1.4) [42]. A possible realization of such a ground state is depicted in Fig. 1.3(a) for an average filling of $\bar{n} = 1$.

The ground state of the system when the on-site interaction is small compared to the tunneling strength is commonly named the *superfluid state.*
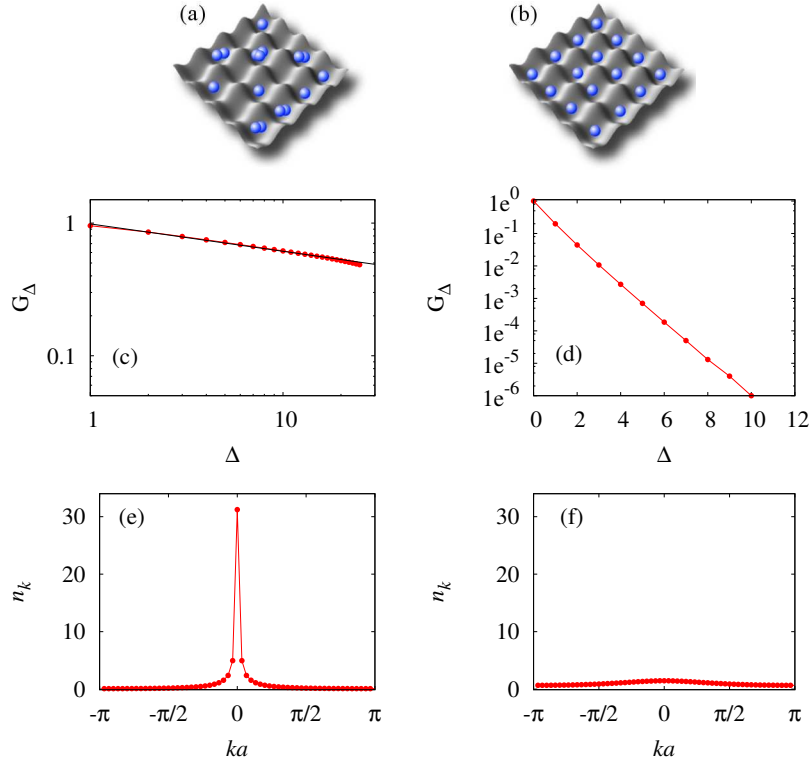
FIGURE 1.3: The two very distinct phases of the BHM at $T = 0$. (a) Sketch of the superfluid state ($U \ll t$) and (b) the Mott-insulating state ($U \gg t$) which has a well-defined occupation number on each site [43], both at averaged filling $\nu = 1$ in a homogeneous system. The single-particle correlation function (G_Δ) decay as a function of the neighbor sites (Δ) is depicted for each phase, (c) the power low decay for the SF regime, the solid line is the fitting to the data, the deviation correspond to finite size effect, and (d) the exponential decay for the MI regime. The momentum distribution profile (n_k) as a function of the dimensionless ka shows (e) the characteristic sharp peak of the SF and (f) the flat profile of the MI.

When the interaction becomes more important there is a disagreement between the "true" ground state and the coherent states, which is due to the growth of a long-range correlations across the system.

In the following, we concentrate in the case of a 1D lattice. In 1D the SF is characterized by a quasi-long-range correlation reflected in an algebraic decay of the off-diagonal elements of the single-particle density matrix with the distance, see Fig. 1.3(c). In the following we discuss in more details the single-particle correlation function(Eq. (1.11)).

The single-particle correlation function (SPCF)   or Green's function
is defined by

$$G_\Delta = \langle \hat{b}_i^\dagger \hat{b}_{i+\Delta} \rangle, \tag{1.11}$$

where the angular brackets denote averaging over the physical ground state.
The creation operator is taken at the site i and the annihilation operator is
acting in the $(i + \Delta)$-neighbor site. If G_Δ decreases very fast with distance,
then faraway points are relatively uncorrelated and the system is dominated
by its microscopic structure and short-ranged forces. On the other hand, a
slow decrease of G_Δ would imply that faraway points have a large degree of
correlation or influence on each other. The system thus becomes organized
at a macroscopic level with the possibility of a new structure beyond the
obvious one dictated by the short-ranged microscopic forces. This is the case
of the gapless superfluid phase where the SPCF decays with a power-law
behavior [44]

$$\langle \hat{b}_i^\dagger \hat{b}_{i+\Delta} \rangle \sim \Delta^{-K/2}, \tag{1.12}$$

where K is the so-called Luttinger liquid parameter. It is usual to examine
the natural orbitals, $\vec{\phi}^\nu$, which are the eigenfuntions of the SPCF and are
considered as the effective single-particle states in interacting systems [45],

$$\sum_{\Delta=i}^{N-1} G_{i,i+\Delta}(x,t)\phi_{i+\Delta}^\nu(x,t) = \lambda_\nu(x,t)\phi_i^\nu(x,t), \tag{1.13}$$

where λ_ν are the occupations. In dilute high dimensional gases, the large
occupation of the lowest natural orbital is regarded as the condensate fraction
$\lambda_0 = n_0/n$ and in fact it is the BEC order parameter which drops continuously
from 1 at $t/U \gg 1$ to zero at $(t/U)_c$. Thus, for a finite and low dimensional
system, it is defined the quasi-condensate fraction as the largest eigenvalue
λ_0, since strictly speaking there is no condensation in 1D at zero-temperature.
As a signal of quasi-condensation one can observe the emergence of a sharp
peak in the momentum distribution profile like the one observed in Fig. 1.3(e).
This is in contrast to the Mott-insulating phase, discussed below, where the
momentum distribution profile is rather flat, see Fig. 1.3(f).

1.3.2   Mott-insulator phase.

For $t/U \sim 0$, on the other hand, delocalization cannot compensate the on-site
repulsion. Therefore, the system arranges in a way to minimize the interaction
energy. This can be achieved by forming localized states at each lattice site
with a well defined number of particles, i.e. Fock or number states $|m\rangle$. The
wave function can be expressed as a product of the form $|\psi\rangle = \prod_i |m\rangle_i$,
where the atom number on each site i is exactly m. In this way, one can
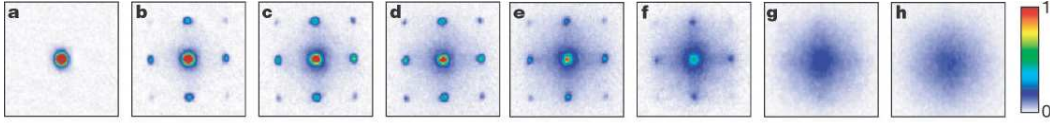
FIGURE 1.4: Momentum distribution of the atoms in the quantum phase transition from SF where interference patterns in absorption images appear to MI where no interference is seen. The depth of the potential wells in the lattice is systematically increased from 0 at (a) to $20E_r$ at (h), where E_r is the recoil energy. The phase transition occurs between (f) and (g). See Ref. [1].

use the criterion that the particle-number variance vanishes, i.e. $(\Delta\hat{n})^2 = \sum_i \langle \hat{n}_i - \bar{n} \rangle^2 = 0$, since both the particle-number and its variance are accessible to measure in experiments.

The phase is also incompressible in the general case of $U \gg t$. The incompressibility implies that the average density remains unchanged when the chemical potential μ is varied, $\partial \bar{n}/\partial \mu = 0$, this defining property is very accurate [28]. This many-body state of the system is known as *Mott-insulator state* (MI). In the homogeneous system for an average filling of $\bar{n} = 1$ the state is a uniform array with exactly one atom per lattice site, this configuration can be seen in Fig. 1.3(b). This phase has been experimentally observed for both ultra-cold bosonic and fermionic gases [2, 3, 31].

With a fixed atom number per site in the Mott insulator state its conjugate variable, which is the phase of the wave function on each site, has the maximum uncertainty. Phase coherence between lattice sites is hence lost, so no interference can occur between the matter waves released from these sites in a TOF experiment [42]. This is in strong contrast to the superfluid case where the phase is well-defined throughout the whole ensemble. Another interesting feature of this gapped Mott-insulator phase in finite systems is the fact that the single-particle correlation function decreases extremely fast with the distance between sites, G_Δ decays exponentially (see Fig. 1.3(d)), therefore there is no correlation among faraway points as was already commented.

Following the proposal in Ref. [35], the SF-MI quantum phase transition was first observed by Greiner *et al.* [1]. In this experiment, they induced the transition in a repulsively interacting BEC held in a three-dimensional optical lattice. As the potential depth of the lattice is increased, the transition is observed from the SF, at very shallow lattice, to the MI phase, where tunneling is suppressed at very deep lattice, see Fig. 1.4. Lately, this phase transition was observed experimentally in 1D lattices by Stöferle *et al.* [46] and two-dimensions by Spielman *et al.* [47].
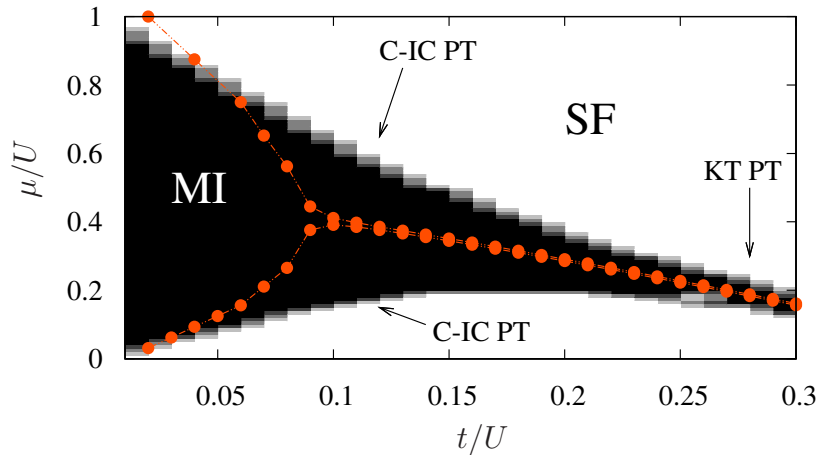
FIGURE 1.5: Phase-space diagram μ/U vs t/U, showing the first Mott-insulator lobe (MI) with $\langle \hat{n} \rangle = 1$ (black region) surrounded by the superfluid phase (SF). The calculations were performed using MPS ansatz (density plot), see Chap. 2 and mean-field Gutzwiller ansatz (circles), see text.

1.3.3 Phase-diagram for the SF-MI transition

The precisely controlled depth of the periodic optical potential by the intensity of the laser beams allows for varying the ratio t/U over a wide range of values in an experiment. This offers the opportunity to adiabatically transfer an initially delocalized BEC into the Mott-insulating state passing through the intermediate interaction regime. Therefore, scanning all the possible paths between these two regimes one obtains the zero-temperature phase diagram of the homogeneous BHM. This diagram is shown in Fig. 1.5, where the density is controlled by the chemical potential μ/U as a function of t/U. There are two different SF-MI transitions: (i) the commensurate-incommensurate (C-IC) phase transition (PT) and (ii) the Kosterlitz-Thouless (KT) PT at commensurate densities.

The commensurate-incommensurate phase transition. On most of the phase transition lines the density of the system changes. Since, those lines mark the boundary between the incompressible insulator and the compressible superfluid. This is a clear example of the commensurate-incommensurate transition and the location of this density transition can be directly determined as the energy it takes to add a particle or a hole to the insulator [44]:

$$\mu_c^p = E^p - E_0 \quad \text{and} \quad -\mu_c^h = E^h - E_0, \tag{1.14}$$

where E_0 is the energy of the Mott insulator ground state, E^p (E^h) is the energy of a state with the density of the ground state and an additional

particle (hole). Note that the chemical potentials μ_c^p and μ_c^h are not equal, nonetheless, those ground-state energies can be calculated using the matrix product states (MPS) method which will be discussed in Chapter 2.

The Kosterlitz-Thouless phase transition. At the phase transition where the density remains integer, the model belongs to the universality class of the $(d + 1)$-dimensional XY-model [39], and there is a Kosterlitz-Thouless [48, 49] phase transition. This transition is purely driven by phase fluctuations that are determined by the hopping t. In principle the Kosterlitz-Thouless transition could be found by locating the t at which $\mu_c^p = \mu_c^h$. But since the particle-hole excitation gap closes exponentially fast, small errors in the energies lead to a big error in the experimental or theoretical location of the critical point t_c. This is usually the case of the KT phase transition, for which the phase boundaries and critical points are very difficult to determine. Instead in this case, one can take the advantage that the SF-MI transition is associated with the loss of long-range order in the SPCF. Therefore, it is much better to study the change in the decay of the correlation functions to find not only the critical point at the tip but also obtain the whole shape the Mott-lobes.

In general, the Kosterlitz-Thouless transition does not correspond to any "conventional" quantum critical behavior (as in the SF phase) and the corresponding power laws are not always possible to visualize near the vicinity of the transition point. The correlation functions behave smoothly and the finite size effects (in lattices for instance) are severe. Connected to that, the Kosterlitz-Thouless transition does not yield a singularity in any derivative of the order parameter at the transition, and therefore it is usually called an infinite-order transition.

The Gutzwiller ansatz. To study the many-body physics of the BHM, one can use the Gutzwiller ansatz, which is a variational method based on the product state [50]

$$|\Psi_{GW}\rangle = \prod_i \sum_l \frac{f(l)}{\sqrt{l!}} \left(\hat{b}_i^\dagger\right)^l |0\rangle. \tag{1.15}$$

We minimize the expectation value of the free energy, $\hat{F} = \hat{H} - \mu\hat{n}$, with respect to the variational values $f(l)$, with l running over the internal states per site, under the constrain of fixed norm $\sum_l |f(l)|^2 = 1$. Following this procedure, one obtain the phase diagram μ/U vs t/U of Fig. 1.5(circles). To keep it simpler, we have set $U := 1$ as unit of energy.

In spite of the fact that the variational approach is a simple and well established technique, its application to the SF-MI transition turns out to be not accurate enough for 1D systems. This method is not appropriate to describe the transition in both fermionic and bosonic cases [50, 51]. This wave function

is mean-field in nature because it does not include long-range correlations. In fact, for the fermionic Hubbard model, the optimal $|\Psi_{GW}\rangle$ is never insulating, except at $U = \infty$, even if the variational wave function is improved by adding short-range density-density correlations. In the case of spinless bosons, and insulating $|\Psi_{GW}\rangle$ can be stabilized at finite U, but as it is shown in Fig. 1.5, the insulator obtained in this way gives an incorrect description of the actual ground state. Therefore, it is needed another numerical tool to calculate the real ground-state of the model in 1D like the MPS. Here it is worth to comment that this method is widely used in 2D and 3D where the quantum fluctuations are not that strong and mean-field approaches work much better than in 1D.

1.4 Strongly-correlated quantum magnetism

On-going experiments [52, 53] are approaching the regime at which magnetic properties, including the long-pursued Neél antiferromagnet in spin-1/2 fermions, could be revealed. Optically trapped spinor gases, formed by atoms with various Zeeman substates, result in an exceedingly rich physics and are particularly interesting since they provide unique possibilities for the analysis of quantum magnetism.

Quantum magnets are spin systems in which the spins interact via an exchange interaction. The interaction is purely quantum mechanical in nature and its form was derived by Heisenberg and Dirac [54]. The most well-known model of interacting spins, in an insulating solid with a hypercubic d-dimensional lattice, is the Heisenberg model with the Hamiltonian

$$\hat{H} = \sum_{<ij>} J_{ij}\vec{S}_i \cdot \vec{S}_j, \tag{1.16}$$

where $\vec{S}_i$ is the spin operator located at the lattice site i and can have a magnitude $1/2, 1, 3/2, 2, ...$ etc. J_{ij} denotes the strength of the exchange interaction. Its sign determines the favorable alignment of the nearest neighbors spins. The case of $J > 0$ ($J < 0$) corresponds to antiferromagnetic (ferromagnetic) exchange interaction. Note that the Hubbard model for spinful particles reduces to the Heisenberg model when the charge mode is frozen.

The strength of the exchange interaction J_{ij} falls down as the distance between interaction spins increases. Here, as before for the Hubbard model, we consider that i and j are nearest-neighbors on the lattice. The Hamiltonian (1.16) can describe various types of interactions and therefore, many models have been studied. In further chapters, we analyze some of them such as: the isotropic Heisenberg ($J_x = J_y = J_z$), the anisotropic Heisenberg ($J_x = J_y \neq J_z$) and the XY ($J_z = 0$) models.

For high-spin systems, one introduces the so-called generalized quantum spin models that extend the usual Heisenberg interaction. This model is described by the polynomial generic spin exchange Hamiltonian

$$\hat{H} = \sum_{\gamma}^{2S} \sum_{<ij>} J_{ij,\gamma} \left(\vec{S}_i \cdot \vec{S}_j \right)^{\gamma}. \tag{1.17}$$

Later on we focus on the models for spin-3/2 and spin-1.

The interest in low-dimensional systems, in particular one-dimensional magnets, developed into a field of its own because these systems provide a unique possibility to study ground state and low-lying excited states of quantum models. From the theoretical point of view, the field is extremely broad and has generated a large variety of analytical and numerical methods. In the analytical side, one can list the Bethe ansatz and the mapping to fermionic systems as exact solutions. Bosonization and semiclassical nonlinear σ-model as quantum field approaches. Other methods include perturbative approaches and many-body theory methods as Schwinger bosons, to mention only few.

The numerical methods, like MPS and Lanczos, have been boosted in this field as well. Nonetheless, the Hilbert space dimensionality still is a major issue in the determination of the exact solutions for the many body problems.

1.4.1 Quantum phase transitions in lattice systems

Let us start with a simple question and introduce gradually concepts and properties of this branch of the condensed matter physics, nowadays very interesting from the point of view of low-dimensional finite-lattice systems in the ultra-cold gases community.

What is a phase transition? Everyday examples include the boiling of water or the melting of ice. Phase transitions occur upon variation of an external control parameter and their common characteristic is a qualitative change in the nature of the system state correlations. The phase transitions mentioned so far occur at a finite temperature where the macroscopic order is destroyed by thermal fluctuations, for instance, the crystal structure in the case of ice melting. During recent years, the transitions taking place at zero temperature have attracted growing attention. A non-thermal control parameter such as pressure or magnetic field is varied to access the transition point. In this particular case, the order is destroyed exclusively by quantum fluctuations. Therefore, they are called quantum phase transitions.

In lattice systems, a phase transition can be identified by any non-analyticity point in the ground state energy. This non-analyticity could be either the limiting case of an avoided level-crossing or an actual level-crossing. In this context, the many-body eigenstates point of view is useful to study quantum transitions. If indeed, there is a singularity rising from a simple level

crossing in the many-body ground state then we have a first-order quantum phase transition with no diverging correlations and associated critical singularities. A first-order quantum transition can also occur in a finite-size system as well. The situation is different for continuous transitions, where a higher-order singularity in the ground state energy occurs: here an infinite number of many-body eigenstates may be involved. This is nothing but an avoided level crossing in the ground state, which might become infinitely sharp in the thermodynamic limit.

In finite-size systems, ground state degeneracies are lifted leading into a unique ground state and excited states. Therefore, if there is any level-crossing in the thermodynamic limit, it is translated to the low-lying excited states of the finite system. Quantum critical behavior, rising from the peculiar excitation spectrum, can influence measurable quantities in order to retrieve phase diagrams. Consequently, numerical simulations of continuous transitions are very difficult to capture and the phases may show just a crossover as the borders blurred. Thus, different techniques should be taking into account in order to precise not only the phase-transition boundaries but also the nature of the phases involved.

1.4.2   Spinor systems in optical lattices

Spinor atomic gases are formed by atoms with non-zero spin (the sum of electronic and nuclear spin) denoted by a quantum number F, and in which all orientations of the atomic spin may be realized. Since optical traps allow the simultaneous trapping of several Zeeman sublevels, the ground state of the systems is much richer, characterized by different phases with different spin orders.

When the particle number is large in the trap, the energy gap between the singlet ground state and the higher-energy excited states is extremely small. Therefore, in the experiments the precession time of the classical mean-field ground state is of the order of the trap lifetime [55]. To amplify quantum-spin effects and facilitate their experimental observation, it is desirable to have smaller number of particles and stronger interactions between atoms.

Hence, spinor atoms in optical lattices provide a novel realization of strongly-correlated quantum magnetic systems. Stronger interactions and smaller occupation number open the fascinating possibility of several insulating phases according to different spin correlations. Manipulation of spins and magnetism has been a motivating goal in a great deal of condensed matter, atom optics, quantum information and cold-atoms research.

Detection

Besides of the preparation and manipulation, ultra-cold spinor gases offer also an unprecedented playground for the detection of strongly correlated many-body systems. The ideal measurement of quantum noise for magnetization would be state-selective *in situ* imaging with single atom precision to obtain accurate high order statistics and high resolution to resolve spatial correlations.

Considerable attention has thus been devoted recently to novel methods of detection that allow measurement of (spin) density-density and other higher order correlation functions. One of those methods is atomic noise interferometry [56]. Its power is illustrated by the observation of the bosonic and the fermionic Hanbury-Brown-Twiss (HBT) effect [57, 58]. Another method is the single-atom detection, which has been used also for HBT experiments [59] and to go beyond them [60]. Direct atom counting has been demonstrated in an atom laser set-up by using cavity quantum electrodynamics [61], this method is suited to the study of temporal correlations, for instance TOF experiments, rather than *in situ*, which probes spatial (real space) correlations. There are also proposals on how to prepare and detect magnetic quantum phases using superlattices [62]. All of these approaches are, at least in some respects, destructive and frequently suffer from undesired atom number fluctuations that are inevitable in the preparation of the quantum states.

Quantum non-demolition schemes have been proposed which offer the possibility of measuring quantum fluctuations in the total magnetization of the system employing quantum Faraday effect [63, 64]. From one side, spatially resolved components of atomic spins couple to light quantum polarization degrees of freedom. In this way, quantum correlations of matter are faithfully mapped on those of light; the latter can then be efficiently measured using homodyne detection. We recall that the homodyne detection is a method of detecting frequency-modulated radiation by non-linear mixing with radiation of a reference frequency [63]. In this case, the quantum noise of the laser itself should be less than that of the magnetization and may make features at the single atom level difficult to detect. On the other hand, quantum noise has been used to characterize many-body states of spin systems in a regime with a large but not macroscopic number of atoms. The full distribution function is experimentally relevant and encodes high order correlation functions that may distinguish various many-body states, between ordered, critical, and disordered phases.

1.4.3   Spinor bosons

Spinor Bose-Einstein condensates have attracted a large attention in recent years [65–68], mostly motivated by the rich physics resulting from the interplay

between internal and external degrees of freedom.

Depending on interparticle interactions [65, 67] given by the s-wave scattering lengths $a_{0,2}$ for collisions with total spin 0 and 2, a BEC of cold atoms with hyperfine spin $F = 1$ has been achieved in experiments with ^{23}Na atoms [69] which interact antiferromagnetically (AFM) and with ^{87}Rb atoms [70, 71] characterized by ferromagnetic interactions (FM). They are the simplest spinor system beyond two-components.

Spin-1 lattice bosons have attracted a strong interest from both theory and experimental side, especially the AFM case, for which a wealth of quantum phases have been predicted [65–68, 72–78]. For AFM interactions, mean-field analyzes in two- and three-dimensional lattices, revealed that the SF phase is polar whereas MI states with odd filling are nematic [68, 77, 79]. In the case of even filling, for small tunneling the MI states are singlets and for moderate tunneling there occurs a first order transition to the nematic state. In one-dimension quantum fluctuations lead to a spontaneously dimerized MI ground state (spin Peierls), order that breaks lattice translational symmetry [66, 68, 72, 73, 76, 80–82].

In continuum, the polar state and FM states have been proposed [65, 67]. In particular, the case where $a_0 = a_2$ exhibits an enlarged symmetry and corresponds to an SU(3) FM [79–81], that has a highly degenerate ground state unifying many types of order [83]. Most spin-1 species are naturally close to this multi-critical point (i.e. $a_0 \approx a_2$), where small external perturbations, as Zeeman shifts, may have a large effect, reducing the system symmetry, and thus favoring different phases.

The spinor dynamics has been at the focus of major interest [84–87] since it is clearly differentiated from the one displayed by scalar condensates. The dynamics resulting from spin-changing collisions, which coherently re-distribute the populations among the different Zeeman sublevels, is characterized by a very low energy scale. This scale is much lower than the chemical potential in the condensate. As a consequence, the spinor dynamics in alkaline gases may be extraordinary sensitive to other small energy scales, such as the dipole-dipole interaction [88, 89]. As an interesting application, measurements of the coherent collisional spin dynamics in lattices have allowed for a very precise determination of the ^{87}Rb scattering lengths for $F = 1$ and $F = 2$ [90, 91].

Later on in this Thesis, we discuss the phase diagram for Mott-insulating phases of repulsively-interacting ultra-cold spin-1 bosons with unit filling. Such system is described by a bilinear-biquadratic Hamiltonian (See Eq. (4.30) in Chapter 4). Our main contribution is the inclusion of the quadratic Zeeman coupling (QZE) to the system. Note that the QZE may be controlled by means of microwave and optical techniques [92, 93]. Hence, as recently demonstrated for spinor BECs in the continuum [86], the results of this Thesis show that a controlled quenching of the QZE may permit the observation of field-induced phase transitions in spin-1 lattice bosons, which are precluded by simple use

of the linear Zeeman effect due to conservation of magnetization, and thus are absent in spin-1/2 systems. In addition, optical Feshbach resonances [94, 95] permit the modification of the ratio of the scattering lengths a_2/a_0, so that the full phase diagram discussed in Chapter 6 may be explored with state of the art techniques.

1.4.4 Spinor fermions

Although until now spinor bosons have attracted a larger attention, spinor fermions have recently become the focus of a rapidly growing interest and in particular spinor Fermi gases in optical lattices. This fact has been motivated by the experiments on BEC-BCS crossover in two-component fermions [28]. The availability of multicomponent fermions opens exciting perspectives for the observation of a wealth of new quantum phases.

The realization of the metal to Mott insulator transition in two-component Fermi gas in an optical lattice [2, 3] is signalled by a drastic suppression of doubly occupied lattice sites, a strong reduction of the compressibility inferred from the response of double occupancy to atom number increase, and the appearance of a gapped mode in the excitation spectrum. Even more interesting the suppression of conductivity in the system is a result of the interactions and not the consequence of a filled Bloch band like in usual insulators.

The proximity to the Mott insulating phase in fermionic systems is the origin for many intriguing phenomena in condensed matter physics. The first reason is that such system is a perfect quantum simulator of the fermionic Hubbard model, and thus shine light on the problem of high T_c superconductivity. This has been proposed for $F = 1/2$ [96] and recently considered with three-component fermions [97].

Listing some candidates for high-F fermionic spinor gases in optical lattices, one should include the alkali ^{6}Li which has hyperfine manifolds with $F = 1/2$ and $F = 3/2$, spite of the two-body losses, long life time in the lattice is expected. On the other hand, three component Li gases [98] are also expected to give rise to interesting superfluid phases. Another commonly used fermion is the heavy alkali ^{40}K, which has manifolds $F = 7/2$ and $F = 9/2$. The production of the degenerate ^{40}K gas in an optical lattice by sympathetic cooling with bosonic ^{87}Rb atoms, has been achieved [99]. There are several elements whose lowest hyperfine manifold have $F = 3/2$ and where the two body losses can be avoided, such as ^{9}Be, ^{132}Cs, ^{135}Ba and ^{137}Ba [100], but so far only the bosonic Cs-BEC has been achieved [101]. Recently Fermi degeneracy has been reached as well with ultra-cold alkaline-earth-metal-like atoms such as ^{173}Yb [102] which opens the fascinating possibility of $SU(6)$-symmetric spin-5/2 gases [103]. The spin-degeneracy in multi-component fermions includes also pseudo-spin-1 fermions [104] which allows for color superfluidity and trions, whereas attractive spin-3/2 gases allow also for the possibility of quartet

formation [105–109], a four-fermion counterpart of Cooper pairing.

We are also interested in exploring the rich physics of repulsive spin-3/2 fermions [105–108, 110, 111], which at quarter filling may undergo a MI transition. Contrary to spin-1/2, the MI of spin-3/2 presents in 1D two distinct magnetic phases given by a gapless spin-liquid or a gapped dimerized phase, depending on the interatomic interactions. While for spin-1/2 spin-changing collisions are absent and the quadratic Zeeman effect (QZE) is irrelevant, the latter is crucial for higher-spins, as shown in spinor condensates [65]. In spite of its experimental relevance, the QZE is mostly ignored in the analysis of the magnetic properties. In this Thesis we show that the QZE has indeed important consequences for the physics of spin-3/2 fermions.

1.5 Overview

This Thesis is structured as follows. Chapter 2 introduces the numerical methods used in this work for the description of the different ultra-cold atom systems. We discuss in detail the matrix product state (MPS) ansatz. Thereafter, the Thesis is divided in two parts.

In Part I, we concentrate on the correlation-dynamics of superfluid Bose gases in one-dimensional time-dependent optical lattices. Quasi-local functions besides long-range correlations like the quasi-condensate fraction are introduced and their dynamics is studied. The adiabaticity issue is also regarded.

In Part II, we focus on spinor systems. In particular, we analyze the influence of the quadratic Zeeman coupling on the Mott-insulator phases of repulsively interacting spin-3/2 fermions and spin-1 bosons. For large enough interactions and under certain conditions, the system can be kept in the MI with one particle per site. In Chapter 4, the effective hard-core Hamiltonian with super-exchange interaction is retrieved by means of perturbation theory and symmetry considerations. Chapter 5 is devoted to the MI phase diagram for spin-3/2 fermions as a function of the spin-changing collisions and the QZE. The quantum phases are characterized in detail and the nature of the phase transitions is analyzed. Chapter 6 deals with the field-induced phase transitions of spin-1 bosons. There, we characterize the phase diagram and the corresponding phase transitions. Finally, Chapter 7 outlines the potential of the system models and methods considered in this Thesis and points towards possible further applications.

Numerical Methods

In classical mechanics, the description of n particles with d degrees of freedom scales linearly as $2dn$. On the other hand in quantum mechanics, the problem grows exponentially. The Hilbert space for an analogous situation as above, would have a dimension of d^n. This makes numerical simulations of solid state physics, quantum statistical mechanics or many-body physics challenging at best or even impossible at worst.

In a general context one needs to calculate only a few eigenstates of the quantum system Hamiltonian of interest. Naturally, this implies that the Hilbert space of the problem has to be truncated either by considering finite systems or by imposing suitable cut-offs, or both. Fortunately in low dimensions, efficient numerical methods have been developed and successfully used to understand a variety of models in recent years [112]. For the numerical studies of strongly correlated quantum systems, the most important methods are Quantum Monte-Carlo (QMC) [113, 114], exact diagonalization (ED) including the Lanczos algorithm and the density matrix renormalization group (DMRG) method. The latest was first introduced in the condensed matter community by S. White [115–118] and described by the matrix product states (MPS) technique developed in the context of quantum information theory [112, 119–122].

2.1 Matrix product states

The DMRG was originally intended to study ground state properties of 1D strongly correlated systems in condensed matter. The DMRG and the MPS connection relates the thermodynamic limit of the DMRG with a position-independent matrix product wavefunction [123]. This identification leaded to an important step into rigorous further algorithms. Nowadays, a much wider family of MPS-like algorithms for simulating quantum systems has been developed, including time evolution [112, 119], periodic boundary conditions [120], ground state calculations [122], finite temperature [121, 124], infinite systems [125] and excitation spectra [126]. Let us point out that the required computational effort is essentially a function of the entanglement of the wavefunction, which for 1D systems scales at worst logarithmically with the system size [127].

2.1.1 How to build up a MPS.

When one has a quantum system, described by the state $|\psi\rangle$, consisting of two subsystems A and B, then the state in general can be expressed as:
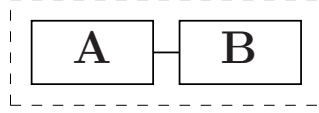
$$|\psi\rangle = \sum_{ij} a_{ij}|A_i\rangle \otimes |B_j\rangle, \qquad (2.1)$$

where $\{|A_i\rangle\}$ and $\{|B_j\rangle\}$ are the complete set of orthonormal basis vectors in their respective Hilbert subspaces. The combined state contains $N_A N_B$ expansion coefficients and could be very difficult to manipulate.

In this thesis, we consider physical lattice systems made of an array with L sites. Let us separate the last site forming a bipartite (two-subsystem) system, as in Fig. 2.1(a).
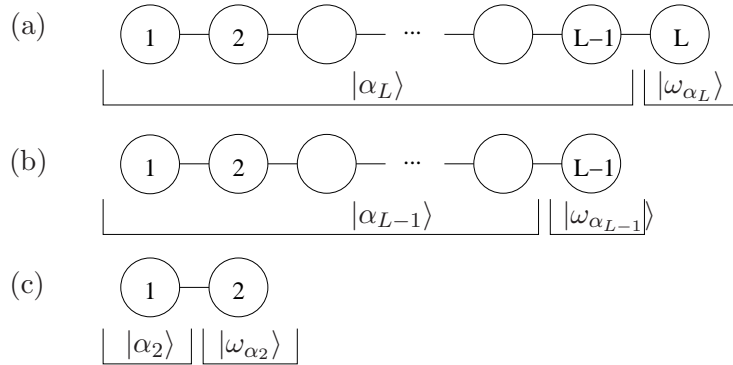

FIGURE 2.1: Schmidt decomposition of a chain. We divide the chain in two parts, for site 1 to L-1 (left block) and the last right site. Then, the next step is to divide the left block in two parts as well.

As next step, we apply the Schmidt decomposition (SD) [128] to the state $|\psi\rangle$. Following this decomposition, any arbitrary pure state of a bipartite system can be written as

$$|\psi\rangle = \sum_{\alpha_L=1}^{N_B} \lambda_{\alpha_L}|\alpha_L\rangle^{[A]} \otimes |\omega_{\alpha_L}\rangle^{[B]}, \qquad (2.2)$$

where $\{|\alpha_L\rangle\}$ (on the left block) and $\{|\omega_{\alpha_L}\rangle\}$ (on the single site) are two orthonormal basis sets belonging to the respective Hilbert subspaces, each with N_B basis elements. Here $N_A > N_B$. The coefficients λ_{α_L} are non-negative real numbers satisfying $\sum_{\alpha_L} \lambda_{\alpha_L}^2 = 1$, known as the *Schmidt coefficients*.

We would like to re-express the previous bases in the Fock basis, since, it is known how the operators act on it. Let us start projecting the single-site B block, $|\omega_{\alpha_L}\rangle = \sum_{n_L} \Gamma_{\alpha_L}^{n_L} |n_L\rangle$, where $\Gamma_{\alpha_L}^{n_L}$ are the matrix elements of the transformation and $\{|n_L\rangle\}$ are the Fock basis elements. Therefore, the state $|\psi\rangle$ can be re-written as follows:

$$|\psi\rangle = \sum_{\alpha_L n_L} \lambda_{\alpha_L} \Gamma_{\alpha_L}^{n_L} |\alpha_L\rangle |n_L\rangle \qquad (2.3)$$

Now, let us concentrate in the $|\alpha_L\rangle$ block. From the $L-1$ sites that it contains, we separate the last one again and perform the Schmidt decomposition as it is shown in Fig. 2.1(b). Thus, the state for this new left block is given by

$$|\alpha_L\rangle = \sum_{\alpha_{L-1}} \lambda_{\alpha_{L-1}} |\alpha_{L-1}\rangle |\omega_{\alpha_{L-1}}^{\alpha_L}\rangle. \qquad (2.4)$$

The single site block, $|\omega_{\alpha_{L-1}}^{\alpha_L}\rangle = \sum_{n_{L-1}} \Gamma_{\alpha_{L-1}\alpha_L}^{n_{L-1}} |n_{L-1}\rangle$, is also expressed in the Fock basis. Since the site $L-1$ is connected to the site L in the chain, one cannot forget the dependency of α_L in the index array. We include it explicitly.

Replacing $|\omega_{\alpha_{L-1}}^{\alpha_L}\rangle$ in Eq. (2.4), plugging the result in the state (2.3) and tracking all the indexes correctly, we obtain

$$|\psi\rangle = \sum_{\substack{\alpha_{L-1}\alpha_L \\ n_{L-1}n_L}} \lambda_{\alpha_{L-1}} \Gamma_{\alpha_{L-1}\alpha_L}^{n_{L-1}} \lambda_{\alpha_L} \Gamma_{\alpha_L}^{n_L} |\alpha_{L-1}\rangle |n_L n_{L-1}\rangle. \qquad (2.5)$$

We keep doing this procedure until we reach the second site as it is depicted in Fig. 2.1(c). At this point, we end up with two single sites with no further division for the left block. The later expressed in the Fock basis is given by $|\alpha_2\rangle = \sum_{n_1} \lambda_{\alpha_2} \Gamma_{\alpha_1\alpha_2}^{n_1} |n_1\rangle$. But, it can be further simplified since the coefficient λ_2 is just a Kronecker delta $\lambda_2 = \delta_{1\alpha_1}$, so these two sites are written as follows,

$$|\omega_{\alpha_2}^{\alpha_3}\rangle = \sum_{n_2} \Gamma_{\alpha_2\alpha_3}^{n_2} |n_2\rangle \quad \text{and} \quad |\alpha_2\rangle = \sum_{n_1} \Gamma_{\alpha_2}^{n_1} |n_1\rangle. \qquad (2.6)$$

Then, the state of the whole system has the form

$$|\psi\rangle = \sum_{\substack{\alpha_2...\alpha_L \\ n_1...n_L}} \Gamma_{\alpha_2}^{n_1} \lambda_{\alpha_2} \Gamma_{\alpha_2\alpha_3}^{n_2} \ldots \lambda_{\alpha_{L-1}} \Gamma_{\alpha_{L-1}\alpha_L}^{n_{L-1}} \lambda_{\alpha_L} \Gamma_{\alpha_L}^{n_L} |n_1 \ldots n_L\rangle. \qquad (2.7)$$

In order to simplify the expressions, we define the $\mathbb{A}^s$ matrix, that belongs to the site s, in the following way: $A_{\alpha_s\alpha_{s+1}}^{n_s} \equiv \lambda_{\alpha_s} \Gamma_{\alpha_s\alpha_{s+1}}^{n_s}$. Finally, the matrix product representation of the pure state is given by

$$|\psi\rangle = \sum_{\substack{\alpha_2 \ldots \alpha_L \\ n_1 \ldots n_L}} A^{n_1}_{\alpha_1 \alpha_2} A^{n_2}_{\alpha_2 \alpha_3} \ldots A^{n_{L-1}}_{\alpha_{L-1} \alpha_L} A^{n_L}_{\alpha_L \alpha_{L+1}} |n_1 \ldots n_L\rangle, \qquad (2.8)$$

where we have introduced the coefficients α_1 and α_{L+1} in blue, although $\alpha_1, \alpha_{L+1} = 1$. This is done only to keep all the matrices with the same dimension and generic form.

Truncations

The number of matrix elements that $\mathbb{A}^s$ has is given by $N_s = d \min[d^{2s}, d^{2(L-s)}]$ which is still exponentially big. However from numerical analysis, it had been found that the Schmidt coefficients λ_{α_s} decay (roughly) exponentially with α_s in both ground state and time-evolution calculations [119]. Therefore, the MPS ansatz can be truncated by the restriction $\alpha_s = 1, \ldots, \chi_s$.

As we already commented, it was shown that the DMRG system state is made of a position-independent matrix product wavefunction. Hence, one can choose a fixed number of elements $\chi_s \equiv \chi$ for every site. Thus, the number of $\mathbb{A}^s$ matrix elements is reduced to

$$\bar{N}_s = d\chi^2, \qquad (2.9)$$

while keeping a faithful representation of the original state. The total number of the matrix elements required numerically is $d\chi^2 L$ since there are L sites. This means that the dimension increases algebraically rather than exponentially as the Hilbert space dimension does. Moreover, the parameter χ is related directly to the entanglement of the system. An essential requirement for the numerical method to be efficient and reliable is that the entanglement should be "small" or χ must be updated during a simulated dynamics, in order to keep a faithful representation.

Orthogonalization of a MPS

The singular value decomposition. A MPS state with no particular constraints on the form of its $\mathbb{A}$ matrices is numerically difficult to handle. To simplify its manipulation, one can transform an arbitrary MPS into a form where it is orthonormalized. In this way, the difficulty of the operations, like to find the norm of a given state or to calculate a desirable observable, is reduced.

Therefore, in order to normalize an arbitrary MPS, we use the singular value decomposition (SVD). This technique is a well-known linear algebra technique to factorize a real or complex matrix. Suppose $\mathbb{A}$ is a $m \times n$ matrix, then exists a factorization of the form:

$$\mathbb{A} = UDV^\dagger, \qquad (2.10)$$

where U is a $m \times m$ column-orthogonal matrix and V is a $n \times n$ row-orthogonal matrix. This means

$$U^\dagger U = 1 \quad \text{and} \tag{2.11}$$

$$VV^\dagger = 1. \tag{2.12}$$

D is a $m \times n$ non-negative diagonal matrix containing the *singular values* of $\mathbb{A}$, so $D_{\alpha\alpha'} = D_\alpha \delta_{\alpha\alpha'}$. These coefficients coincide with the ones given by the Schmidt decomposition.

Orthogonalization process

To orthogonalize the state $|\psi\rangle$ of Eq. (2.8), we apply the SVD site by site from one end to the other of the chain. The process is as follows:

1. From left to right

   - Perform a SVD for the first matrix of the left-hand coefficients:

   $$A^{n_1}_{\alpha_2} = \sum_{\alpha'_2} U^{n_1}_{\alpha'_2} D_{\alpha'_2} V^\star_{\alpha'_2 \alpha_2}. \tag{2.13}$$

   - Consider the $\mathbb{A}$ matrix of the second site in order to pack all the matrices referring to α_2 together and replace the expression (2.13) by:

   $$\sum_{\substack{n_1,n_2 \\ \alpha_2\alpha_3}} A^{n_1}_{\alpha_2} A^{n_2}_{\alpha_2\alpha_3} = \sum_{\substack{n_1,n_2 \\ \alpha'_2\alpha_3}} U^{n_1}_{\alpha'_2} \underbrace{\sum_{\alpha_2} D_{\alpha'_2} V^\star_{\alpha'_2\alpha_2} A^{n_2}_{\alpha_2\alpha_3}}_{\bar{A}^{n_2}_{\alpha'_2\alpha_3}}$$
   $$= \sum_{\substack{n_1,n_2 \\ \alpha'_2\alpha_3}} U^{n_1}_{\alpha'_2} \bar{A}^{n_2}_{\alpha'_2\alpha_3} \tag{2.14}$$

   - Then, introduce the $\mathbb{A}$ matrix of the third site and apply the SVD to the $\bar{\mathbb{A}}$ matrix of Eq. (2.14):

   $$\sum_{\substack{n_1,n_2,n_3 \\ \alpha'_2,\alpha_3,\alpha_4}} U^{n_1}_{\alpha'_2} \bar{A}^{n_2}_{\alpha'_2\alpha_3} A^{n_3}_{\alpha_3\alpha_4} = \sum_{\substack{n_1,n_2,n_3 \\ \alpha'_2,\alpha'_3,\alpha_4}} U^{n_1}_{\alpha'_2} U^{n_2}_{\alpha'_2\alpha'_3} \underbrace{\sum_{\alpha_3} D_{\alpha'_3} V^\star_{\alpha'_3\alpha_3} A^{n_3}_{\alpha_3\alpha_4}}_{\bar{A}^{n_3}_{\alpha'_3\alpha_4}}$$
   $$= \sum_{\substack{n_1,n_2,n_3 \\ \alpha'_2,\alpha'_3,\alpha_4}} U^{n_1}_{\alpha'_2} U^{n_2}_{\alpha'_2\alpha'_3} \bar{A}^{n_3}_{\alpha'_3\alpha_4} \tag{2.15}$$

Applying the same procedure until reach the kth-site, the state is written as:

$$|\psi\rangle = \sum_{\substack{n_1,\ldots,n_L \\ \alpha_1\alpha'_2\ldots\alpha'_k \\ \alpha_{k+1}\ldots\alpha_{L+1}}} U^{n_1}_{\alpha_1\alpha'_2} U^{n_2}_{\alpha'_3\alpha'_3}\ldots U^{n_{k-1}}_{\alpha'_{k-1}\alpha'_k} \bar{A}^{n_k}_{\alpha'_k\alpha_{k+1}} A^{n_{k+1}}_{\alpha_{k+1}\alpha k+2}\ldots A^{n_L}_{\alpha_L\alpha_{L+1}} |\vec{n}\rangle.$$

$$(2.16)$$

The blue indexes are included again to keep all the matrices with the same generic form. The $\bar{A}$ matrix in red represents the site we have stopped the process.

2. Thereafter, we proceed to do the orthonormalization from the last site to the kth-site. This time the right-hand orthogonal matrices should be used.

   - Start with the SVD for the matrix on the right-hand, in the L-site:

   $$A^{n_L}_{\alpha_L} = \sum_{\alpha'_L} U^{n_L}_{\alpha_L\alpha'_L} D_{\alpha'_L} V^\star_{\alpha'_L}.$$

   $$(2.17)$$

   - Consider the $\mathbb{A}$ matrix that refers to the site $L-1$:

   $$\sum_{\substack{n_{L-1},n_L \\ \alpha_{L-1},\alpha_L}} A^{n_{L-1}}_{\alpha_{L-1}\alpha_L} A^{n_L}_{\alpha_L} = \sum_{\substack{n_{L-1},n_L \\ \alpha_{L-1},\alpha'_L}} \sum_{\alpha_L} \underbrace{A^{n_{L-1}}_{\alpha_{L-1}\alpha_L} U_{\alpha_L\alpha'_L} D_{\alpha'_L}}_{\bar{A}^{n_{L-1}}_{\alpha_{L-1}\alpha'_L}} V^{n_L\star}_{\alpha'_L}$$

   $$= \sum_{\substack{n_{L-1},n_L \\ \alpha_{L-1},\alpha'_L}} \bar{A}^{n_{L-1}}_{\alpha_{L-1}\alpha'_L} V^{n_L\star}_{\alpha'_L}$$

   $$(2.18)$$

   - Then, include the $\mathbb{A}$ matrix of the $L-2$-site and apply the SVD to the $\bar{\mathbb{A}}$ matrix of the Eq. (2.18):

   $$\sum_{\substack{n_{L-2},n_{L-1},n_L \\ \alpha_{L-2},\alpha_{L-1},\alpha'_L}} A^{n_{L-2}}_{\alpha_{L-2}\alpha_{L-1}} \bar{A}^{n_{L-1}}_{\alpha_{L-1}\alpha'_L} V^{n_L\star}_{\alpha'_L}$$

   $$= \sum_{\substack{n_{L-2},n_{L-1},n_L \\ \alpha_{L-2},\alpha_{L-1},\alpha'_L}} A^{n_{L-2}}_{\alpha_{L-2}\alpha_{L-1}} \left(\sum_{\alpha'_{L-1}} u_{\alpha_{L-1}\alpha'_{L-1}} D_{\alpha'_{L-1}} V^{n_{L-1}\star}_{\alpha'_{L-1}\alpha'_L} \right) V^{n_L\star}_{\alpha'_L},$$

   we exchange the sums over α_{L-1} and α'_{L-1} and separate, in the parenthesis, all the terms that contain α_{L-1}, as follows,

$$
= \sum_{\substack{n_{L-2}, n_{L-1}, n_L \\ \alpha_{L-2}, \alpha'_{L-1}, \alpha'_L}} \underbrace{\left(\sum_{\alpha_{L-1}} A^{n_{L-2}}_{\alpha_{L-2}\alpha_{L-1}} U_{\alpha_{L-1}\alpha'_{L-1}} D_{\alpha'_{L-1}} \right)}_{\bar{A}^{n_{L-2}}_{\alpha_{L-2}\alpha'_{L-1}}} V^{n_{L-1}\star}_{\alpha'_{L-1}\alpha'_L} V^{n_L\star}_{\alpha'_L}
$$

$$
= \sum_{\substack{n_{L-2}, n_{L-1}, n_L \\ \alpha_{L-2}, \alpha'_{L-1}, \alpha'_L}} \bar{A}^{n_{L-2}}_{\alpha_{L-2}\alpha'_{L-1}} V^{n_{L-1}\star}_{\alpha'_{L-1}\alpha'_L} V^{n_L\star}_{\alpha'_L} \tag{2.19}
$$

With this process we keep the V-matrices at the left side. So an orthogonalized MPS with respect to site k is given by the following expressions and can be represented by the figure below:
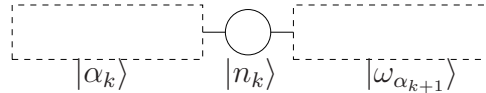
$$
|\psi\rangle = \sum_{n_k \alpha_k \alpha_{k+1}} A^{n_k}_{\alpha_k \alpha_{k+1}} |\alpha_k\rangle |n_k\rangle |\omega_{\alpha_{k+1}}\rangle, \tag{2.20}
$$

where

$$
|\alpha_k\rangle = \sum_{\alpha_1 \ldots \alpha_{k-1}} \prod_{s=1}^{k-1} U^{n_s}_{\alpha_s \alpha_{s+1}} |n_s\rangle, \tag{2.21}
$$

and

$$
|\omega_{\alpha_{k+1}}\rangle = \sum_{\alpha_{k+2} \ldots \alpha_{L+1}} \prod_{s=k+1}^{L} V^{n_s\star}_{\alpha_s \alpha_{s+1}} |n_s\rangle. \tag{2.22}
$$

According to the definition of orthogonal matrices, for any value of k, the states $|\alpha_k\rangle$ and $|\omega_{\alpha_k}\rangle$ satisfy the following relations (the proof of this statement is developed via induction method in Appendix A):

$$
\langle \alpha_k | \alpha'_k \rangle = \delta_{\alpha_k \alpha'_k} \qquad \text{and} \qquad \langle \omega_{\alpha_k} | \omega_{\alpha'_k} \rangle = \delta_{\alpha_k \alpha'_k}. \tag{2.23}
$$

The MPS state is orthonormalized in the sense that all U-matrices to the left of the matrix $A^{n_k}_{\alpha_k \alpha_{k+1}}$ are orthogonalized in the left-hand sense, see Eq. (2.11), and therefore, the left subsystem orthonormal. Conversely, all V-matrices to the right of $A^{n_k}_{\alpha_k \alpha_{k+1}}$ are orthogonal in the right-hand sense, see Eq. (2.12), then the basis of the right-hand side is orthonormal.

The main result of this part is the generic orthonormalized MPS state form, see Eq. (2.20), which we use henceforth.

2.1.2   Calculation of expectation values

The next point is to calculate the quadratic form of desired observables using the orthonormalized MPS of Eq. (2.20). Usually, one studies on-site operators, nearest-neighbor operators and correlation functions.

On-site operators.

First, we discuss a general local operator $\langle \hat{O}^i \rangle$, acting in the site i, while the $\mathbb{A}^s$ matrix, which contains the state information, is located in the site s. Suppose that $i > s$ then we perform the measurement as follows:

$$
\langle \psi | \hat{O}^i | \psi \rangle = \sum_{\substack{n'_s \ldots n'_i \; \alpha'_s \ldots \alpha'_{i+1} \\ n_s \ldots n_i \; \alpha_s \ldots \alpha_{i+1}}} A^{n'_s *}_{\alpha'_s \alpha'_{s+1}} V^{n'_{s+1} *}_{\alpha'_{s+1} \alpha'_{s+2}} \cdots V^{n'_{i-1} *}_{\alpha'_{i-1} \alpha'_i} V^{n'_i *}_{\alpha'_i \alpha'_{i+1}}
$$

$$
A^{n_s}_{\alpha_s \alpha_{s+1}} V^{n_{s+1}}_{\alpha_{s+1} \alpha_{s+2}} \cdots V^{n_{i-1}}_{\alpha_{i-1} \alpha_i} V^{n_i}_{\alpha_i \alpha_{i+1}}
$$

$$
\underbrace{\langle \alpha'_s | \alpha_s \rangle}_{\delta_{\alpha'_s, \alpha_s}} \underbrace{\langle n'_s \ldots n'_{i-1} | n_s \ldots n_{i-1} \rangle}_{\delta_{n'_s \ldots n'_{i-1}, n_s \ldots n_{i-1}}} \underbrace{\langle \omega_{\alpha'_{i+1}} | \omega_{\alpha_{i+1}} \rangle}_{\delta_{\omega_{\alpha'_{i+1}}, \omega_{\alpha_{i+1}}}} \langle n'_i | \hat{O}^i | n_i \rangle .
$$

Now, we apply the Kronecker deltas and write the remaining terms, in such way that we keep together the terms related to the same site, as follows:

$$
\langle \psi | \hat{O}^i | \psi \rangle = \sum_{\substack{\alpha_s \\ \alpha_{i+1}}} \sum_{\substack{\alpha'_{s+1} \ldots \alpha'_i \\ \alpha_{s+1} \ldots \alpha_i}} \left[\sum_{n_s} A^{n_s *}_{\alpha_s \alpha'_{s+1}} A^{n_s}_{\alpha_s \alpha_{s+1}} \right] \left[\sum_{n_{s+1}} V^{n_{s+1} *}_{\alpha'_{s+1} \alpha'_{s+2}} V^{n_{s+1}}_{\alpha_{s+1} \alpha_{s+2}} \right] \cdots
$$

$$
\tag{2.24}
$$

$$
\left[\sum_{n_{i-1}} V^{n_{i-1} *}_{\alpha'_{i-1} \alpha'_i} V^{n_{i-1}}_{\alpha_{i-1} \alpha_i} \right] \left[\sum_{n_i, n'_i} V^{n'_i *}_{\alpha'_i \alpha'_{i+1}} \mathcal{O}_{n'_i n_i} V^{n_i}_{\alpha_i \alpha_{i+1}} \right] .
$$

At this point, let us introduce the concept of *transfer matrix* $\mathbb{E}^k$ of the local operator $\hat{O}^k$ acting on a given site k as,

$$
\mathbb{E}^k(\hat{O}^k) \equiv \sum_{n_k n'_k} B^{n'_k *}_{\alpha'_k \alpha'_{k+1}} \mathcal{O}_{n'_k n_k} B^{n_k}_{\alpha_k \alpha_{k+1}}, \tag{2.25}
$$

The following diagram clarifies the meaning of this object, the boxes represent the B-matrix at site s and its complex conjugate. In between, one finds the expected value of the generic on-site operator $\hat{O}^k$ on the local Fock basis. The complexity of the transfer matrix is observed in its dimension since $\dim \left[\mathbb{E}^k(\hat{O}^k) \right] \equiv \chi^4$.

$$\mathbb{E}^k(\hat{O}) = \begin{array}{c} \alpha_k \fbox{B^k} \alpha_{k+1} \\ \langle n'_k|\hat{O}|n_k\rangle \\ \alpha'_k \fbox{$B^{k\star}$} \alpha'_{k+1} \end{array}$$

One can see the importance of this concept in Eq. (2.24), since it has three different cases where one uses the transfer matrices of an operator:

1. Identify B with A, the operator $\mathcal{O}_{n'_s n_s} = \delta^{n_s}_{n'_s}$ and perform the index grouping $\gamma_{s+1} \equiv (\alpha'_{s+1}, \alpha_{s+1})$:

$$\sum_{\substack{\alpha_s \\ }} \sum_{\substack{\alpha'_{s+1} \\ \alpha_{s+1}}} \left[\sum_{n_s} A^{n_s *}_{\alpha_s \alpha'_{s+1}} A^{n_s}_{\alpha_s \alpha_{s+1}} \right] = \sum_{\substack{\alpha'_{s+1} \\ \alpha_{s+1}}} \sum_{\substack{\alpha'_s \\ \alpha_s}} \delta^{\alpha_s}_{\alpha'_s} \left[\sum_{n_s} A^{n_s *}_{\alpha'_s \alpha'_{s+1}} A^{n_s}_{\alpha_s \alpha_{s+1}} \right]$$

$$= \sum_{\gamma_{s+1}} \sum_{\alpha'_s, \alpha_s} \delta^{\alpha_s}_{\alpha'_s} \mathbb{E}(\hat{I}^s)^{\alpha'_s}_{\alpha_s, \gamma_{s+1}}$$

$$= \sum_{\gamma_{s+1}} \mathbf{Tr}_{\overleftarrow{\mu}} \left[\mathbb{E}^s(\hat{I}^s) \right]. \qquad (2.26)$$

Where $\mathbf{Tr}_{\overleftarrow{\mu}} [\cdot]$ means: first, change of index $\mu \equiv (\alpha'_s, \alpha_s)$ and second, calculate the trace over μ, which refers to the left-site index pair, of the transfer matrix. In other words, this trace means to close the open left channels as it is depicted in the following sketch.

$$\mathbf{Tr}_{\overleftarrow{\mu}} \left[\mathbb{E}^s(\hat{I}^s) \right] = \begin{array}{c} \alpha_s \fbox{B^s} \alpha_{s+1} \\ \langle n'_s|\hat{I}|n_s\rangle \\ \fbox{$B^{s\star}$} \alpha'_{s+1} \end{array}$$

2. Identify B with V, the operator $\mathcal{O}_{n'_k n_k} = \delta^{n_k}_{n'_k}$ with $k \in [s+1, \ldots, i-1]$ and the index grouping $\gamma_k \equiv (\alpha'_k, \alpha_k)$:

$$\sum_{\substack{\alpha'_k \\ \alpha_k}} \sum_{\substack{\alpha'_{k+1} \\ \alpha_{k+1}}} \left[\sum_{n_k} V^{n_k *}_{\alpha'_k \alpha'_{k+1}} V^{n_k}_{\alpha_k \alpha_{k+1}} \right] = \sum_{\alpha'_k, \alpha_k} \sum_{\alpha'_{k+1}, \alpha_{k+1}} \left[\sum_{n_k} V^{n_k *}_{\alpha'_k \alpha'_{k+1}} V^{n_k}_{\alpha_k \alpha_{k+1}} \right]$$

$$= \sum_{\gamma_k} \sum_{\gamma_{k+1}} \mathbb{E}(\hat{I}^k)_{\gamma_k, \gamma_{k+1}}. \qquad (2.27)$$

3. Identify B with V, the operator $\mathcal{O}_{n'_i n_i}$ which is acting on the site i and the index grouping $\gamma_i \equiv (\alpha'_i, \alpha_i)$ and $\mu \equiv (\alpha'_{i+1}, \alpha_{i+1})$:

$$
\sum_{\substack{\alpha'_i \\ \alpha_i}} \sum_{\alpha_{i+1}} \left[\sum_{n_i, n'_i} V^{n'_i *}_{\alpha'_i \alpha_{i+1}} \mathcal{O}_{n'_i n_i} V^{n_i}_{\alpha_i \alpha_{i+1}} \right] = \sum_{\substack{\alpha'_{i+1} \\ \alpha_{i+1}}} \sum_{\substack{\alpha'_i \\ \alpha_i}} \delta^{\alpha_{i+1}}_{\alpha'_{i+1}} \left[\sum_{n_i, n'_i} V^{n'_i *}_{\alpha'_i \alpha'_{i+1}} \mathcal{O}_{n'_i n_i} V^{n_i}_{\alpha_i \alpha_{i+1}} \right]
$$

$$
= \sum_{\gamma_i} \mathbf{Tr}_{\underset{\rightarrow}{\mu}} \left[\mathbb{E}^i(\hat{O}^i) \right]. \qquad (2.28)
$$

This time, we perform the trace closing the open channels in the right-hand side. Therefore, it is called $\mathbf{Tr}_{\underset{\rightarrow}{\mu}}[\cdot]$ and we sketch it as follows:

Let us come back to our original calculation, the expected value of a local operator $\hat{O}^i$, we can rewrite now the expression in Eq. (2.24) in terms of the transfer matrices of Eqs. (2.26), (2.27) and (2.28).

$$
\langle \psi | \hat{O}_i | \psi \rangle = \mathbf{Tr} \left[\mathbb{E}^s(\hat{I}^s) \dots \mathbb{E}^{i-1}(\hat{I}^k) \dots \mathbb{E}^{i-1}(\hat{I}^{i-1}) \mathbb{E}^i(\hat{O}^i) \right] \qquad (2.29)
$$

Finally, we perform the sum over all one-site operators, taking into account that i is never s, then we have,

$$
\sum_i \langle \hat{O}_i \rangle = \sum_i \mathbf{Tr} \left[\mathbb{E}^s \mathbb{E}^{s+1} \dots \mathbb{E}^{i-1} \mathbb{E}^i(\hat{O}^i) \right]
$$

$$
= \mathbf{Tr} \left[\mathbb{E}^s \sum_i \mathbb{E}^{s+1} \dots \mathbb{E}^{i-1} \mathbb{E}^i(\hat{O}^i) \right]. \qquad (2.30)
$$

Norm of a MPS.

Now, we are able also to compute the norm of a given MPS. This is nothing else than replacing the on-site operator by the identity in the expected value of Eq.(2.29). If the state is not orthonormalized, which means $\langle \alpha_k | \alpha'_k \rangle \neq \delta_{\alpha_k \alpha'_k}$ and $\langle \omega_{\alpha_k} | \omega_{\alpha'_k} \rangle \neq \delta_{\alpha_k \alpha'_k}$ the product of the transfer matrices is extended on the

whole system and the indexes are grouped as $\mu = (\alpha, \alpha')$,

$$\langle \psi | \psi \rangle = \sum_{\vec{\alpha}, \vec{\alpha}'} \prod_s \left[\sum_{\vec{n}} A^{n_s \star}_{\alpha'_s \alpha'_{s+1}} A^{n_s}_{\alpha_s \alpha_{s+1}} \right] = \sum_{\vec{\mu}} \prod_s \mathbb{E}(\hat{I}^s)_{\mu_s \mu_{s+1}}$$

$$= \mathbf{Tr} \left[\prod_s \mathbb{E}(\hat{I}^s) \right], \tag{2.31}$$

Nevertheless, we know that it is possible to orthogonalize the state as in Eq. (2.20), this fact gives us an enormous advantage for the calculation as follows

$$\langle \psi | \psi \rangle = \sum_{n_k \alpha_k \alpha_{k+1}} A^{n_k \star}_{\alpha_k \alpha_{k+1}} A^{n_k}_{\alpha_k \alpha_{k+1}} \equiv \vec{A}^\dagger \vec{A}$$

$$= \mathbf{Tr} \left[\mathbb{E}(\hat{I}^k) \right], \tag{2.32}$$

This is the site where we had located the information of the system since the matrices of the rest of the sites have been reduced to unitary matrices.

Nearest-neighbor operators.

Here, we analyze a couple of operators, $\langle \hat{O}_1^i \hat{O}_2^{i+1} \rangle$, acting on nearest-neighbor sites. Extending the previous calculation of on-site operators, one obtains

$$\langle \hat{O}_1^i \hat{O}_2^{i+1} \rangle = \mathbf{Tr} \left[\mathbb{E}^s \mathbb{E}^{s+1} \dots \mathbb{E}^{i-1} \mathbb{E}^i (\hat{O}_1^i) \mathbb{E}^{i+1} (\hat{O}_2^{i+1}) \right], \tag{2.33}$$

If instead, we orthogonalize on the site where the first operator is located, the expression simplifies, since all the matrices to the left of site i are reduced to the identity,

$$\langle \hat{O}_1^i \hat{O}_2^{i+1} \rangle = \mathbf{Tr} \left[\mathbb{E}^i (\hat{O}_1^i) \mathbb{E}^{i+1} (\hat{O}_2^{i+1}) \right]. \tag{2.34}$$

Correlation functions.

The calculation of correlations is very important in one-dimensional quantum systems, such as the single-particle correlation function discussed in the previous chapter. Here, we use a general expression as follows

$$G_\Delta = \langle \hat{O}_1^s \, \hat{O}_2^{s+\Delta} \rangle,$$

where the operators $\hat{O}_1^s$ and $\hat{O}_2^{s+\Delta}$ are independent operators that act on the sites s and $s + \Delta$ respectively. The average is performed on $|\psi\rangle$ and for simplicity, we orthogonalize the state collecting the information at the site s, where the first observable of the correlation is acting. By making use of

the orthogonal matrices, the correlation function is written as follows and depicted as is shown below,

$$\langle \hat{O}_1^s \hat{O}_2^{s+\Delta} \rangle = \text{Tr} \left[\mathbb{E}^s(\hat{O}^s) \left(\prod_{k=s+1}^{s+\Delta-1} \mathbb{E}^k(\hat{I}) \right) \mathbb{E}^{s+\Delta}(\hat{O}^{s+\Delta}) \right]. \tag{2.35}$$

Here, we have used the fact that all the matrices outside the interval $[s, s+\Delta]$ are identity matrices and therefore, all the transfer matrices related to those sites are equal to the unity.
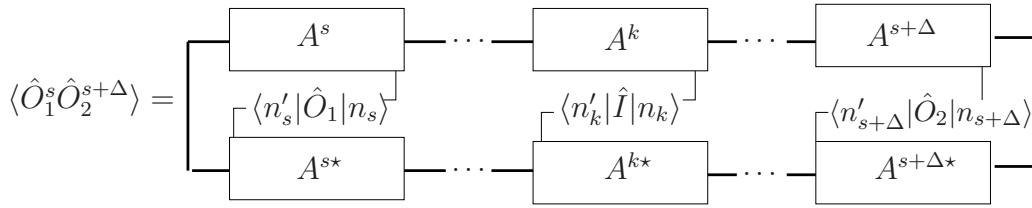
The diagram shows explicitly the complexity of the correlation function calculations, even with the advantage of the orthonormalization of the MPS state.

2.1.3 Variational MPS method

In this section, we concentrate in retrieving the ground state of a given Hamiltonian by solving the Schrödinger equation

$$\hat{H}|\psi\rangle = E_0|\psi\rangle. \tag{2.36}$$

We use the MPS representation of the state $|\psi\rangle = \sum A_{\alpha_s \alpha_{s+1}}^{n_s} |\alpha_s\rangle |n_s\rangle |\omega_{\alpha_{s+1}}\rangle$. We already saw that it depends explicitly on the matrix $\mathbb{A}^s$ located in the site s where the information is store. Since $|\psi\rangle = |\psi(\mathbb{A}^s)\rangle$, we rewrite the Schrödinger equation making explicit the dependency,

$$\hat{H}^s|\psi(\mathbb{A}^s)\rangle = E_0|\psi(\mathbb{A}^s)\rangle. \tag{2.37}$$

The variational method is employed to find the the lowest eigenstate, i.e. the ground state of $\hat{H}$,

$$\langle \psi(\mathbb{A}^{s\dagger})|\hat{H}|\psi(\mathbb{A}^s)\rangle = E_0 \langle \psi(\mathbb{A}^{s\dagger})|\psi(\mathbb{A}^s)\rangle. \tag{2.38}$$

In the general case, when the state is not orthonormalized, the eigenenergy is defined as

$$E_0 = \frac{\langle \psi(\mathbb{A}^{s\dagger})|\hat{H}|\psi(\mathbb{A}^s)\rangle}{\langle \psi(\mathbb{A}^{s\dagger})|\psi(\mathbb{A}^s)\rangle} = \frac{\vec{A}^{s\dagger}\mathcal{H}^s\vec{A}^s}{\vec{A}^{s\dagger}\vec{A}^s}, \tag{2.39}$$

where we had used the Eq. (2.32) and in a similar way we have for the denominator $\langle \psi(\mathbb{A}^{s\dagger})|\hat{H}^s|\psi(\mathbb{A}^s)\rangle = \sum A_{\alpha_s' \alpha_{s+1'}}^{n_s'^*} H_{n_s' n_s *} A_{\alpha_s \alpha_{s+1}}^{n_s} = \vec{A}^{s\dagger}\mathcal{H}^s\vec{A}^s$.

The minimization of the energy is performed by deriving with respect to $\vec{A}^{s\dagger}$:

$$\frac{\partial E_0(\vec{A}^{s\dagger})}{\partial \vec{A}^{s\dagger}} = \frac{\mathcal{H}^s \vec{A}^s (\vec{A}^{s\dagger} \vec{A}^s) - \vec{A}^s (\vec{A}^{s\dagger} \mathcal{H}^s \vec{A}^s)}{(\vec{A}^{s\dagger} \vec{A}^s)(\vec{A}^{s\dagger} \vec{A}^s)}$$

$$= \frac{1}{\vec{A}^{s\dagger} \vec{A}^s} \left(\mathcal{H}^s \vec{A}^s - E_0 \vec{A}^s \right) = 0. \tag{2.40}$$

We assume that $\vec{A}^{s\dagger} \vec{A}^s \neq 0$ and in reality this internal product is the unity for an orthonormalized state. To minimize the energy, we solve the eigensystem

$$\mathcal{H}^s \vec{A}^s = E_0 \vec{A}^s. \tag{2.41}$$

The minimization procedure is sketched in Fig. 2.2. In the following the algorithm is clarified in detail:

1. Start with the orthogonalization of the state $|\psi\rangle$ to a extreme site $s = 1$ or $s = L$ and obtain $\vec{A}^s$.

2. Calculate the Hamiltonian matrix $\mathcal{H}^s$ for the same site of the previous step.

3. Solve the eigensystem, Eq. (2.41), and choose the eigenvector that correspond to the lowest eigenenergy. This new vector $\vec{A}_0^s$ is used to update $\vec{A}^s$.

4. Move to the next site, this is done by performing a SVD, in this way the system is orthogonalized to the site $s + 1$ if one is moving to the right direction otherwise to the site $s - 1$. Special cases are $s = L$ for the sweep to the right and $s = 1$ for the sweep to the left. In those cases, one has to be careful to reverse the direction. Thus, one goes back-and-forth throughout the chain.

5. Check the change in the energy E_0 at each site. When the difference between the previous and current site energy is equal to a predetermined numerical threshold, for instance $\epsilon \sim 10^{-6}$, we consider that the system has converged. To be more accurate, this convergence can be asked for at least a complete sweep along the chain. If the convergence is not reached yet, the algorithm goes to step (2) and continues the process.
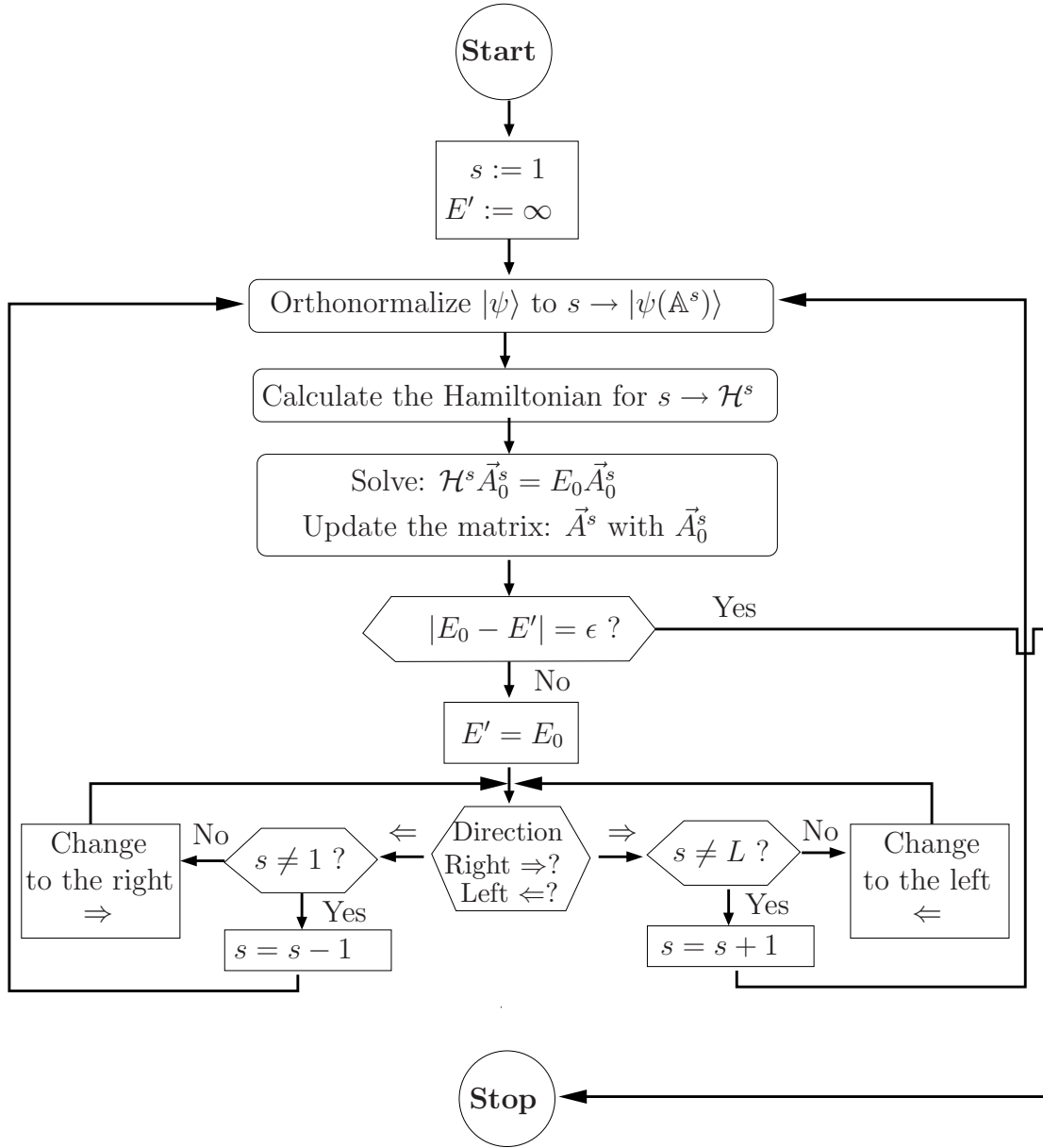
FIGURE 2.2: Flow diagram of the variational MPS method. The different steps are explained in the text.

2.1.4   Time-evolving block decimation (TEBD) algorithm

We concentrate now on the dynamics of a one-dimensional quantum many-body system. The time evolution is given by the time-dependent Schrödinger equation whose solution is given by

$$|\psi(t)\rangle = e^{-it\hat{H}}|\psi(0)\rangle. \tag{2.42}$$

Up to now, no constraints about the structure of the Hamiltonian have

been done. Henceforth, in order to be able to use the TEBD algorithm [119], the considered Hamiltonians should have at most nearest-neighbor interactions of the form

$$\hat{H} = \sum_i \hat{H}_1^{[i]} + \sum_i \hat{H}_2^{[i,i+1]}. \tag{2.43}$$

Now, it is possible to decompose $\hat{H}$ as a sum of two non-commuting terms, $\hat{H} = \hat{H}^e + \hat{H}^o$, where

$$\hat{H}^e \equiv \sum_{even\ i} (\hat{H}_1^{[i]} + \hat{H}_2^{[i,i+1]}) = \sum_{even\ i} \hat{H}^{e[i]},$$

$$\hat{H}^o \equiv \sum_{odd\ i} (\hat{H}_1^{[i]} + \hat{H}_2^{[i,i+1]}) = \sum_{odd\ i} \hat{H}^{o[i]}. \tag{2.44}$$

The even and odd labels refer to the pairs of sites that have as first and even and odd position in the chain. This configuration is illustrated in the following sketch, where the odd pairs are shown in blue while the even ones are shown in green.
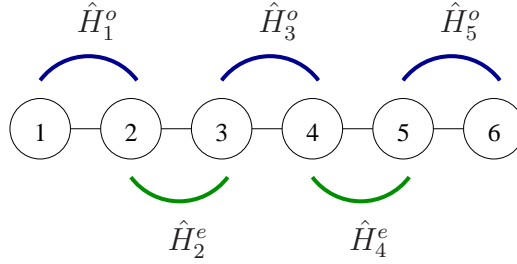
When two couples of operators do not share a site, they commute and satisfy $[\hat{H}^{e[i]}, \hat{H}^{e[i']}] = [\hat{H}^{o[i]}, \hat{H}^{o[i']}] = 0$.

Suzuki-Trotter decomposition [129] represents a general way of writing exponential operators:

$$e^{(A+B)} = \lim_{n \to \infty} (e^{\frac{A}{n}} e^{\frac{B}{n}})^n \tag{2.45}$$

This decomposition up to second order is given by

$$e^{-i\hat{H}\delta t} = e^{A\delta/2} e^{B\delta} e^{A\delta/2}. \tag{2.46}$$

plus corrections terms which vanish in the limit $\delta \to 0$. Here we consider δ to be small and positive. By using the second order Trotter expansion, the time-evolution operator $\hat{U}(\Delta t)$ is expressed as follows

$$\hat{U}(\Delta t) = e^{-\frac{i}{\hbar}\hat{H}\Delta t} = e^{-\frac{i}{\hbar}(\hat{H}^e + \hat{H}^o)\Delta t}$$

$$\approx \left[e^{-\frac{i}{\hbar}\hat{H}^e \Delta t/2} \right] \left[e^{-\frac{i}{\hbar}\hat{H}^o \Delta t} \right] \left[e^{-\frac{i}{\hbar}\hat{H}^e \Delta t/2} \right]$$

$$\approx \prod_{s(even)} e^{-\frac{i}{\hbar}H_s^e \Delta t/2} \prod_{s(odd)} e^{-\frac{i}{\hbar}H_s^o \Delta t} \prod_{s(even)} e^{-\frac{i}{\hbar}H_s^e \Delta t/2}. \tag{2.47}$$

We end up with a time evolution operator $\hat{U}_s^\nu = exp(-\frac{i}{\hbar}\hat{H}_s^\nu \Delta t)$ that acts in two sites $s, s+1$. The parity ν can be either even or odd. For the even case the time step is half of the odd case due to the second order decomposition.

How to apply the time evolution operator to a MPS.

Let us apply the decomposed operator $\hat{U}_s^\nu$ on a pair of sites $(s, s+1)$ for one time step Δt. In this case, it is convenient to write the MPS leaving the basis for this couple of sites explicitly

$$
\begin{aligned}
|\psi(t + \Delta_s^\nu t)\rangle &= \hat{U}_s^\nu(\Delta t)|\psi(t)\rangle \\
&= \hat{U}_s^\nu(\Delta t)\sum A_{\alpha_s\alpha_{s+1}}^{n_s} V_{\alpha_{s+1}\alpha_{s+2}}^{n_{s+1}\dagger}|\alpha_s\rangle|n_s n_{s+1}\rangle|\omega_{\alpha_{s+2}}\rangle.
\end{aligned} \tag{2.48}
$$

The operator acts from the left and goes directly to s with the advantage that the state remains orthogonal until this site.

$$
\begin{aligned}
|\psi(t + \Delta_s^\nu t)\rangle &= \sum A_{\alpha_s\alpha_{s+1}}^{n_s} V_{\alpha_{s+1}\alpha_{s+2}}^{n_{s+1}\dagger}|\alpha_s\rangle\hat{U}_s^\nu|n_s n_{s+1}\rangle|\omega_{\alpha_{s+2}}\rangle \\
&= \sum A_{\alpha_s\alpha_{s+1}}^{n_s} V_{\alpha_{s+1}\alpha_{s+2}}^{n_{s+1}\dagger}|\alpha_s\rangle\hat{I}\,\hat{U}_s^\nu|n_s n_{s+1}\rangle|\omega_{\alpha_{s+2}}\rangle \\
&\qquad \text{with} \quad \hat{I} = \sum_{n_s', n_{s+1}'}|n_s' n_{s+1}'\rangle\langle n_s' n_{s+1}'| \\
&= \sum \underbrace{A_{\alpha_s\alpha_{s+1}}^{n_s'} \mathcal{U}_{n_{s+1}' n_{s+1}}^{n_s'\ n_s} V_{\alpha_{s+1}\alpha_{s+2}}^{n_{s+1}'\dagger}}|\alpha_s\rangle|n_s n_{s+1}\rangle|\omega_{\alpha_{s+2}}\rangle \\
&= \sum \Theta_{\alpha_s\alpha_{s+2}}^{n_s n_{s+1}}|\alpha_s\rangle|n_s n_{s+1}\rangle|\omega_{\alpha_{s+2}}\rangle.
\end{aligned} \tag{2.49}
$$

Where the object Θ is calculated by the following operation

$$
\Theta_{\alpha_s\alpha_{s+2}}^{n_s n_{s+1}} = \sum_{\substack{n_s' n_{s+1}' \\ \alpha_{s+1}}} A_{\alpha_s\alpha_{s+1}}^{n_s'} \mathcal{U}_{n_{s+1}' n_{s+1}}^{n_s'\ n_s} V_{\alpha_{s+1}\alpha_{s+2}}^{n_{s+1}'\dagger}. \tag{2.50}
$$

In the next step, we perform the singular value decomposition to the Θ matrix. Taking into account that this matrix has 4 indexes, we regroup them as $\eta = (n_s, \alpha_s)$ and $\eta' = (n_{s+1}, \alpha_{s+2})$ in such way that the SVD looks like

$$
\begin{aligned}
\Theta_{\alpha_s\alpha_{s+2}}^{n_s n_{s+1}} = \Theta_{\eta\eta'} &= \sum_{\tilde{\alpha}_{s+1}=1}^{\chi'} \tilde{U}_{\eta\tilde{\alpha}_{s+1}} \underbrace{D_{\tilde{\alpha}_{s+1}} V_{\tilde{\alpha}_{s+1}\eta'}^\dagger} \\
&= \sum_{\tilde{\alpha}_{s+1}=1}^{\chi'} \tilde{U}_{\alpha_s\tilde{\alpha}_{s+1}}^{n_s} A_{\tilde{\alpha}_{s+1}\alpha_{s+2}}^{n_{s+1}}.
\end{aligned} \tag{2.51}
$$

The $\tilde{U}$ matrix replaces the $\mathbb{A}^s$ while the product $DV^\dagger$ becomes the new $\mathbb{A}^{s+1}$ matrix. This process is depicted in the following diagram in three steps. First,
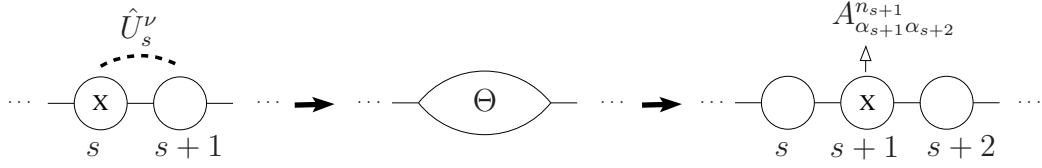
the orthogonalization of the state in the site s. Second, the calculation of the Θ-matrix after the time evolution operator. And third, the SVD performed to Θ in order to allocate the information on the site $s + 1$.

Note that in general, the truncation of the basis before the evolution is not equal to the truncation for the evolved state, it means $\chi_{old} \neq \chi'$. Actually, the entanglement of the system increases in a time evolution operation. Therefore, the truncation parameter should be also updated after performing a time step. The optimal value of the χ-parameter is calculated by

$$\sum_{i=1}^{\chi'} D_i^2 = 1 - \epsilon, \tag{2.52}$$

where $\epsilon << 1$ is given by the desired precision.

This procedure lead us to the single step time-evolved MPS state of the form

$$|\psi(t + \Delta_s^\nu t)\rangle = \sum \tilde{U}_{\alpha_s \tilde{\alpha}_{s+1}}^{n_s} A_{\tilde{\alpha}_{s+1} \alpha_{s+2}}^{n_{s+1}} |\alpha_s\rangle |n_s n_{s+1}\rangle |\omega_{\alpha_{s+2}}\rangle \tag{2.53}$$

The last stage is to orthogonalize the state to the site $s+2$. Leaving the state ready to apply the evolution to the next couple of sites. Thus, another SVD is performed to pass the information from the site $s+1$ to $s+2$. The expression of the state and the sketch of this process are presented in the following:

$$\begin{aligned}|\psi(t + \Delta_s^\nu t)\rangle &= \sum \tilde{A}_{\tilde{\alpha}_{s+1} \alpha_{s+2}}^{n_{s+1}} V_{\alpha_{s+2} \tilde{\alpha}_{s+3}}^{n_{s+2}\dagger} |\tilde{\alpha}_{s+1}\rangle |n_{s+1} n_{s+2}\rangle |\omega_{\alpha_{s+2}}\rangle \\ &= \sum U_{\tilde{\alpha}_{s+1} \alpha_{s+2}}^{n_{s+1}} A_{\alpha_{s+2} \alpha_{s+3}}^{n_{s+2}} |\tilde{\alpha}_{s+1}\rangle |n_{s+1} n_{s+2}\rangle |\omega_{\alpha_{s+2}}\rangle. \end{aligned} \tag{2.54}$$
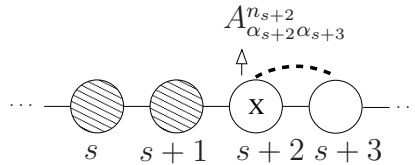
The algorithm is repeated evolving all the even and odd sites. Figure 2.3 presents a flow diagram for the TEBD algorithm. It presents the process for a chosen parity of the Hamiltonian and therefore the time evolution operator.
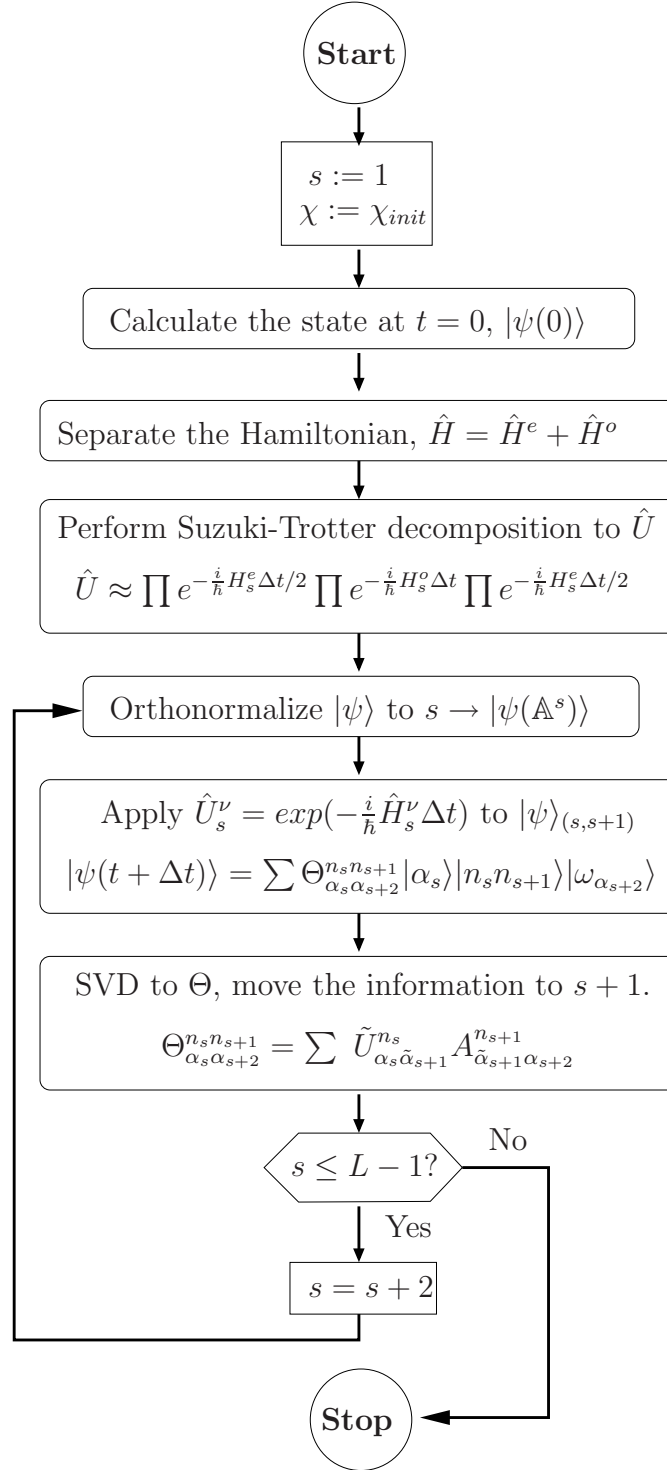
FIGURE 2.3: Flow diagram of the TEBD algorithm based in the MPS formalism. The scheme shows the process for a given parity ν of the Hamiltonian.

2.2   The Lanczos method

The Lanczos method is a technique that can be used to solve symmetric eigenproblems

$$H\vec{x} = r(\vec{x})\vec{x}. \tag{2.55}$$

The method involves the tridiagonalization of the given Hamiltonian matrix H. Important information about the extremal eigenvalues of H can be obtained, this makes the Lanczos algorithm particularly useful where a set of largest or smallest eigenvalues of H are desired. The basic idea of the Lanczos method lies on the fact that the special Krylov space is constructed where the Hamiltonian H has a tridiagonal form. It is achieved by projecting the original H onto that subspace. Afterwards one can easily diagonalize. If m is equal to the dimension of the Hilbert space, the approach is equivalent to a full diagonalization of H. However, one of the advantages of this method is that accurate enough information about the ground-state can be retrieved after a small number of iterations [130].

The system length-size one can reach with this method depends strongly on the amount of states one allow per lattice site. It has been shown for spin-3/2 systems that one can get until 14 sites [131], whereas for spin-1 it is possible to reach 16 sites [132]. Since the algorithm depends strongly on the basis size, the implementation of the problem symmetries is undoubtedly a very good tool to reduce the basis. A few examples are listed below:

- Particle number conservation:

  The Hamiltonians we use in the frame of this work commute with the particle number operator. One can always work in the micro- or canonical- ensemble. This allows us to work in the manifold of a given number of particles and thus the reduction of the basis is guaranteed.

- Symmetry implementation:

  A representation of a group is a map which preserves multiplication and sends a member of the group to a linear operator on a vector space. The dimension of the representation is the one of the vector space. Not all representations yield new information since they can be decomposed into direct product of smaller dimension representation. The irreducible representation is, of course, the one that cannot be broken down into a smaller representation.

  If there is a specific symmetry preserved in the system and it is not broken under any consideration, for instance during a time-evolution or by the variation of system parameters, then one can exploit such symmetry in the numerical simulations.

The idea is to find irreducible group representations inside the extended representation of the problem. Once these observables have been identified, one can work in the manifold that contains them exclusively. As a consequence a considerable reduction of the basis size is achieved.

Part I

Correlation dynamics in quenched strongly-correlated bosons in 1D optical lattices

Correlation dynamics of spinless bosons in 1D optical lattices

We analyze by means of MPS simulations the correlation dynamics of strongly-correlated superfluid Bose gases in one-dimensional time-dependent optical lattices. We show that, as for the case of abrupt quenches, a quasi-adiabatic modulation of the lattice is characterized by a relatively long transient regime for which quasi-local single-particle correlation functions have already converged to a new equilibrium, whereas long-range correlations and particularly the quasi-condensate fraction may still present a very significant dynamics well after the end of the lattice modification. We also address the issue of adiabaticity by considering the fidelity between the time-evolved state and the ground-state of the final lattice.

3.1 Motivation

The high tunability and long characteristic time scales of ultra-cold gases offer an ideal scenario to investigate non-equilibrium dynamics in a way not available in traditional condensed matter systems. In particular, lattice hopping rates may be easily tuned by modulating the intensity of the lasers creating the optical lattice, and the interactions may be also modified in real time by means of Feshbach resonances and time-dependent magnetic fields. These changes may be produced fast enough to be considered as a sudden quench. These quenches have attracted a growing attention in recent years, in particular in what concerns the evolution of correlations and possible equilibration after a quench [133–140]. Thermalization (or actually the absence of it) was recently studied in a milestone experiment performed in nearly integrable one-dimensional Bose gases by Kinoshita et al [141].

On the contrary, if the modification of the system is very slow, much slower than the tunneling rate, one can in principle assume the evolution as adiabatic [142–144]. The issue of adiabaticity is however far from trivial, especially in low dimensional gapless systems, as recently discussed by Polkovnikov and Gritsev [145]. Interestingly, in the so-called non-adiabatic scenarios, the adiabatic limit cannot be reached no matter how slow the change is introduced. Although this result is strictly speaking only applicable in integrable harmonic systems, it was shown in Ref. [145] that this non-adiabatic scenario may be

obtained by considering an initial non-interacting 1D or 2D Bose gas in a lattice under a slow increase of the interaction strength. The harmonic approximation remains accurate as long as $U_0/tn_0 \ll 1$, where (see below) U_0 characterizes the on-site interactions, t is the hopping rate, and n_0 is the filling factor. In this regime the truncated Wigner approximation (TWA), plus an additional first-order quantum correction, allows for an accurate description of the correlation dynamics [145].

In this chapter we study the correlation dynamics of a superfluid Bose gas in a 1D lattice during and after a modification of the lattice depth. Contrary to the case of a quench [133–140], the modification is not considered as instantaneous, but rather a finite linear ramp. In addition, contrary to the (quasi-)harmonic scenario discussed by Polkovnikov and Gritsev [145] we are here particularly interested in the correlation dynamics in the deeply quantum regime $U_0 \gg t$ at low filling $n_0 < 1$, where the system remains superfluid although strongly correlated. In this regime, quantum fluctuations are dominant, and hence TWA approximation cannot be employed to describe the dynamics. To this aim, we employ time-dependent MPS techniques, which allow us to study accurately relatively large systems.

We show that, as for the case of abrupt quenches the correlation dynamics is characterized by an intermediate regime, in which quasi-local correlations have converged to a new equilibrium, although long-ranged correlations, and in particular the quasi-condensate fraction still presents an observable dynamics (which keeps evolving well after the end of the slow ramp). Since the system is not integrable, eventually a new equilibrium is reached. We analyze this final state and the adiabaticity of the modification by means of the transferred energy and the fidelity with respect to the expected ground state solution.

The scheme of this chapter is as follows. Sec. 3.2 introduces the model under consideration and the numerical methods employed. Sec. 3.3 is devoted to the analysis of correlation functions and quasi-condensate fraction. Sec. 3.4 studies the fidelity of the final evolved state with respect to the ground state of the final Hamiltonian. Finally, Sec. 3.5 summarizes our conclusions.

3.2 System and methodology

In the following we consider spinless bosons in a deep lattice constrained to the lowest energy band. In this regime, the free energy of the system is described by the BHH

$$\hat{F} = \hat{H} - \mu\hat{n} = \sum_i \left[-t(\tau)\left(\hat{b}_i^\dagger \hat{b}_{i+1} + h.c\right) + \frac{U_0}{2}\hat{n}_i\left(\hat{n}_i - 1\right) - \mu\hat{n}_i \right], \quad (3.1)$$

where $\hat{b}_i$ ($\hat{b}_i^\dagger$) is the annihilation (creation) operator of a boson at the i-th site, $\hat{n}_i$ is the corresponding number operator, μ is the chemical potential, $t(\tau)$ is the time-dependent tunneling amplitude between neighboring sites, and $U_0 > 0$ is the repulsive on-site interaction. We consider in the following that at the initial time, $\tau = 0$, the system is in the ground-state for the initial hopping value $t_i = t(0)$.

As mentioned above, the system may be driven out of equilibrium either by modifying the hopping rate, as we consider here, or by modifying the interaction rate, e.g. by means of Feshbach resonances. In the following we consider a time-dependent lattice depth, which leads to a linear-ramp of the form,

$$t(\tau) = t_i + (t_f - t_i)\frac{\tau}{\tau_r}, \tag{3.2}$$

for an initial time interval $0 < \tau < \tau_r$, where t_f is the final hopping. For $\tau > \tau_r$ the system evolves at a constant $t = t_f$. We let the system evolve for sufficiently large post-ramp times such that the quantities of interest enter into a new equilibrium.

We consider in our calculations a lattice with $L = 60$ sites with open boundary conditions, which is sufficiently large to minimize finite-size effects at the lattice center, where we evaluate the correlations discussed below. In our time-evolution simulations, we work in the canonical ensemble with two different total number of particles, $N = 20$ which leads to an average lattice-site filling $\bar{n} \sim 0.3$ below half-filling (HF), and $N = 50$ which leads to $\bar{n} \sim 0.8$, i.e. above HF.

In all simulations discussed below we considered $t_i = 0.1375U_0$ and $t_f = 0.2500U_0$. These values were chosen relatively close to each other to allow for the convergence to a new equilibrium discussed below within a numerically available evolution time. In spite of that, these values are sufficiently different to allow for the study of the ramping adiabaticity. Note that the hopping rates t_i and t_f are rather low and comparable to the critical tunneling where the tip of the lowest MI lobe is located, which for 1D is found at $t \simeq 0.2U_0$. In that regime quantum fluctuations are highly relevant, but due to the low filling $\bar{n}$ considered, the system remains highly-correlated within the SF regime.

In our calculations we first obtained the ground-state for $t = t_i$ at $\tau = 0$ using the variational MPS ansatz. Here we use $\chi = 25$ to calculate this initial state. For the local basis, the maximal number of atoms per site considered is $d = 2$, which for our parameters it is safely assumed. Thereafter, we evolve the system in real time for $\tau > 0$ by means of the TEBD method, updating χ when it is necessary.
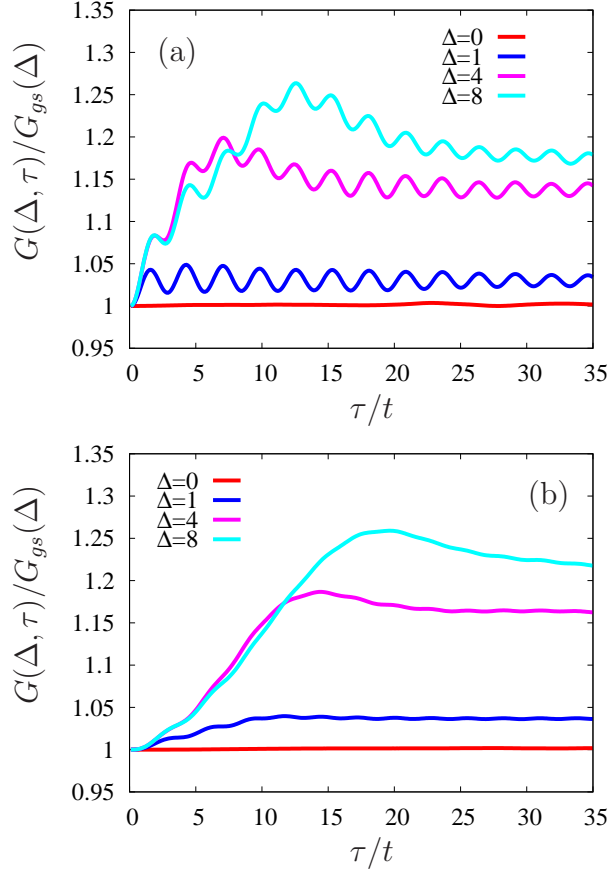
FIGURE 3.1: Time-evolution of several correlation functions considering a ramp-time of (a) $\tau_r = 0.2t_f$ and (b) $\tau_r = 10.0t_f$. The used density population is $\bar{n} = 0.3$.

3.3   Correlation dynamics and quasi-condensate fraction

In this section, we study the single-particle correlation function, defined in the introduction by the Eq. (1.11). In the following we are particularly interested on the dynamics of the SPCF restricting ourselves to the middle of the lattice to avoid problems coming from the borders, for this respect we use

$$G(\Delta, \tau) = \langle \hat{b}_0^\dagger \hat{b}_\Delta \rangle, \tag{3.3}$$

where the angular brackets denote averaging over the evolved state. The creation operator is taken at the initial site of a segment in the middle of the lattice, namely position zero, and the annihilation operator is acting in the Δ-neighbor site.

We have analyzed the evolution of $G(\Delta, \tau)/G(\Delta, \tau = 0)$ for different values of Δ and different ramping times τ_r. Fig. 3.1(a) exemplifies the case of an
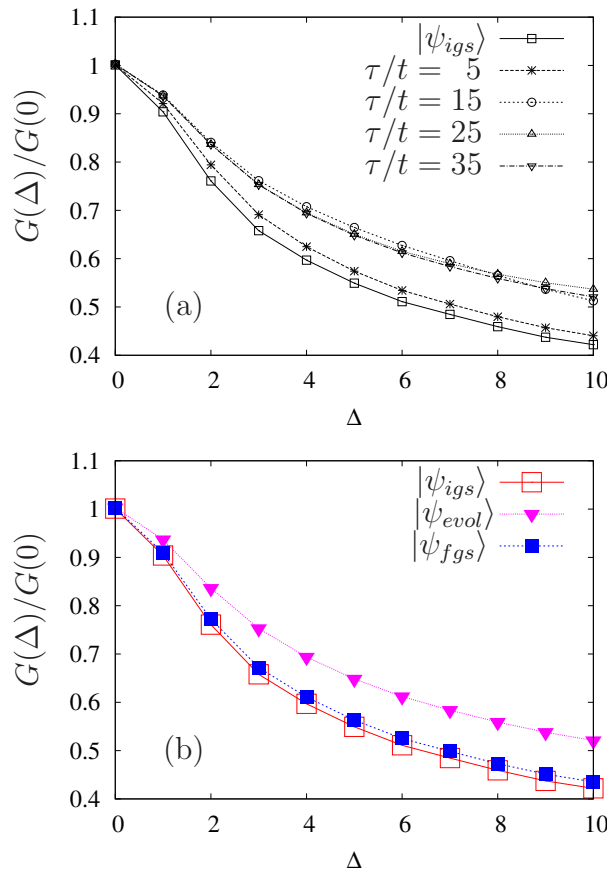
FIGURE 3.2: Spatial correlation as a function of Δ. (a) Shows the initial state $|\psi_{igs}\rangle$ and evolved states at several times. (b) Presents the comparison between $|\psi_{igs}\rangle$, the ground-state $|\psi_{fgs}\rangle$ of the final configuration and the evolved state $|\psi_{evol}\rangle$ after $\tau/t = 35$ for a ramp time of $\tau_r = 10.0t_f$.

abrupt ramp which is basically an instantaneous quench, with $\tau_r = 0.2t_f$, whereas Fig. 3.1(b) shows typical results observed for a mild ramp, in this case $\tau_r = 10.0t_f$. Both cases are calculated at a filling factor $\bar{n} = 0.3$. Note that $G(\Delta, \tau)$ shows in both cases a significant dynamics following the linear ramp. Moreover, due to number conservation the density, i.e. $\Delta = 0$, is unaffected by the lattice modulation.

Both abrupt and slow ramps lead to an evolution of the correlations characterized by an initial short-time scale, followed by an eventual convergence into a new equilibrium at longer times. Observe, however, that the correlation dynamics, following the abrupt quench, presents a short-time modulation which persists well within the quasi-equilibrium region [138]. This short-time evolution of the correlations continues well after the end of the ramp ($t = t_r$), even for the mild ramp. Notice also that short-distance correlations, in partic-

ular $\Delta = 1$, converge significantly quicker than correlations at larger distances. As a consequence the lattice bosons experience a transient regime characterized by a quasi-equilibrium of local or quasi-local observable coexisting with out-of-equilibrium global properties.

After this transient regime the system reaches a final equilibrium, characterized by an equilibrium correlation. To emphasize this fact, we plot in Fig. 3.2(a) the correlation function as function of Δ at different times. The time step used in the evolution is $\delta\tau/t = 0.1$ and the modulation ramp time is $\tau_r = 10.0t_f$. In the graph, we definitely see that $G(\Delta)$ continues evolving after stopping the ramping until its shape saturates. Nevertheless, this saturation does not arrive to the expected ground state configuration that one gets for the final parameter set, i.e. $t = t_f$. The distinction between the initial ground state $|\psi_{igs}\rangle$, the saturated time-evolved state $|\psi_{evol}\rangle$ and the ground state, $|\psi_{fgs}\rangle$, calculated for t_f is clearly seen in Fig. 3.2(b).

The quasi-condensate fraction

As we already mention in the introduction, this fraction is defined as the largest eigenvalue λ_0 of the density matrix $\langle \hat{b}_i^\dagger \hat{b}_j \rangle$ of the system [146], and hence may be considered a global property of the system, influenced by correlations at any available Δ. Although strict condensation is prevented in 1D, quasi-condensation, characterized by a distinct finite λ_0, is possible in finite systems.

We are interested to analyze the transient regime, where observables in equilibrium and out-of-equilibrium coexist. To do so, let us study the time evolution of the normalized quasi-condensate fraction $\lambda_0(\tau)/\lambda_0(0)$. Note that this quantity evolves at a much longer time scale than local or quasi-local correlations. It is shown in Fig. 3.3(a) for a filling factor $\bar{n} = 0.3$ and two different ramping modulations $\tau_r = 0.2t_f$ and $\tau_r = 10t_f$. The evolution takes much larger than the ramp time even in the mild-ramping case, therefore for our typical calculations, it has not yet fully converged.

To determine the variation time scale of the different correlation functions, we analyze the evolution of the quasi-condensate fraction, this time, taking into account different filling factors. Thus, the transient regime time becomes also particularly clear. The figure 3.3(b) shows the evolution of the quasi-condensate fraction for the case of an average filling factor $\bar{n} = 0.8$ compared to the case with $\bar{n} = 0.3$, using the mild ramp $t_r = 10t_f$. At higher densities the quasi-equilibrium is reached sooner for the same ramping, even more, the same behavior is observed for $G(\Delta)$. As it is shown in Fig. 3.3(b), we may define a typical time scale for the variation of λ_0, which is $t(\bar{n} = 0.3) = 17.9$ and $t(\bar{n} = 0.8) = 12.9$.
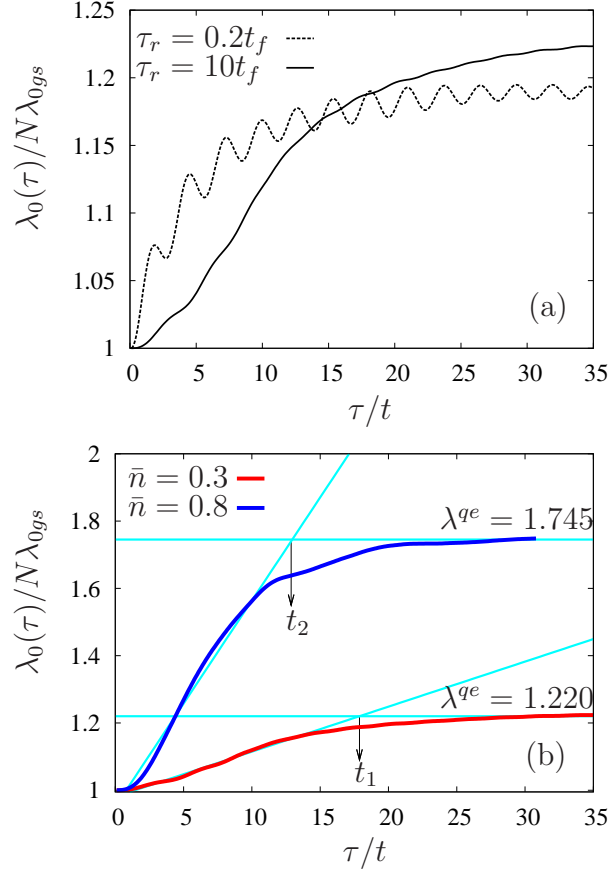
FIGURE 3.3: Time evolution of the quasi-condensate fraction. (a) For two different ramp times, an abrupt ramp $\tau_r = 0.2t_f$ and a mild ramp $\tau_r = 10t_f$. (b) For two different fillings, $\bar{n} = 0.3$ and $\bar{n} = 0.8$, using the mild ramp. The horizontal lines denote the tended quasi-equilibrium values (λ^{qe}). The dashed lines fit the initial curve stretch and the intersection points are defined as a qualitative estimation of the λ_0 variation time, $t_1(\bar{n} = 0.3) = 17.9$ and $t_2(\bar{n} = 0.8) = 12.9$. The plot is in units of λ_{0gs} where λ_{0gs} is the quasi-condensate fraction of the initial ground-state.

3.4 Adiabaticity analysis

3.4.1 Fidelity

A good tool for the analysis of the adiabaticity of the ramping is provided by the fidelity [147]

$$\mathcal{F} = |\langle \psi_{fgs} | \psi(\tau) \rangle|^2, \tag{3.4}$$

between the time-evolved state $|\psi(\tau)\rangle$ and the expected ground-state $|\psi_{fgs}\rangle$ calculated with the final $t = t_f$. The fidelity $\mathcal{F}$ is an interesting figure of
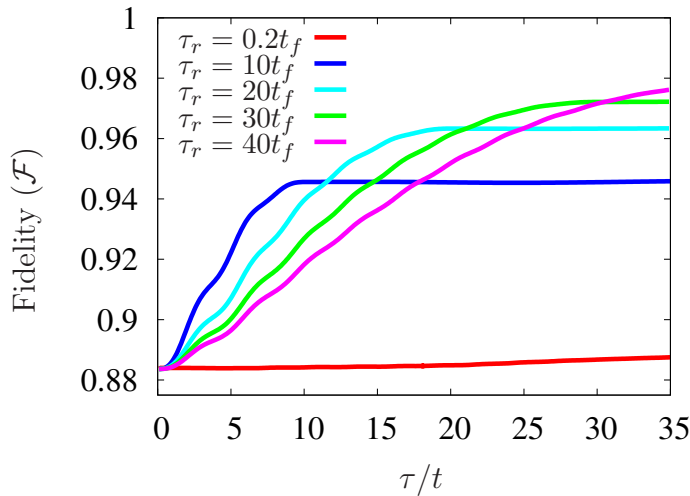
FIGURE 3.4: Fidelity of the time-evolved state to the ground state at the end of the lattice modulation for several time modulations.

merit for the adiabaticity of the ramping, since contrary to other figures, as the correlation functions discussed above, it just evolves while the ramping is on, since after the ramping the eigenstates of the final Hamiltonian are of course stationary, and consequently $\mathcal{F}$ remains constant. Hence, although other quantities require a rather long waiting time for comparing the final state and the time-evolved one, $\mathcal{F}$ provides an answer at the relatively short-time scale, of the order of τ_r (see Fig. 3.4). As expected the abrupt ramping $\tau_r = 0.2t_f$ leads basically to an instantaneous projection of the initial ground-state $|\psi_{igs}\rangle$ into $|\psi_{fgs}\rangle$, note that the overlapping is already rather large, 88%, due to the relative close values of t_i and t_f. One can also anticipate that the milder ramping approaches further to $|\psi_{fgs}\rangle$. However, the fidelity is still 5% off from $|\psi_{igs}\rangle$. Interestingly, this indicates that even very large ramping times, significantly larger than the hopping time and for a relatively small variation of $\Delta t = 0.1125U_0$, do not guarantee a perfect transfer into the ground state of the final configuration. The analysis of $\mathcal{F}$ for even milder ramps shows that milder ramps lead indeed to more adiabatic transfers, contrary to what may be expected in the harmonic regime [145].

3.4.2   Final energy

As mentioned above, the correlations $G(\Delta)$ approach at longer times to a new equilibrium. This new equilibrium is not that given by the expected ground state but by a new distribution with a higher energy. The analysis of the final energy after the ramping is shown in Fig. 3.5. Unfortunately, it does not provide an equally strict adiabaticity analysis as that of the fidelity, especially for situations as those discussed here, in which t_i and t_f possess relatively
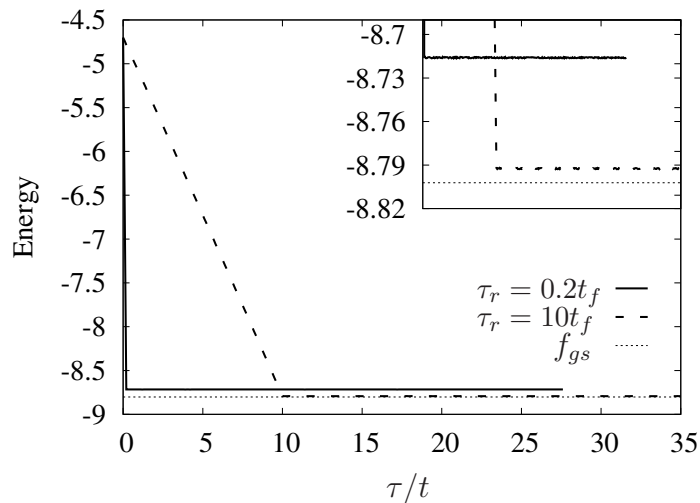
FIGURE 3.5: Ground state energy comparison between the abrupt and the mild ramps with the ground state at t_f.

close values. In our case, the difference between the energy of the system after the abrupt ramping and the one of $|\psi_{fgs}\rangle$ is less than 1%, whereas the time-evolution with the mild ramping provides a final energy less than 0.1% off than $|\psi_{fgs}\rangle$. Therefore, there is a hierarchy where the ground state has the lowest energy, the mild ramp has an intermediate one, and finally the state coming from the abrupt ramp has clearly the highest energy.

3.5   Conclusions

We have analyzed by means of MPS techniques the dynamics of correlation functions and quasi-condensate fraction of ultra-cold lattice bosons in the deeply correlated superfluid regime during and after a finite linear ramp modulation of the hopping rate. We have shown that the evolution is characterized by a transient non-equilibrium state in which quasi-local correlation functions have already converged into a new equilibrium whereas long-range correlations and the quasi-condensate fraction present still a significant time dependence. Additionally, we have analyzed the formation at a longer time scale of a new equilibrium from an initial gas at zero temperature. By considering the fidelity with respect to the ground state of the final configuration we have shown that even rather mild ramps do not fully guarantee a perfect loading of the new ground state. We have however shown that contrary to the harmonic regime [145] progressively milder ramps lead to a more adiabatic transfers.

Part II

Mott-insulator phases of spinor systems

Spinor gases and effective models

In this chapter, we discuss general concepts of spinor gases. Thereafter, we derive the low-energy effective spin Hamiltonian in the hard-core limit of up to one particle per site. We concentrate, in the Mott insulator regime with a small, but finite, atomic tunneling parameter, for repulsive interacting particles (either fermions or bosons) in the presence of a quadratic Zeeman coupling. The virtual tunneling induces effective spin-exchange interactions between the nearest-neighbor particles, leading to possible magnetic order phases. We also review the already known quantum phase diagrams in absence of external fields for spin-3/2 fermions and spin-1 bosons cases.

4.1 Spinor gases

As already mentioned, ultra-cold gases in optical lattices constitute an extraordinary tool for the analysis of strongly correlated systems under extremely well-controlled conditions [27, 28]. Spinor gases, formed by atoms with several internal states, are particularly interesting systems, since they constitute an ideal scenario to investigate the interplay between internal and external degrees of freedom. The competition between various energy scales such as short-range interactions, Zeeman effect, dipole-dipole interaction, and trapping leads to an exceeding rich physics.

One of the most interesting features of spinor gases is the presence of inter-atomic interactions that lead to spin-changing processes in which population is transferred coherently between different Zeeman sub-levels. This fascinating effect has attracted a large interest, mostly in the realm of spinor BEC [86, 148]. The breakthrough of spinor condensates came with the development of dipole traps, which made possible to confine all components of a spinor BEC. On the other hand, spinor fermions have recently become the focus of a rapidly growing interest, motivated by several experiments including two-component fermions [28] and the availability of multicomponent fermions [98] which present a wealth of novel phases.

4.1.1 Short-range interactions in spinor condensates

Let us start considering short-range interactions in spinor condensates which for the extremely low energies relevant in ultra-cold gases are dominated by two-body s-wave collisions. When two particles interact, their spins couple to form a total spin during the collision. Afterwards, the two spins decouple and the particles move away form each other. For two identical spin-S particles, the total spin is given by $\vec{F} = \vec{S}_1 + \vec{S}_2$, and the allowed total spins are $F = 2S, 2S - 1, ..., 0$. However, due to the symmetry (anti-symmetry) required for the total wavefunction by identical bosons (fermions), only F channels with symmetric(anti-symmetric) spin wavefunction are allowed for bosons (fermions), since the s-wave collision spatial wavefunction of two atoms is always symmetric. The short-range interaction conserves the total spin F.

An important feature of the short-range interactions is that due to their isotropy, they do not modify the spin projection of the pair along the quantization axis. This means that if the in-coming pair has spins $m_{F,1}$ and $m_{F,2}$ and the out-going one $m_{F,3}$ and $m_{F,4}$, then $m_{F,1} + m_{F,2} = m_{F,3} + m_{F,4}$, due to the magnetization conservation. Note that, this may be realized in two non-equivalent ways. One way is given by the so-called *spin-preserving* collisions, for which $m_{F,1} = m_{F,3}$ ($m_{F,1} = m_{F,4}$) and $m_{F,2} = m_{F,4}$ ($m_{F,2} = m_{F,3}$). Even more interesting, there is an alternative way in which the population of the different components is re-distributed while conserving the magnetization, the so-called *spin-changing* collisions. The later play a crucial role in the magnetic properties discuss in the present and following chapters.

The short-range interaction between two particles may be decomposed into contributions from the different channels in the form

$$\hat{V}(\vec{r}_1 - \vec{r}_2) = \delta(\vec{r}_1 - \vec{r}_2) \sum_{F=0}^{2S} g_F \hat{P}_F, \tag{4.1}$$

where the coupling strength for the F-channel is defined by

$$g_F = 4\pi\hbar^2 a_F/M, \tag{4.2}$$

with M the atomic mass and $\hat{P}_F$ is the projector operator onto a two-particle state with total spin-F:

$$\hat{P}_F = \sum_{m_F=-F}^{F} |F, m_F\rangle\langle F, m_F|. \tag{4.3}$$

For identical particles, the projector operators satisfy the following closure relation,

$$\hat{I} = \sum_{F=0}^{2S} \hat{P}_F. \tag{4.4}$$

On the other hand, since $\vec{S}_1 \cdot \vec{S}_2 = (\vec{F}^2 - \vec{S}_1^2 - \vec{S}_2^2)/2$, then

$$\hat{S}_i \cdot \hat{S}_2 = \frac{1}{2} \sum_{F=0}^{2S} \left(F(F+1) - 2S(S+1) \right) \hat{P}_F. \qquad (4.5)$$

Let us introduce as well the inverse relations, since they will be useful later on when deriving effective Hamiltonians. The projectors in terms of the spin operators are

$$\hat{P}_F = \alpha \prod_{s' \neq F} \left[\hat{S}_1 \cdot \hat{S}_2 - \frac{s'(s'+1)}{2} + S(S+1) \right],$$

where,

$$\qquad (4.6)$$

$$\alpha \prod_{s' \neq F} \left[\frac{F(F+1)}{2} + 2S(S+1) - \frac{s'(s'+1)}{2} \right] = 1.$$

As mentioned, multi-component quantum systems in optical lattices lead to a rich physic, which we explore in Thesis. We start from the most general Hamiltonian and derive the low energy effective spin Hamiltonian in the hard-core limit for repulsive interacting particles. In this limit there is exactly one particle per lattice site inside the Mott insulator regime. In other words, the "charge" degree of freedom is frozen out and only spin modes are considered. We consider fermionic (spin-3/2) and bosonic (spin-1) spinor systems in two different scenarios: in absence and in presence of a quadratic external coupling. The fermionic and bosonic effective Hamiltonians are presented for each scenario in the following. Moreover, we review as well, the ground state phases of each spinor system in absence of an external field. This is a warming-up for the wealth of magnetic properties coming out, in Chapters 5 and 6 for spin-3/2 and spin-1, respectively, due to the inclusion of the quadratic Zeeman coupling.

4.2 Spin-3/2 fermions in optical lattices

We consider spin-3/2 fermions colliding via s-wave scattering. As we already mentioned, the fermionic character of the particles requires the total wavefunction to be anti-symmetric, leading the spin wavefunction to be anti-symmetric. Therefore, from the Pauli exclusion principle, only two channels are open for collisions, the channels with total spin $F = 0$ and $F = 2$.

For a deep lattice and low filling the most generic Hamiltonian, describing four-component fermions with equal masses interacting via this contact potential, is

$$\hat{H}' = - t \sum_{m,i} [\hat{\psi}^\dagger_{m,i} \hat{\psi}_{m,i+1} + h.c.] - \mu \sum_{m,i} \hat{n}_{m,i} + q \sum_{m,i} m^2 \hat{n}_{m,i}$$
$$+ g_0 \sum_i \hat{P}^\dagger_{00,i} \hat{P}_{00,i} + g_2 \sum_{m_F,i} P^\dagger_{2m_F,i} P_{2m_F,i}, \tag{4.7}$$

where $\hat{\psi}_{m,i}$ annihilate fermions with spin m at site i, μ is the chemical potential, $\hat{n}_{m,j} = \psi^\dagger_{m,j} \psi_{m,j}$ is the particle number operator, the hopping rate between adjacent sites is t, q is quadratic Zeeman coupling strength, and $\hat{P}_{00,i}$ and $\hat{P}_{2m_F,i}$ are the projectors in the channels $F = 0$ and $F = 2$, respectively.

Rewriting explicitly the projector operators, the one-site interaction term of the Hamiltonian is given by

$$\hat{H}_I = - \mu \sum_{m,i} \hat{n}_{m,i} + q \sum_{m,j} m^2 \hat{n}_{m,j}$$
$$+ \sum_i \Bigg\{ G(1+g) \Big[\hat{\psi}^\dagger_{-\frac{3}{2}} \hat{\psi}^\dagger_{-\frac{1}{2}} \hat{\psi}_{-\frac{1}{2}} \hat{\psi}_{-\frac{3}{2}} + \hat{\psi}^\dagger_{-\frac{3}{2}} \hat{\psi}^\dagger_{\frac{1}{2}} \hat{\psi}_{\frac{1}{2}} \hat{\psi}_{-\frac{3}{2}}$$
$$+ \hat{\psi}^\dagger_{-\frac{1}{2}} \hat{\psi}^\dagger_{\frac{3}{2}} \hat{\psi}_{\frac{3}{2}} \hat{\psi}_{-\frac{1}{2}} + \hat{\psi}^\dagger_{\frac{1}{2}} \hat{\psi}^\dagger_{\frac{3}{2}} \hat{\psi}_{\frac{3}{2}} \hat{\psi}_{\frac{1}{2}} \Big]_i \tag{4.8}$$
$$+ \ G \Big[\hat{\psi}^\dagger_{-\frac{3}{2}} \hat{\psi}^\dagger_{\frac{3}{2}} \hat{\psi}_{\frac{3}{2}} \hat{\psi}_{-\frac{3}{2}} + \hat{\psi}^\dagger_{-\frac{1}{2}} \hat{\psi}^\dagger_{\frac{1}{2}} \hat{\psi}_{\frac{1}{2}} \hat{\psi}_{-\frac{1}{2}} \Big]_i$$
$$+ Gg \Big[\hat{\psi}^\dagger_{-\frac{3}{2}} \hat{\psi}^\dagger_{\frac{3}{2}} \hat{\psi}_{\frac{1}{2}} \hat{\psi}_{-\frac{1}{2}} + \hat{\psi}^\dagger_{-\frac{1}{2}} \hat{\psi}^\dagger_{\frac{1}{2}} \hat{\psi}_{\frac{3}{2}} \hat{\psi}_{-\frac{3}{2}} \Big]_i \Bigg\},$$

where G and g are functions of the scattering strengths $g_{0,2}$ defined by Eq. (4.2),

$$G = \frac{g_0 + g_2}{2} \quad \text{and} \quad g = \frac{g_2 - g_0}{g_0 + g_2}. \tag{4.9}$$

Henceforth, we employ G as unity ($G \equiv 1$). It is important to emphasize that g provides the spin-changing collision strength (note that spin-changing collisions are given by the last line of Eq. (4.8)).

We consider a balanced mixture of spin-3/2 fermions loaded in a 1D optical lattice [105–107, 110] with $N_m = N_{-m}$, where N_m is the number of fermions with spin projection m and the magnetization $\mathcal{M} \equiv \sum_m m N_m = 0$. Note that the interactions preserve $\mathcal{M}$, and hence the linear Zeeman effect does not play any role for a fixed $\mathcal{M}$.

In Fig. 4.1, we report the $\mu - t$ phase space diagram for two values of $g = 0.5, 5.0$. In the figure, we differentiate three regions: the Mott regime in white, the vacuum in black and the metal phase in gray.

For large-enough interactions, $G \gg t$, and for a chemical potential higher than a critical value, $\mu > \mu_c(t)$, the system becomes a MI with one fermion
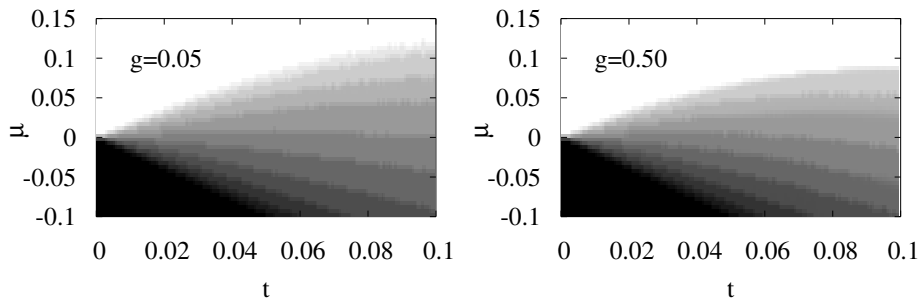
FIGURE 4.1: Phase-space diagram $\mu - t$ for $g = 0.05$ and $g = 0.50$, in absence of an external field. t and μ are in units of G. We distinguish the vacuum (black region), the bottom of the first Mott (white) and the metal phase (gray).

per site. We focus on the magnetic properties of these MI phases in Chapter 5. Note that from an experimental point of view, the MI states with one and two particles per site are the most interesting cases because they are free of three-body losses.

We first discuss the case where no magnetic field is applied ($q = 0$), and thus the four hyperfine components are completely degenerate.

4.2.1 Phase diagram at quarter filling

The magnetic properties of the ground state are determined by the strengths g_0 and g_2. Figure 4.2 depicts the 1D phase diagram for spin-3/2 systems at quarter filling in absence of external fields, which has been discussed in detail by C. Wu in Ref. [107].

The phase diagram contains several phases at incommensurate fillings.

- A gapless spin liquid, with 3 gapless spin-modes, occurs in the repulsive interaction regime $g_{0,2} > 0$ with $g_2 < g_0$, this phase includes the SU(4) line ($g_0 = g_2$) already solved by Sutherland[149].

- A phase characterized by the formation of quartets which is divided in two regions and lies in the regime where attractive interactions dominates. The quartets undergo either superfluidity ($g_0 > g_2$ with $g_2 < 0$ and $g_0 > 0$) or charge density wave (CDW) instabilities ($|g_2| > g_0$ with $g_2 < 0$), the latest is the four-fermion counterpart of Cooper pairing.

- The last phase is characterized by the formation of singlet pairs. The two leading competing orders in this phase are dimerized (spin-Peierls) order ($g_{0,2} > 0$ with $g_2 > g_0$) which exhibits spin-gap, and CDW singlet pairs, the singlet Cooper pairs, which is long range ordered ($g_2 > g_0$ with $g_0 < 0$).
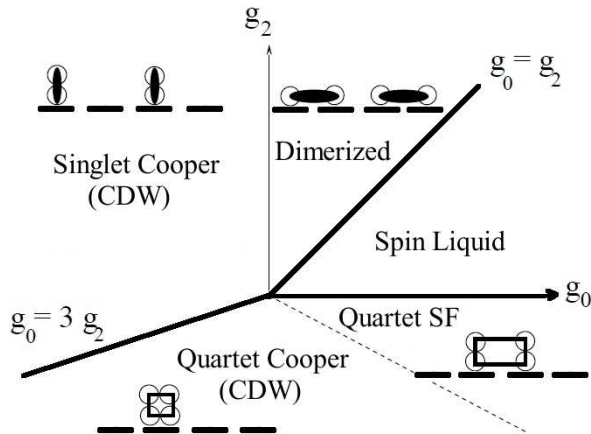
FIGURE 4.2: Spin-3/2 phase diagram at quarter filling in terms of g_0 and g_2. The different phases are shown and the boundaries in solid bold lines are: transitions between spin liquid and either the dimerized phase ($g_0 = g_2$) or the quartet SF ($g_2 = 0, g_0 > 0$) and the boundary between the singlet and the quartet Cooper pairs ($g_0 = 3g_2$). The transition between the quartets are sketched with dashed line and between the singlets with solid single line. See Refs. [106, 107].

Phases in the Mott regime

When the charge gap opens (no holes in the chain) the insulating ground state phases are those in the repulsive interaction regime where $g_0, g_2 > 0$ [106–108], see Fig. 4.2. In terms of the convenient variables of Eq. (4.9), one has that:

- For $-1 < g \leq 0$ the gapless spin-liquid phase is found. The exactly solvable SU(4) point is located in $g = 0$.

- For $0 < g < 1$ one has the dimerized phase which presents a long-range order defined by

$$\lim_{n \to \infty} \langle \hat{D}_i \hat{D}_{i+n} \rangle = f_0, \qquad (4.10)$$

  where f_0 is a finite value and the dimer operators $\hat{D}_i$ are

$$\hat{D}_i = (-1)^i \hat{\mathbf{S}}_i \cdot (\hat{\mathbf{S}}_{i-1} - \hat{\mathbf{S}}_{i+1}), \qquad (4.11)$$

  with $\hat{\mathbf{S}}$ the spin-3/2 operators.

At $g = 0$ the system undergoes a Kosterlitz-Thouless like transition between these two phases [107].

4.2.2   Hard-core regime without external fields

Using the definition of Eq. (B.12) (see Appendix B) and taking into account the fermionic character of the particles, we obtain the effective Hamiltonian

of the system with one particle per site in terms of two-sites spin-manifold projectors [110]

$$\hat{H}_{eff} = \sum_{<i,j>} \left[-\frac{4t^2}{g_0}\hat{P}_{ij}(0) - \frac{4t^2}{g_2}\hat{P}_{ij}(2) \right]. \tag{4.12}$$

It is always convenient to express the Hamiltonian in terms of spin operators. We use the relations of Eq. (4.6) and follow the derivation of Section B.1.2, obtaining:

$$\hat{H}_{eff} = \sum_{<i,j>} \left[-\frac{4t^2}{g_0}\alpha_0(\hat{S}_i\hat{S}_j + \frac{11}{4})(\hat{S}_i\hat{S}_j + \frac{3}{4})(\hat{S}_i\hat{S}_j - \frac{9}{4}) \right.$$
$$\left. -\frac{4t^2}{g_2}\alpha_2(\hat{S}_i\hat{S}_j + \frac{15}{4})(\hat{S}_i\hat{S}_j + \frac{11}{4})(\hat{S}_i\hat{S}_j - \frac{9}{4}) \right], \tag{4.13}$$

where $\alpha_{0,2}$ are given in the appendix. This effective Hamiltonian is of the type of polynomial generic spin exchange Hamiltonians, Eq. (1.17), that one typically finds in the studies of quantum magnetism, as discussed in Section 1.4.

In nature, the values of a_0 and a_2, and thus g_0 and g_2, are typically similar. However, they may be variated by means of micro-wave dressing [95] or optical Feshbach resonances [94]. In the relevant case of $g_0 = g_2$, the effective Hamiltonian reduces to

$$\hat{H}_{eff} = -\frac{4t^2}{g_0} \sum_{\langle ij \rangle} \left[\hat{P}_{ij}(0) + \hat{P}_{ij}(2) \right], \tag{4.14}$$

where

$$\hat{P}_{ij}(0) + \hat{P}_{ij}(2) = \frac{9}{16}(\vec{\hat{S}}_i \cdot \vec{\hat{S}}_j) - \frac{11}{36}(\vec{\hat{S}}_i \cdot \vec{\hat{S}}_j)^2 - \frac{1}{9}(\vec{\hat{S}}_i \cdot \vec{\hat{S}}_j)^3 + \frac{99}{64}, \tag{4.15}$$

showing explicitly bilinear, biquadratic and bicubic terms. This particular spin model also exhibits a uniform SU(4) symmetry and an exact solution has been obtained by means of the Bethe-ansatz method [149].

Up to now, we considered no external magnetic field since any liner Zeeman effect can be gauged out. However, due to spin-changing collisions, which redistribute the populations of the different components while preserving $\mathcal{M}$, the quadratic Zeeman coupling (QZE) characterized by the parameter q becomes crucial in spinor gases and plays a key role in the magnetic properties of the system. The QZE is externally controllable by means of a magnetic field or microwave or optical dressing [92, 93].

4.2.3 Effective model including external fields

Spinor lattice gases offer interesting physics, most relevantly on the field of quantum magnetism, including intriguing phases for higher spins [103, 104,

150]. While for spin-1/2 spin-changing collisions are absent and the quadratic Zeeman effect (QZE) is irrelevant, the latter is crucial for higher spins, as shown in spinor condensates [67, 84, 87, 151]. In spite of its experimental relevance, the QZE is mostly ignored in the analysis of the magnetic properties.

Second-order perturbation theory

The QZE lifts some of the degeneracies of the system, thus a quasi-degenerated perturbation theory should be applied to construct the low-energy effective spin model Hamiltonian. We consider two-site MI states with small but finite tunneling. The virtual hopping induce effective nearest-neighbor spin-exchange interactions [110, 111]. A standard method for this calculation is the Van-Vleck transformation [152]. It performs a perturbation-theory similarity-transformation to the total Hamiltonian and transforms it into a two-block diagonal preserving the eigenvalues. It is depicted in Fig 4.3. One block contains the desired effective Hamiltonian of the system under the given restrictions H_{eff} and the other block contains the virtual states.
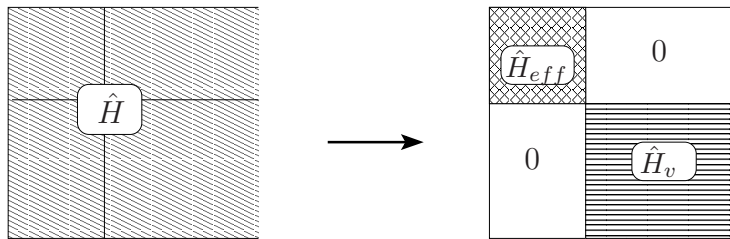

FIGURE 4.3: Removal of the off-diagonal elements of $\hat{H}$. $\hat{H}_{eff}$ represents the effective Hamiltonian while the block $\hat{H}_v$ contains all the virtual states.

Let us start considering the eigenenergies of the unperturbed Hamiltonian Eq. (4.8). First, we solve the eigensystem in the different particle number manifolds.

- One particle (hole) eigenstates and eigenenergies:

Eigenstate	Eigenenergy
$\lvert \varnothing \rangle_1$	0
$\lvert \frac{1}{2} \rangle_1, \quad \lvert -\frac{1}{2} \rangle_1$	$\frac{1}{4}q - \mu$
$\lvert \frac{3}{2} \rangle_1, \quad \lvert -\frac{3}{2} \rangle_1$	$\frac{9}{4}q - \mu$

- Two particles per site with total spin $F = 2$ and projection $m_F \neq 0$:

Eigenstate	Eigenenergy
$\lvert -\frac{1}{2}, -\frac{3}{2}\rangle_1, \quad \lvert -\frac{1}{2}, \frac{3}{2}\rangle_1, \quad \lvert \frac{1}{2}, -\frac{3}{2}\rangle_1, \quad \lvert \frac{1}{2}, \frac{3}{2}\rangle_1$	$\frac{5}{2}q - 2\mu + (1+g)$

Second, we consider the pair-states with projection $m_F = 0$ interacting in both channels $F = 0$ and $F = 2$. It is a special case, since the spin changing collision process plays a significant role exchanging coherently population between the $\pm\frac{1}{2}$ and $\pm\frac{3}{2}$ particles. To do so, we collect all the terms acting on the states $\lvert -\frac{1}{2}, \frac{1}{2}\rangle_1$ and $\lvert -\frac{3}{2}, \frac{3}{2}\rangle_1$ in the following matrix

$$
\begin{array}{cc}
 & \begin{array}{cc} \lvert -\frac{1}{2}, \frac{1}{2}\rangle_1 & \lvert -\frac{3}{2}, \frac{3}{2}\rangle_1 \end{array} \\
\begin{array}{c} \lvert -\frac{1}{2}, \frac{1}{2}\rangle_1 \\ \lvert -\frac{3}{2}, \frac{3}{2}\rangle_1 \end{array} & \left(\begin{array}{cc} q/2 & g \\ g & 9q/2 \end{array} \right).
\end{array}
$$

The resulting states and energies we obtain are:

Eigenstate	Eigenenergy
$\lvert +\rangle_1 = \cos\phi \lvert -\frac{3}{2}, \frac{3}{2}\rangle_1 + \sin\phi \lvert -\frac{1}{2}, \frac{1}{2}\rangle_1$	$\lambda_+ - 2\mu$
$\lvert -\rangle_1 = -\sin\phi \lvert -\frac{3}{2}, \frac{3}{2}\rangle_1 + \cos\phi \lvert -\frac{1}{2}, \frac{1}{2}\rangle_1$	$\lambda_- - 2\mu$

where

$$\tan\phi = \frac{2q + \sqrt{4q^2 + g^2}}{g}, \tag{4.16}$$

$$\lambda_\pm = 1 + \frac{5}{2}q \pm \sqrt{4q^2 + g^2}. \tag{4.17}$$

The next step is to use Van-Vleck perturbation theory to obtain the matrix elements of the desired effective Hamiltonian. The second-order term of the expansion is given by

$$\langle n \lvert \hat{H}^{(2)} \rvert n' \rangle = \frac{1}{2} \sum_\nu \langle n \lvert \hat{H}_t \rvert \nu \rangle \langle \nu \lvert \hat{H}_t \rvert n' \rangle \left[\frac{1}{E_n - E_\nu} + \frac{1}{E_{n'} - E_\nu} \right], \tag{4.18}$$

where $\lvert n \rangle$ and $\lvert n' \rangle$ are two-sites states with exactly one particle per site and $\lvert \nu \rangle$ are the two-sites intermediate virtual states with two particles on a single site and an empty site. For the construction of the $\hat{H}_{eff}$ up to second order we use that

$$\langle n \lvert \hat{H}_{eff} \rvert n' \rangle = \hat{H}^{(0)}_{nn'} \delta_{nn'} + \underbrace{H^{(2)}_{nn'} \delta_{nn'}}_{\text{diagonal}} + \underbrace{H^{(2)}_{nn'} (1 - \delta_{nn'})}_{\text{off-diagonal}}. \tag{4.19}$$

A couple of examples are sketched in Fig. 4.4 and Fig. 4.5. The first depicts the calculation of the simplest diagonal terms while the second shows the intricate calculation of those terms related with the spin changing collision interaction. Following similar procedures and taking into account all the possible paths that link the initial state with the target, for each matrix element, we obtain the two-sites effective Hamiltonian with superexchange

$$
\begin{aligned}
\hat{H}_{eff}^{1,2} = & \sum_m qm^2 \left(\hat{n}_{m,1} + \hat{n}_{m,2} \right) \\
& + c_2 \sum_{|m| \neq |m'|} \left(\hat{n}_{m,1} \hat{n}_{m',2} - \hat{\psi}_{m,1}^\dagger \hat{\psi}_{m',2}^\dagger \hat{\psi}_{m,2} \hat{\psi}_{m',1} \right) \\
& + \sum_{|m|=1/2}^{3/2} c_{|m|} \left(\hat{n}_{m,1} \hat{n}_{-m,2} - \hat{\psi}_{m,1}^\dagger \hat{\psi}_{-m,2}^\dagger \hat{\psi}_{m,2} \hat{\psi}_{-m,1} \right) \\
& + c_{sc} \left\{ \left[\psi_{-\frac{1}{2},1}^\dagger \psi_{\frac{1}{2},2}^\dagger - \psi_{\frac{1}{2},1}^\dagger \psi_{-\frac{1}{2},2}^\dagger \right] \left[\psi_{\frac{3}{2},1} \psi_{-\frac{3}{2},2} - \psi_{-\frac{3}{2},1} \psi_{\frac{3}{2},2} \right] + h.c \right\},
\end{aligned}
\tag{4.20}
$$

where the coefficients are given by

$$
\begin{aligned}
c_2 &= -\frac{2t^2}{1+g}, \\
c_{1/2} &= 2t^2 \left(\frac{\sin^2 \phi}{\frac{1}{2}q - \lambda_+} + \frac{\cos^2 \phi}{\frac{1}{2}q - \lambda_-} \right), \\
c_{3/2} &= 2t^2 \left(\frac{\cos^2 \phi}{\frac{9}{2}q - \lambda_+} + \frac{\sin^2 \phi}{\frac{9}{2}q - \lambda_-} \right), \\
c_{sc} &= 2t^2 \sin\phi \cos\phi \left[\frac{\frac{5}{2}q - \lambda_+}{\left(\frac{9}{2}q - \lambda_+ \right) \left(\frac{1}{2}q - \lambda_+ \right)} \right. \\
& \qquad\qquad\qquad \left. - \frac{\frac{5}{2}q - \lambda_-}{\left(\frac{9}{2}q - \lambda_- \right) \left(\frac{1}{2}q - \lambda_- \right)} \right].
\end{aligned}
\tag{4.21}
$$

The coefficient c_2 characterizes the spin preserving collisions with total spin projection $m_F = 2$. This is the super-exchange interaction between two neighboring particles with m and m' such that $|m| \neq |m'|$. The strength $c_{|m|}$ characterizes the interaction when the two particles have zero total spin projection $m_F = 0$ with local magnetization m and $-m$ but excluding the spin changing collisions which are given by c_{sc}. The latest interaction connects the two spin manifolds $\pm\frac{1}{2}$ and $\pm\frac{3}{2}$ via a simultaneous hopping and spin changing process.

The different coefficients diverge for a critical value $q_{div} = \pm(g^2 - 1/4)$. This is eventually reached when the energy of at least one virtual state coincides with the energy of a real state. Under this conditions, the Mott becomes
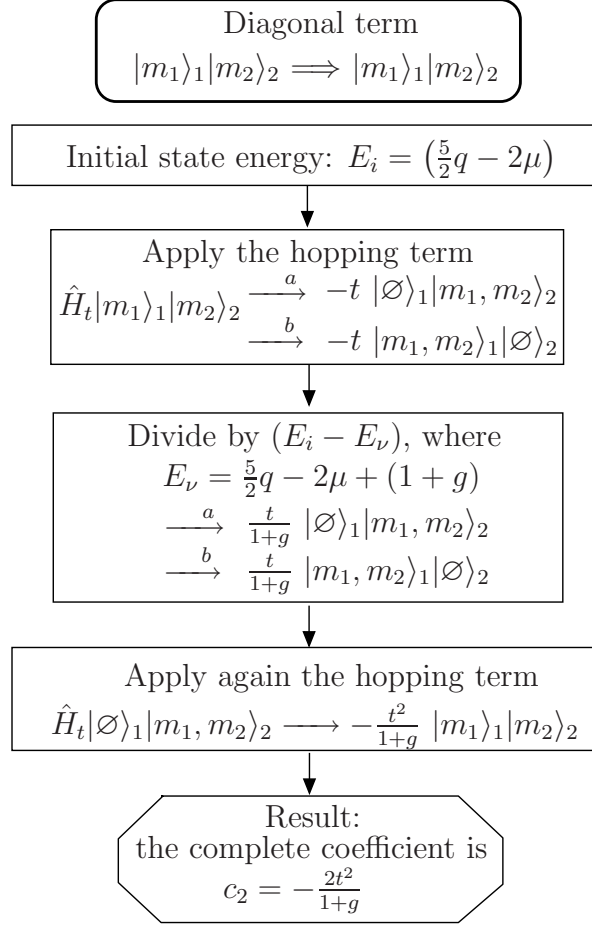
Diagonal term
$$|m_1\rangle_1 |m_2\rangle_2 \implies |m_1\rangle_1 |m_2\rangle_2$$

Initial state energy: $E_i = \left(\frac{5}{2}q - 2\mu\right)$

Apply the hopping term
$$\hat{H}_t |m_1\rangle_1 |m_2\rangle_2 \xrightarrow{a} -t\, |\varnothing\rangle_1 |m_1, m_2\rangle_2$$
$$\xrightarrow{b} -t\, |m_1, m_2\rangle_1 |\varnothing\rangle_2$$

Divide by $(E_i - E_\nu)$, where
$$E_\nu = \frac{5}{2}q - 2\mu + (1 + g)$$
$$\xrightarrow{a} \frac{t}{1+g}\, |\varnothing\rangle_1 |m_1, m_2\rangle_2$$
$$\xrightarrow{b} \frac{t}{1+g}\, |m_1, m_2\rangle_1 |\varnothing\rangle_2$$

Apply again the hopping term
$$\hat{H}_t |\varnothing\rangle_1 |m_1, m_2\rangle_2 \longrightarrow -\frac{t^2}{1+g}\, |m_1\rangle_1 |m_2\rangle_2$$

Result:
the complete coefficient is
$$c_2 = -\frac{2t^2}{1+g}$$

FIGURE 4.4: Scheme to obtain the diagonal coefficient c_2 of $\hat{H}_{eff}$ up to second order in perturbation theory.

unstable and the charge modes cannot be further neglected. Nevertheless, this case is out of the scope of this work. Hence, we consider q small enough that we are save to use this effective Hamiltonian.

Note that $\hat{H}_{eff}$ conserves the total magnetization of the system $\mathcal{M} = 0$ and furthermore the individual components, $(n_{3/2} - n_{-3/2}) = 0$ and $(n_{1/2} - n_{-1/2}) = 0$, recovering the large symmetry of the system in absence of the magnetic field.

Finally, let us express the effective Hamiltonian in terms of the spin operators. As it is expected, we obtain the generalized Heisenberg Hamiltonian, but with two more terms related exclusively to the two spin manifolds. The Hamiltonian reads as follows

$$\hat{H} = \sum_{<ij>} \left[\sum_{k=1}^{3} \gamma_k (\vec{S}_i \cdot \vec{S}_j)^k + \gamma_0 \hat{I}_{i,j} + \gamma_4 \hat{P}_{i,j}^{1/2} + \gamma_5 \hat{P}_{i,j}^{3/2} \right], \tag{4.22}$$

the projectors are defined by

$$\hat{P}_{ij}^m = -2\hat{S}_i^m \hat{S}_j^m + \frac{1}{2}\hat{I},$$ (4.23)

where the spin operators act only in the reduced manifold $m = 1/2$ or $m = 3/2$. The coefficients introduced above are

$$\gamma_0 = -\frac{33t^2\left[(1+g)^2(3+g(2g-5))-48q^2\right]}{16(1+g)\left[(g^2-1)^2-16q^2\right]},$$

$$\gamma_1 = \frac{t^2\left[(g-1)(g+1)^2(27+4g)+432q^2\right]}{12(1+g)\left[(g^2-1)^2-16q^2\right]},$$

$$\gamma_2 = \frac{t^2\left[(g-1)(g+1)^2(-11+6g)-176q^2\right]}{9(1+g)\left[(g^2-1)^2-16q^2\right]},$$ (4.24)

$$\gamma_3 = -\frac{4t^2\left[(g-1)(g+1)^2+16q^2\right]}{9(1+g)\left[(g^2-1)^2-16q^2\right]},$$

$$\gamma_4 = \frac{8t^2gq\left[g+g^2+4q\right]}{(1+g)\left[(g^2-1)^2-16q^2\right]}, \quad \text{and}$$ (4.25)

$$\gamma_5 = -\frac{8t^2gq\left[g+g^2-4q\right]}{(1+g)\left[(g^2-1)^2-16q^2\right]}.$$

In the limiting cases $(q \to 0)$ and $(q \to 0, g \to 0)$, we recover the two-sites effective Hamiltonians of the Eqs. (4.12) and (4.14) [110, 111].

4.3 Spin-1 bosons in optical lattices

4.3.1 Hard-core Hamiltonian without external fields

Let us consider now spin-1 bosons constrained to the lowest Bloch band. Two colliding particles should share the orbital-wavefunctions and therefore each of them has a symmetric spin-wavefunction. This restricts the calculation to the only two possible scattering channels $F = 0$ and $F = 2$, with respective interaction strength g_0 and g_2.

The most general Hamiltonian that describes a balance mixture of spin-1 bosons in optical lattices in the single-band regime [68] is given by

$$\hat{H} = -t\sum_{m,i}[\hat{\psi}_{m,i}^\dagger \hat{\psi}_{m,i+1} + h.c.] + \hat{H}_I,$$ (4.26)

with

$$\hat{H}_I = -\mu \sum_{m,i} \hat{n}_{m,i} + q \sum_{m,j} m^2 \hat{n}_{m,j}$$
$$+ \sum_i \left\{ \frac{g_0 + 2g_2}{6} \hat{\psi}_0^\dagger \hat{\psi}_0^\dagger \hat{\psi}_0 \hat{\psi}_0 + \frac{g_2}{2} \left(\hat{\psi}_1^\dagger \hat{\psi}_1^\dagger \hat{\psi}_1 \hat{\psi}_1 + \hat{\psi}_{-1}^\dagger \hat{\psi}_{-1}^\dagger \hat{\psi}_{-1} \hat{\psi}_{-1} \right) \right.$$
$$\left. + \frac{2g_0 + g_2}{3} \hat{\psi}_1^\dagger \hat{\psi}_{-1}^\dagger \hat{\psi}_{-1} \hat{\psi}_1 + g_2 \left(\hat{\psi}_0^\dagger \hat{\psi}_{-1}^\dagger \hat{\psi}_{-1} \hat{\psi}_0 + \hat{\psi}_0^\dagger \hat{\psi}_1^\dagger \hat{\psi}_1 \hat{\psi}_0 \right) \right. \tag{4.27}$$
$$\left. + \frac{g_2 - g_0}{3} \left(\hat{\psi}_0^\dagger \hat{\psi}_0^\dagger \hat{\psi}_{-1} \hat{\psi}_1 + \hat{\psi}_1^\dagger \hat{\psi}_{-1}^\dagger \hat{\psi}_0 \hat{\psi}_0 \right) \right\}_i .$$

As we already saw, when $t \ll g_0, g_2$ one can treat the hopping as a perturbation. We use again Eq. (B.12), see the details in Appendix B, and calculate the effective Hamiltonian up to one particle per site at $q = 0$

$$\hat{H}_{eff} = \sum_{<i,j>} \left[-\frac{4t^2}{g_0} \hat{P}_{ij}(0) - \frac{4t^2}{g_2} \hat{P}_{ij}(2) \right] = \sum_{<i,j>} \left[-J_0 \hat{P}_{ij}(0) - J_2 \hat{P}_{ij}(2) \right], \tag{4.28}$$

which in terms of spin operators is given by

$$\hat{H}_{eff} = \sum_{<i,j>} \left[-\left(\frac{J_0}{3} + \frac{J_2}{6} \right) \left(\hat{S}_i \hat{S}_j \right)^2 - \frac{J_2}{2} \left(\hat{S}_i \hat{S}_j \right) + \left(\frac{J_0}{3} - \frac{J_2}{3} \right) \hat{I} \right]. \tag{4.29}$$

We have introduced the exchange constants $J_0 = \frac{4t^2}{g_0}$ and $J_2 = \frac{4t^2}{g_2}$ for the channels $F = 0$ and $F = 2$ respectively.

4.3.2 Phase diagram at unit filling

The bilinear-biquadratic Hamiltonian of Eq. (4.29) is the most general isotropic effective Hamiltonian for spin-1 chain restricting to nearest-neighbor interactions and hard-core regime. Up to a constant, this Hamiltonian may be re-written in a widely employed parameterized form:

$$\hat{H}(\theta) = J \sum_{<ij>} \left[\cos\theta (\vec{S}_i \cdot \vec{S}_j) + \sin\theta (\vec{S}_i \cdot \vec{S}_j)^2 \right], \tag{4.30}$$

where $\cos\theta$ ($\sin\theta$) gives the strength of the bilinear (biquadratic) coupling, J is defined as the unity and the angle θ is defined by

$$\tan\theta = \frac{3J_2}{2J_0 + J_2}. \tag{4.31}$$

The properties of the ground state as well as the excitations are determined by θ. The phase diagram is shown in Fig. 4.6.
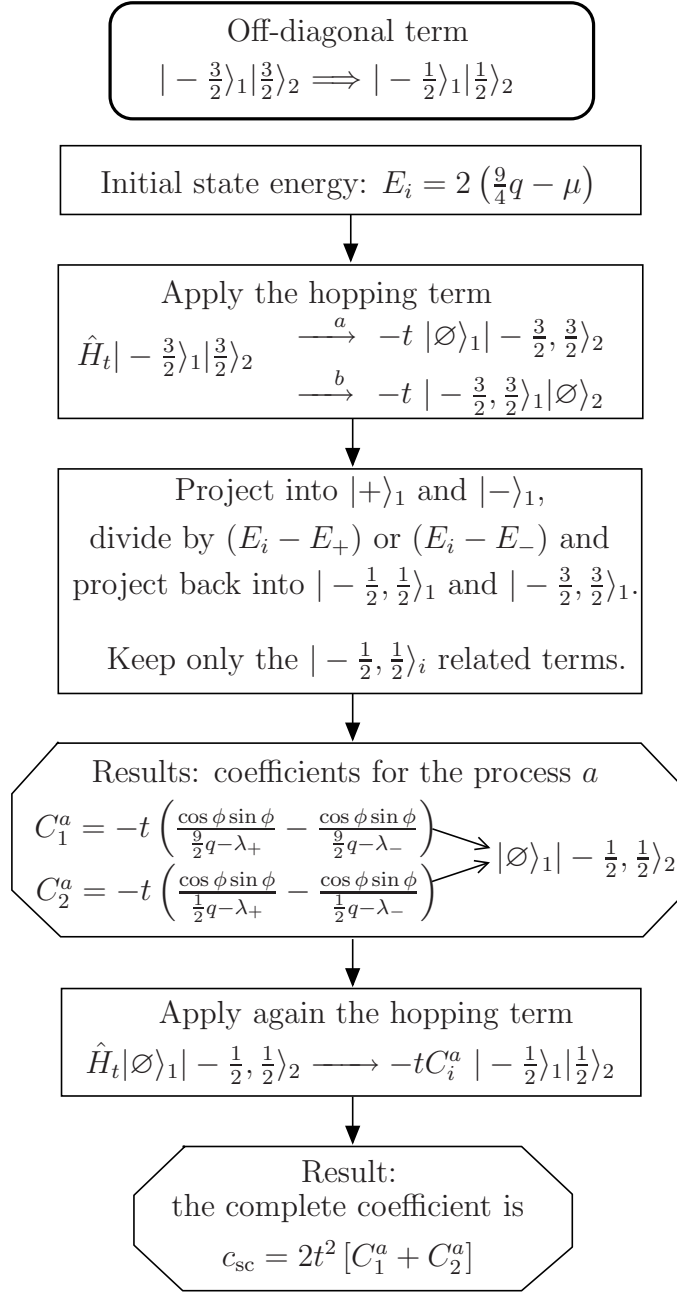
FIGURE 4.5: Scheme to obtain the spin changing collision coefficient, c_{sc}, up to second order in perturbation theory.

In the range $-3\pi/4 < \theta < \pi/2$, the ground state is antiferromagnetic, i.e., has vanishing magnetization ($\vec{M} = \langle \sum_i \vec{S}_i \rangle = 0$). For $\theta \in [-\pi/4, \pi/4]$, the ground state belongs to the Haldane phase, being $\theta = 0$ the Heisenberg point and $\theta = \arctan(1/3)$ the Affleck-Kennedy-Lieb-Tasaki (AKLT) point which is described with an exact valence-bond wavefunction [154]. At the Uimin-
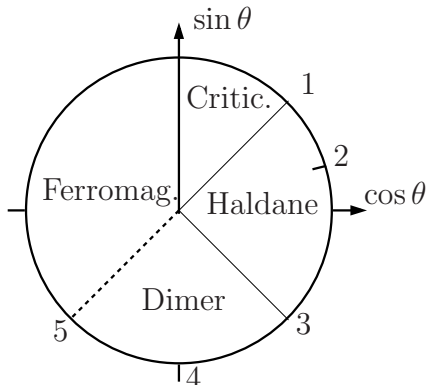
FIGURE 4.6: Spin-1 MI phase-space diagram without external fields. The different ground state phases of Eq. (4.30) are depicted. The solved points are 1: $\theta = \pi/4$, Uimin-Lai-Sutherland (ULS) point, 2: $\tan\theta = 1/3$, Affleck-Kennedy-Lieb-Tasaki (AKLT) point, 3: $\theta = -\pi/4$, Takhtajan-Babujan (TB) point, 4: $\theta = -\pi/2$, Klumper-Barber-Batchelor (KBB) point and 5: $\theta = -3\pi/4$, exactly solvable highly symmetric (SU(3)) point. See Ref. [153].

Lai-Sutherland (ULS) critical point [155], $\theta = \pi/4$ a phase transition occurs into a gapless phase. The Takhtajan-Babujan (TB) critical point [156, 157], $\theta = -\pi/4$, presents a second order phase transition into a dimerized phase which is gapped and has an exactly solvable point at $\theta = -\pi/2$, the Klumper-Barber-Batchelor (KBB) point [158, 159].

4.3.3 Effective model including external fields

We follow the same procedure of Section 4.2.3 to obtain the effective Hamiltonian that describes the physics of spin-1 bosons, in an optical lattice with one particle per site, in presence of an external field.

In order to perform the Van-Vleck transformation, we calculate the eigenenergies of $\hat{H}_I$ of Eq. (4.27) for each particle number manifold.

- One particle (hole) eigenstates and eigenenergies:

Eigenstate	Eigenenergy
$|\varnothing\rangle_1$	0
$|0\rangle_1$	$-\mu$
$|1\rangle_1, \quad |-1\rangle_1$	$q - \mu$

- Two particles per site with total spin $F = 2$ and projection $m_F \neq 0$:

Eigenstate	Eigenenergy
$\lvert -1,0 \rangle_1, \quad \lvert 0,1 \rangle_1$	$q - 2\mu + g_2$
$\lvert -1,-1 \rangle_1, \quad \lvert 1,1 \rangle_1$	$2q - 2\mu + g_2$

- Eigenenergies of the pair-states with projection $m_F = 0$ interacting in both channels $F = 0$ and $F = 2$.

  This is a special case, since spin changing collisions may exchange coherently population between the $m = 0$ and $m = \pm 1$ particles. We collect all the terms in the following matrix

$$
\begin{array}{cc}
& \begin{array}{cc} \lvert -1,-1 \rangle_1 \qquad\qquad & \lvert 0,0 \rangle_1 \end{array} \\
\begin{array}{c} \lvert -1,-1 \rangle_1 \\[1em] \lvert 0,0 \rangle_1 \end{array} &
\begin{pmatrix} 2q + \frac{2g_0 + g_2}{3} & \sqrt{2}\,\frac{g_2 - g_0}{3} \\[1em] \sqrt{2}\,\frac{g_2 - g_0}{3} & \frac{g_0 + 2g_2}{3} \end{pmatrix}
\end{array}.
$$

  After the diagonalization, the resulting states and energies we obtain are:

Eigenstate	Eigenenergy
$\lvert + \rangle_1 = \cos\phi \lvert -1,1 \rangle_1 + \sin\phi \lvert 0,0 \rangle_1$	$\lambda_+ - 2\mu$
$\lvert - \rangle_1 = -\sin\phi \lvert -1,1 \rangle_1 + \cos\phi \lvert 0,0 \rangle_1$	$\lambda_- - 2\mu$

  where

$$
\begin{aligned}
A &= \frac{g_2 + 2g_0}{3}, \\
B &= \frac{g_2 - g_0}{3}, \\
\lambda_\pm &= A + \frac{B}{2} + q \pm \frac{1}{2}\sqrt{9B^2 - 4Bq + 4q^2}, \\
\tan\phi &= \frac{\lambda_+ - A - 2q}{\sqrt{2}B}.
\end{aligned}
\tag{4.32}
$$

The next step is to use the Van-Vleck perturbation theory to obtain the two-sites effective Hamiltonian with superexchange. After the procedure we retrieve

$$\hat{H}_{eff}^{1,2} = \sum_m qm^2 \left(\hat{n}_{m,1} + \hat{n}_{m,2}\right) + \sum_{m=-1}^{1} c_{|m|} \hat{n}_{m,1} \hat{n}_{-m,2}$$
$$+ c_2 \left(\sum_{|m| \neq |m'|} \hat{n}_{m,1} \hat{n}_{m',2} + 2 \sum_{|m| \neq 0} \hat{n}_{m,1} \hat{n}_{m,2} \right) \tag{4.33}$$
$$+ c_{sc} \left[\psi_{-1,1}^\dagger \psi_{1,2}^\dagger \psi_{0,1} \psi_{0,2} + \psi_{1,1}^\dagger \psi_{-1,2}^\dagger \psi_{0,1} \psi_{0,2} + h.c \right],$$

where the coefficients are given by

$$
\begin{aligned}
c_2 &= -\frac{2t^2}{g_2}, \\
c_0 &= -4t^2 \left(\frac{\sin^2 \phi}{\lambda_+} + \frac{\cos^2 \phi}{\lambda_-} \right), \\
c_1 &= 2t^2 \left(\frac{\cos^2 \phi}{2q - \lambda_+} + \frac{\sin^2 \phi}{2q - \lambda_-} \right), \\
c_{sc} &= \sqrt{2} t^2 \sin \phi \cos \phi \left[\frac{1}{2q - \lambda_+} - \frac{1}{2q - \lambda_-} - \frac{1}{\lambda_+} + \frac{1}{\lambda_-} \right].
\end{aligned}
\tag{4.34}
$$

The coefficient c_2 characterizes the spin preserving collisions with total spin projection $m_F = 2$, this is the super-exchange interaction between two neighboring particles. The strength $c_{|m|}$ characterizes the interaction when the two particles have zero total spin projection $m_F = 0$ but excluding the spin changing processes. The interaction given by c_{sc} connects the two spin manifolds 0 and ± 1 via a simultaneous hopping and spin changing collision.

Now, we write the effective Hamiltonian in terms of the spin-1 operators. Again, up to a constant, we obtain the generalized isotropic Heisenberg Hamiltonian and in addition, we retrieve two terms in the way that

$$
\hat{H} = q \sum_i \left(S_i^z \right)^2 + \sum_{<ij>} \left[a_1 (\vec{S}_i \cdot \vec{S}_j) + a_2 (\vec{S}_i \cdot \vec{S}_j)^2 \right.
$$
$$
\left. + a_3 (S_i^x \cdot S_j^x + S_i^y \cdot S_j^y)^2 + a_4 (S_i^z \cdot S_i^z)^2 \right],
\tag{4.35}
$$

where the coefficients are given by

$$a_1 = -\frac{2t^2}{g_2},$$

$$a_2 = 2t^2\left[-\frac{1}{g_2} + \frac{g_2 - g_0}{-3g_0g_2 + 4g_0q + 2g_2q} + \frac{g_0 - g_2}{3g_0g_2 + 2g_0q + 4g_2q}\right],$$

$$a_3 = -t^2\frac{4q(g_0 - g_2)\left[3g_2(g_0 - g_2) + 4q(g_0 + 2g_2)\right]}{g_2\left[3g_0g_2 + 2g_0q + 4g_2q\right]\left[3g_0g_2 - 2q(2g_0 + g_2)\right]}, \qquad (4.36)$$

$$a_4 = t^2\frac{4q(g_0 - g_2)\left[3g_2(g_0 - g_2) - 4q(g_0 + 2g_2)\right]}{g_2\left[3g_0g_2 + 2g_0q + 4g_2q\right]\left[3g_0g_2 - 2q(2g_0 + g_2)\right]}.$$

Since the parameter q fulfills the condition that $q \sim t^2$ for the magnetic properties we are interested in, the above coefficients reduce to

$$a_1 = -\frac{2t^2}{g_2},$$

$$a_2 = -\frac{4t^2}{3g_0} - \frac{2t^2}{3g_2} + \mathcal{O}[t]^3, \qquad (4.37)$$

$$a_3 = \mathcal{O}[t]^4,$$

$$a_4 = \mathcal{O}[t]^4,$$

which are equal to those we obtain at zero magnetic field previously in the Eq. (4.29). With this simplification, and rewriting the expression in a parameterized way, the effective Hamiltonian is given by

$$\widehat{H} = -J\left[\sum_{\langle ij\rangle}\cos\theta\vec{S}_i\cdot\vec{S}_j + \sin\theta\sum_{\langle ij\rangle}\left(\vec{S}_i\cdot\vec{S}_j\right)^2\right] - DJ\sum_i\left(S_i^z\right)^2, \qquad (4.38)$$

where $D = -q/J$ and the standard parameterization of the exchange constants used above is

$$a_1 = -J\cos(\theta), \quad a_2 = -J\sin(\theta), \qquad (4.39)$$

where J and θ are defined by

$$J \equiv \sqrt{a_1^2 + a_2^2} = 2t^2\frac{\sqrt{10g_0^2 + 4g_0g_2 + 4g_2^2}}{3g_0g_2} > 0, \qquad (4.40)$$

$$\arctan(\theta) \equiv \arctan(a_2/a_1) = \frac{-(g_0 + 2g_2)}{-3g_0}, \qquad (4.41)$$

usually J is taken as the unity $J \equiv 1$. The angle θ takes values in the interval $[-\pi/2, -\pi + \arctan(1/3)]$ as the ratio g_0/g_2 varies from 0 to $+\infty$. This limits the possible phases which can be studied (recall Fig. 4.6). More elaborated ideas (involving arranges of electric and magnetic fields to vary at will the coupling constants) may allow for exploring all gapped phases around the circle [153].

4.4 Summary

In this chapter we have discussed the effective Hamiltonians in the Mott insulator regime with one particle per site (hard-core limit), in absence of an external magnetic field for spin-3/2 fermionic and spin-1 bosonic systems. We have reviewed the phase diagrams at zero field for these different systems.

The quadratic Zeeman effect plays a crucial role in the magnetic properties of ultra-cold spinor systems. Therefore, we have introduced the external field and analyzed in detail the calculation of the effective hard-core Hamiltonian with super-exchange interactions for both spin-3/2 fermions and spin-1 bosons. This will allow us the study of the magnetic phases one can obtain inside the Mott regime and of course the quantum phase transitions between the involved phases. In Chapter 5, we study spin-3/2 systems, while Chapter 6 is devoted to spin-1 systems.

Spin-3/2 Mott phases in the presence of QZE

We study the influence of the quadratic Zeeman effect on the Mott-insulator phases of hard-core 1D spin-3/2 fermions. We show that, contrary to spinor bosons, the quadratic Zeeman coupling preserves an $SU(2) \otimes SU(2)$ symmetry, leading for large-enough coupling to an isotropic pseudo-spin-1/2 Heisenberg antiferromagnetic phase. Decreasing the quadratic field this phase undergoes, depending on the scattering lengths, through either a Kosterlitz-Thouless transition into a gapped dimerized phase or a commensurate-incommensurate transition into a gapless spin liquid. This rich phase diagram can be observed experimentally in four-component fermions in optical lattices under similar entropy constraints to those required for Néel order in spin-1/2 gases.

5.1   Motivation

The high spin physics with cold atoms contains novel features which do not appear in solid state systems where the quantum fluctuations are typically weak. Therefore, these high spin systems are treated classically. In contrast, such behavior does not happen in high spin systems with cold atoms where high (hidden) symmetries and strong quantum fluctuations are possible. Such a high symmetry without fine tuning is rare in condensed matter and thus it is worthwhile for further exploration with cold atomic systems. Moreover, relatively few works have been done for high spin fermions, although such systems indeed have interesting properties.

Spin-3/2 magnetic systems are characterized by strong quantum fluctuations. This is a little bit counter-intuitive because one would expect weak quantum fluctuations due to the high spin. However, because of a hidden high SO(5) symmetry, quantum fluctuations are actually even stronger than those in spin-1 systems. The ground state properties for repulsive spin-3/2 fermions have shown to be very interesting [106, 108]. As we already commented, this system at quarter filling may undergo a Mott transition. Contrary to spin-1/2, the Mott of spin-3/2 presents in one dimension distinct magnetic phases, in absence of an external field, given by a gapless spin liquid or a gapped dimerized phase, depending on the inter-atomic interactions.

In this chapter, our starting point is the effective Hamiltonian (4.20) obtained in the previous chapter. Based on it, we analyze the magnetic phases and phase transitions of the spin-3/2 systems in the Mott regime in the presence of the experimentally relevant quadratic Zeeman effect. Note that in the context of quantum magnetism, this coupling is usually called single ion anisotropy.

5.2 Isotropic Heisenberg antiferromagnet at $|\tilde{q}| \gg \tilde{q}_c$

Let us start analyzing the limiting case when the magnetic field is very strong compared to the other interaction strengths in the problem. In particular the case where $|q|$ is larger (but finite) than a critical value $\tilde{q}_c$ where the transition would be expected. In this limit, the degeneracy among the components is lifted, in such a way, that the system behaves like an effective pseudo-spin-1/2.

The $\pm 1/2$ and $\pm 3/2$ spin manifolds are linked by the spin changing collision super-exchange, given by the coefficient c_{sc}, from the coefficients set of Eq. (4.21). In the limit under consideration, since the two spin manifolds separate from each other, this interaction is very small. Therefore, we perform perturbation theory up to second order in c_{sc} and project the four-components Hamiltonian into a two-component system. The favoring of either manifold depends on the sign of q. For $q < 0$ the $\pm 3/2$ manifold is picked and $\pm 1/2$ otherwise.

We found that the Hamiltonian (4.20) reduces to an isotropic Heisenberg antiferromagnetic (IHAFM) form

$$H_{HAF}^{|m|} = \sum_i \left(J_{|m|} \hat{S}_i^m \cdot \hat{S}_{i+1}^m + \eta_{|m|} \hat{I}_{i,i+1} \right), \qquad (5.1)$$

with

$$J_{|m|} = -2 \left[c_{|m|} - c_{sc}\epsilon \right], \qquad \eta_{|m|} = \left[2m^2 + J_{|m|} \right], \qquad (5.2)$$

and

$$\epsilon \equiv \frac{c_{sc}}{c_{3/2} - c_{1/2} - \left[(\frac{3}{2})^2 \pm (\frac{1}{2})^2 \right]} \ll 1, \qquad (5.3)$$

where + stands for $|m| = 1/2$ manifold and − for $|m| = 3/2$. $\hat{S}^m$ denotes the pseudo-spin-1/2 operators for each manifold. Here, we recover the operators we have obtained before, when we wrote the effective Hamiltonian in terms of the spin operators, see Eq. (4.23). We have found, apart from the generalized isotropic spin exchange Hamiltonian, two projector operators that act only on the different spin manifolds. The explicit definition of the pseudo-spin-1/2

operators is as follows

$$\hat{S}_z^m \equiv (\hat{n}_m - \hat{n}_{-m})/2,$$
$$\hat{S}_+^m \equiv \hat{\psi}_m^\dagger \hat{\psi}_{-m}, \tag{5.4}$$
$$\hat{S}_-^m \equiv \hat{S}_+^\dagger.$$

Since $J_{|m|} > 0$ for all $g_0, g_2, |q| > 0$, the system reduces to an IHAFM for large enough $|q|$. This is true at any order in ϵ due to a hidden SU(2) symmetry (see below). This must be compared to the case of spinor bosons [160], where virtual transitions between manifolds lead for large $|q|$ to an anisotropic Heisenberg Hamiltonian (see in the next chapter Eq. (6.1)), demanding a fine-tuning of the microscopic constants to map the system to an IHAFM.

It has been shown that spin-3/2 fermions present a hidden SO(5) symmetry in the absence of an external field [105]. Interestingly, here we show that, with the field coupling, a high symmetry is still preserved. At any q the system retains a SU(2) $\otimes$ SU(2) symmetry generated by a direct product of two SU(2) spin algebras operating in the $\pm 1/2$ and $\pm 3/2$ manifolds, respectively. The SU(2) generators are

$$\hat{S}_z^\alpha = 1/2 \sum_i (\hat{n}_{\alpha,i} - \hat{n}_{-\alpha,i}),$$
$$\hat{S}_+^\alpha = \sum_i \psi_{\alpha,i}^\dagger \psi_{-\alpha,i}, \tag{5.5}$$
$$\hat{S}_-^\alpha = \hat{S}_+^{\alpha\dagger}$$

with $\alpha = \{1/2, 3/2\}$. The operators belong to the SO(5) symmetry algebra for $q = 0$ and also commute separately with the QZE term. Note that this high SU(2) $\otimes$ SU(2) symmetry is related neither to the hard-core constraint nor to quarter filling, nor to the 1D nature of the problem, being rather a generic feature of spin-3/2 fermions with QZE. This symmetry might be very helpful for future numerical simulations on four-component fermions in magnetic fields. For large $|q|$, the exact SU(2) symmetry in the $\pm 3/2$ and $\pm 1/2$ manifolds results in the above-mentioned isotropy of the pseudo-spin-1/2 Heisenberg antiferromagnet.

The increment of $|q|$ induces phase transitions between the $q = 0$ phases (dimerized phase and spin liquid phase, introduced in Section 4.2) and the IHAFM. Let us now study the phases involved in these two limits and the involved transition.

5.3   Dimerized phase vs IHAFM ($g > 0$)

In the dimerized phase, the symmetry with respect to translation by one site is spontaneously broken. This unusual ground state is characteristic of 1D
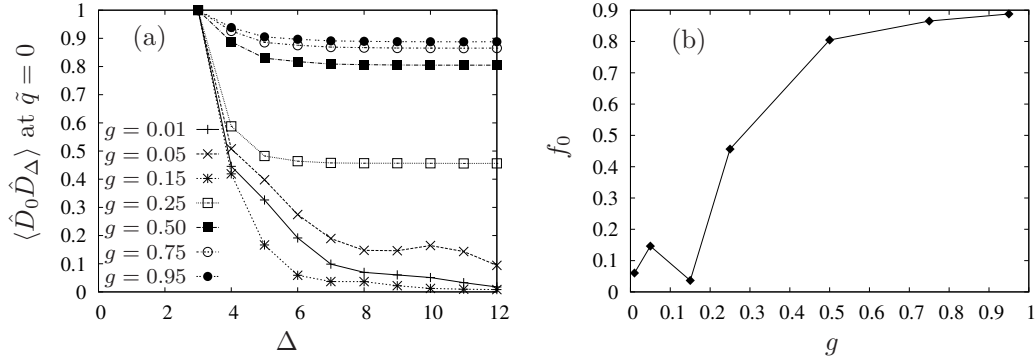
FIGURE 5.1: Dimer phase for several values of g at $q = 0$. (a) Spatial correlation function. (b) f_0 as a function of g.

systems. The possibility of the ground state to be dimerized comes from the fact that a neighboring pair of spins with antiferromagnetic interaction tends to form a spin singlet. In general any spin may be coupled to any other as long as the sign is positive for odd separation and negative for even, for instance. Then, the ground state shows a Peierls ordering structure breaking translational invariance. This ordering in a spin-chain model is studied by the magnetic order parameter D to describe the formation of neighboring sites singlets,

$$D = \frac{1}{L-1} \sum_i (-1)^i \left\langle (\vec{S}_{i-1} \cdot \vec{S}_i) - (\vec{S}_i \cdot \vec{S}_{i+1}) \right\rangle \equiv \frac{1}{L-1} \sum_i \langle \hat{D}_i \rangle, \qquad (5.6)$$

where L is the number of lattice sites. A long-range order in the dimer-dimer correlation functions characterizes the dimerized phase:

$$\lim_{\Delta \to \infty} \langle \hat{D}_i \hat{D}_{i+\Delta} \rangle = f_0. \qquad (5.7)$$

In Fig. 5.1, we show how the long range order becomes stronger as the interaction $g > 0$ increases in absence of QZE. In the panel (a) the dimer-dimer correlation $\langle \hat{D}_0 \hat{D}_\Delta \rangle$ is presented for several values of g while the panel (b) shows the clear rising of f_0 with the increasing of the spin-changing collisions exchange, since g is the measurement of such interaction.

We make use of the MPS ansatz to calculate several ground states with up to 36 sites, open boundary conditions and matrix dimension $\chi = 20$. We perform calculations for several g and $\tilde{q} = 0$ in order to analyze the characteristics of the dimerized phase and $\tilde{q} = -15$ which is considered large enough to study the IHAF, where the $\pm 3/2$ manifold has been chosen to be the ground state. The renormalized QZE parameter $\tilde{q}$ is defined as

$$\tilde{q} = \frac{qG}{t^2}. \qquad (5.8)$$
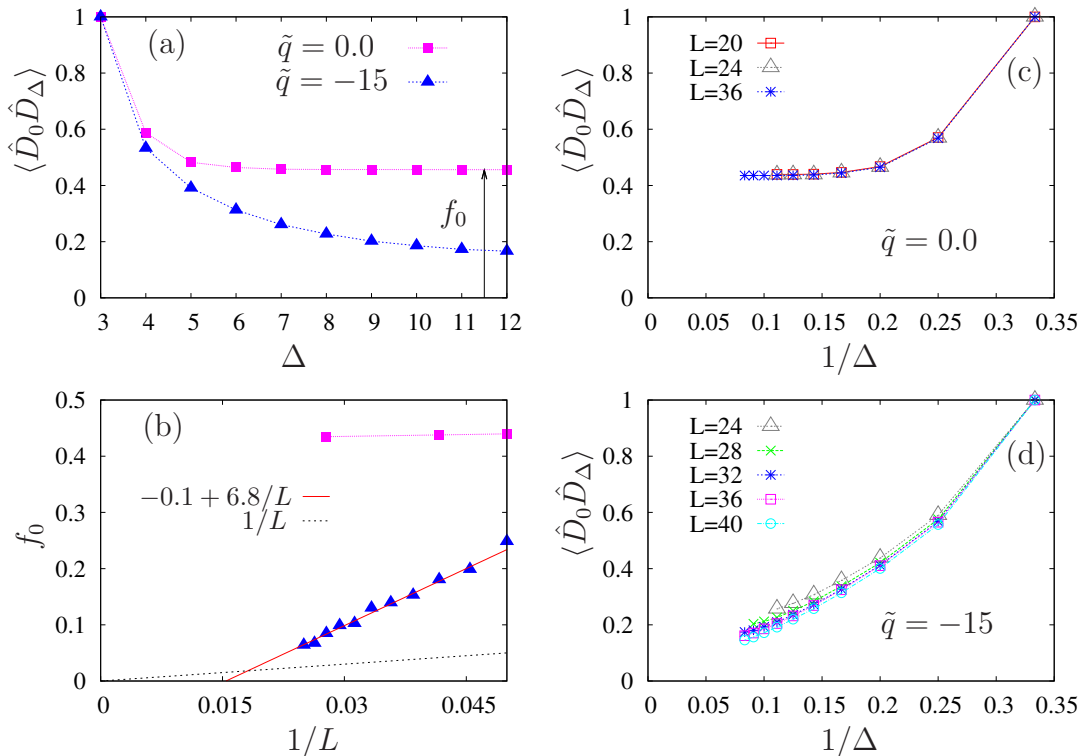
FIGURE 5.2: (a) Dimer-dimer correlations for $\tilde{q} = 0$ and $\tilde{q} = -15$. (b) Finite-size scaling $f_0 \to 0$ for $\tilde{q} = -15$ and f_0 is finite for $\tilde{q} = 0$ implying long-range spin-Peierls ordering. (c) Dimer-dimer correlations for several system sizes for $\tilde{q} = 0$ and (d) for $\tilde{q} = -15$.

Contrary to the dimerized phase, the long range order disappears in the Heisenberg phase. This feature is suggested in Fig. 5.2(a) since the spatial dimer-dimer correlation for $\tilde{q} = -15$ decays faster compared with the $q = 0$ case. To analyze this characteristic long range order, we repeat the calculation for several system sizes in order to perform a finite size scaling, which is shown in the panel (b). We can see how f_0 falls rapidly to lower values of $1/L$ for the IHAFM case (filled triangles) while it goes almost constant for the dimerized case (filled squares). Panels (c) and (d) show the dimer-dimer correlations as a function of $1/\Delta$. The figure shows how the functions tend to a finite value for the case of $q = 0$ in (c) and to zero for the case of $\tilde{q} = -15$ in (d).

Let us continue with the study of the correlations by analyzing the spin-spin correlation function $\langle \vec{S}_0 \vec{S}_\Delta \rangle$ for both phases. As we mentioned already, the dimerized phase is formed by singlets on neighboring sites. Thus, it is expected that the system does not present much correlation between two distant spins as soon as they belong to different and not-neighboring singlets. Indeed, an exponential decay of the spin-spin correlation is retrieved from the calculations, as it is shown in Fig. 5.3(a) with filled squares. The corresponding
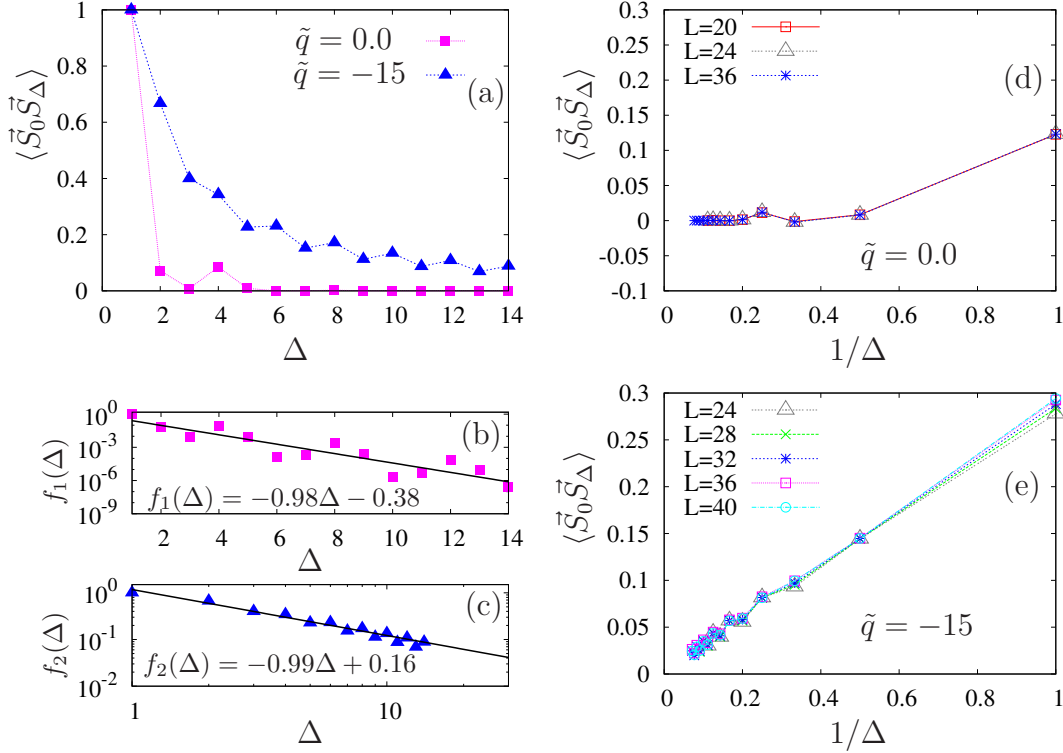
FIGURE 5.3: (a) Spin-spin correlations for $\tilde{q} = 0$ and $\tilde{q} = -15$. (b) Shows the exponential decay of the correlation for $\tilde{q} = 0$ and (c) the algebraic decay for $\tilde{q} > 1$.(d) Spin-spin correlations for several system sizes for $\tilde{q} = 0$ and (e) for $\tilde{q} = -15$.

exponential fitting is presented in panel (b). On the other hand, the IHAFM phase decays algebraically (see the fitting in panel (c)) which suggest the global distribution of the spins along the lattice showing the 1D counterpart of the 3D Néel order. Panels (d) and (e) present the spin-spin correlations as a function of $1/\Delta$ for several system sizes. They show the fast decay in the dimerized phase $q = 0$ and the Δ^{-1} decay expected for a Heisenberg phase.

Finite dimerization in the thermodynamic limit leads to a gap Δ_g (singlet-triplet gap) in the magnetic excitation spectrum[161]. Moreover, the gap vanishes in the IHAFM phase. Numerically, the measurement of the gap is very expensive. We present the calculation for only one interaction strength value, namely $g = 0.25$, to exemplify it. The result is plotted in Fig. 5.4. We have introduced a linear Zeeman field (LZE), hG/t^2, which leads us to a separation of the spin-components. In the figure the horizontal rows of crosses are calculated as follows: first, we fix the QZE, obtain the ground states scanning the linear field and stop when the magnetization gets different from zero. Then, the next value of QZE is used, and we scan again the LZE. The calculation is repeated until a constant value for the LZE is reached. Since the
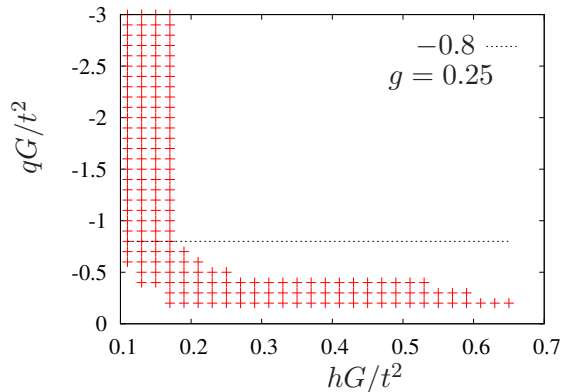
FIGURE 5.4: Gap measurement for $g = 0.25$. The crosses show the region whit zero magnetization, the dashed line shows the place where gap and the critical QZE are defined.

gap is proportional to the linear magnetic field, it is an indirect measurement. At this particular point, we also set the critical QZE like the value when the gap closes, the dimerized phase finishes and the IHAFM starts, i.e. the phase transition occurs. For the example of the figure we retrieve $\Delta_g \sim 0.17$ and $\tilde{q}_c \sim -0.8$ for $g = 0.25$.

5.3.1 Kosterlitz-Thouless phase transition

The previous calculation of the gap gives us a flavor of a phase transition. Now, we are interested to explore this transition, that the QZE brings to the system, which is presumably to be a Kosterlitz-Thouless-like for the case where $g > 0$. For the calculations, we have chosen $q < 0$ and thus the ground state on the manifold of $\pm 3/2$. Nevertheless, similar reasonings apply to $q > 0$ for which the $\pm 1/2$ manifold is favored.

Bosonization shows that the dimerized phase is robust at small $|q|$, which induces a finite chirality τ, defined by

$$\tau = \frac{1}{L}[(N_{3/2} + N_{-3/2}) - (N_{1/2} + N_{-1/2})]. \tag{5.9}$$

We monitor in Fig. 5.5 the chirality as a function of the QZE. τ ranges from 0 at $q = 0$ to 1 in the pure IHAFM phase. This quantity is conserved in absence of the field but it does not at finite q. Although the particle number is conserved in each manifold, the difference between them is not. This fact is reflected in the quasi-saturation behavior for a very small g and the smooth convergence to 1 for larger values. Hence, this is not the observable to follow in order to determine the phase transition.

In spite of this, we scan the chirality for several values of q and g and record the data in a density plot in Fig. 5.6, due to its experimental relevance
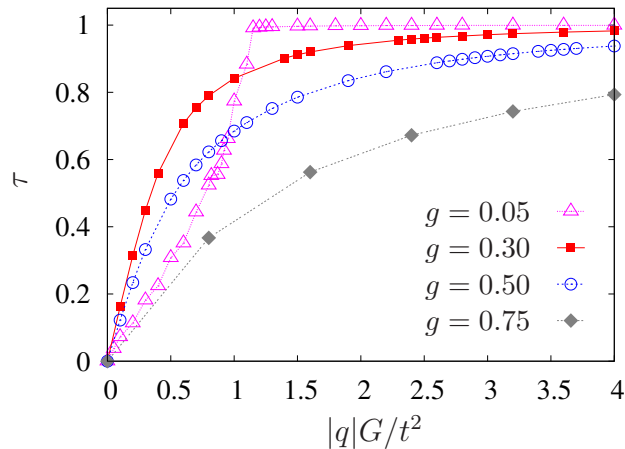
FIGURE 5.5: Chirality τ as a function of $\tilde{q}$ for several values of $g > 0$.

and the fact that τ becomes important in the case of $g < 0$ as we discuss further in Section 5.4. At large $|q|$ bosonization is also not the appropriate technique to study the system. Therefore, one must instead descend from the IHAFM decreasing $|q|$ performing a strong-coupling study.

5.3.2   Strong-coupling analysis

Following the same spirit of Section 5.2, we start from the effective Hamiltonian Eq. (4.20) and perform a perturbation theory to obtain the more relevant spin-exchange interactions of the system when q is large enough. We want to allow next-nearest-neighbor exchanges in the system, to do so, we consider $\hat{H}_q$ as the unperturbed Hamiltonian and the set $\{\hat{H}_{c_2}, \hat{H}_{c_{|m|}}, \hat{H}_{c_{sc}}\}$ as the perturbative term. We also need to go up to fourth order in perturbation theory for our purpose. At the end, we found indeed a Hamiltonian of the form

$$\hat{H}_{J_1 - J_2} = J \sum_i \vec{S}_i \cdot \vec{S}_{i+1} + J_2 \sum_i \vec{S}_i \cdot \vec{S}_{i+2}. \tag{5.10}$$

Where, the spin-changing processes lead to an antiferromagnetic frustrating next-nearest neighbor exchange J_2 ($\sim \tilde{q}^{-2}$) between pseudo-spins-1/2, resembling a frustrated spin-1/2 $J_1 - J_2$ AFM chain, which presents a phase transition at $J_2/J_1 \simeq 0.25$ [162]. Hence, a transition can be anticipated between the IHAFM and the dimerized phase since when lowering $\tilde{q}$ and increasing g the ratio J_2/J increases. Figure 5.6 shows the curve $J_2/J = 0.25$ (solid line) obtained from strong-coupling perturbation theory, which is in good agreement with the Lanczos results discussed below. However, the strong-coupling analysis is not a reliable proof of the existence of a phase transition and numerical calculations must be performed to confirm this scenario.
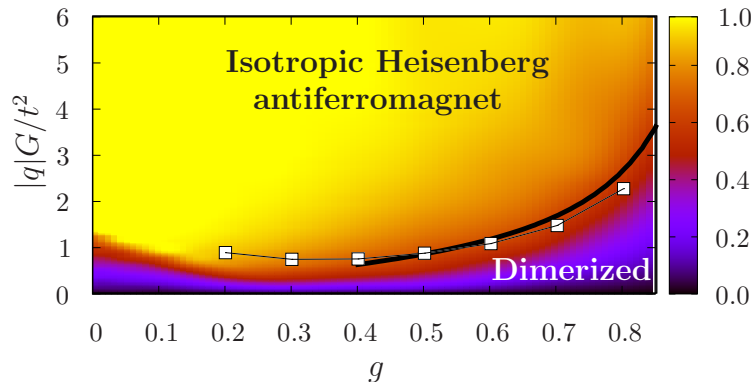
FIGURE 5.6: Phase transition from dimerized to IHAFM for $g > 0$. We depict the chirality τ as a function of q and g (density plot), the $J_2/J = 0.25$ curve resulting from the strong coupling analysis (solid line) and the singlet-triplet crossing in the excitation spectrum (squares).

5.3.3 Level spectroscopy

In a finite chain the two ground states of the dimerized phase (degenerate in the thermodynamic limit) split into a unique ground state and an excited one separated by an energy gap exponentially small in the system size. Thus, for finite chains the lowest excited state in the dimerized phase is unique (for $0 > |\tilde{q}| > |\tilde{q}_{cr}|$). In contrast, the lowest excited state above the Heisenberg ground state $(|\tilde{q}| > |\tilde{q}_{cr}|)$ for a finite-size chain is a degenerate triplet. If the phase transition is of Kosterlitz-Thouless type, as in a frustrated spin-$1/2$ $J_1 - J_2$ AFM chain, a level crossing between the lowest excited singlet and triplet states should occur. Exact Lanczos diagonalization results, for up to 14 sites with periodic boundary conditions and performing finite-size scaling, indeed confirm this crossing. These calculations were performed by A. Argüelles, and hence for more details about this technique we refer to his PhD Thesis [163].

The curve for $\tilde{q}_{cr}$ obtained by Lanczos method is shown in Fig. 5.6 together with the results retrieved by the strong-coupling analysis on top of density plot chirality calculations performed with the MPS. It is very interesting that the extrapolated $\tilde{q}_{cr}$ lies in the region expected from the MPS calculation of τ (the blurred orange region on the Fig. 5.6). This suggests, for $g > 0$, a Kosterlitz-Thouless phase transition with decreasing $|q|$ from the IHAFM into the dimerized phase. For large g, although with non-negligible corrections, $\tilde{q}_{cr}$ follows a $1/L^2$ extrapolation (with L the system size) like in the $J_1 - J_2$ AFM chain [162]. For $g \ll 1$ finite-size effects prevent any reliable extrapolation law.

Figure 5.6 is characterized by a reentrant dimerized phase. This feature is presented in the chirality density plot as well as in the level spectroscopy results. Let us note that decreasing $|q|$, the dimerized phase of the pseudo-

spin-1/2 chain adiabatically connects with the dimerized phase of spin-3/2 fermions, as they share similar properties.

5.4   Spin liquid phase vs IHAFM ($g \leq 0$)

We are interested in the ground state at finite q for every $g \neq 0$. Let us address now to the case where $g \leq 0$. In this case, there is a phase transition between two gapless phases which are the spin liquid and the IHAFM.

5.4.1   Two band model, $g = 0$

At $g = 0$ the system do not have spin-changing collisions, therefore the critical properties as a function of q resemble those of a two-band model [164], where atoms with $m = 3/2$ (1/2) act as fermions at the lowest (second) band, and the QZE difference $2q$ resembles the band gap. The two-band model Hamiltonian has the form

$$H_{2B} = J_{2B} \sum_i^N \left[\sum_{\sigma\sigma'} \sum_{mm'} \left(\hat{\psi}_{i\sigma}^{m\dagger} \, \hat{\psi}_{i\sigma'}^{m'} \, \hat{\psi}_{i+1\sigma'}^{m'\dagger} \, \hat{\psi}_{i+1\sigma}^{m} - \hat{n}_i \hat{n}_{i+1} \right) - q \left(n_i^{(3/2)} - n_i^{(1/2)} \right) \right]$$

(5.11)

where $\hat{\psi}_{i\sigma}^{m\dagger}$ ($\hat{\psi}_{i\sigma}^{m}$) is the creation (annihilation) operator. Each band has two spin states ($\sigma = \uparrow, \downarrow$). With the local constraint that the number of particles is unity at each site, i.e. $n_i = \sum_m \hat{n}_i^{(m)} = 1$. It has been shown that the two bands are completely separated for $q/J_{2B} > \log 2$ [164].

In our case, the exchange strength is twice of the two-band model one, such that $J = 4t^2/G = 2J_{2B}$, therefore $|\tilde{q}_{cr}| \equiv 2 \ln 2 \simeq 1.38$. For $|\tilde{q}| < |\tilde{q}_{cr}|$, the magnetic order is suppressed due to "orbital" effects and the system has three massless spinons. On the contrary, for $|\tilde{q}| > |\tilde{q}_{cr}|$ the orbital degeneracy is lifted and the manifolds $\pm 1/2$ and $\pm 3/2$ completely decouple in the ground state. When this occurs, τ saturates to 1 and the system reduces to the already mentioned pseudo-spin-1/2 IHAFM. In the later phase, the magnetic order also becomes more favorable due to the enhanced antiferromagnetic spin correlations $\langle \hat{S}_z^i \cdot \hat{S}_z^j \rangle \propto |j - i|^\gamma$ with expected exponent $\gamma = -1$. Hence, at $\tilde{q}_{cr}$ there is a phase transition from a gapless spin liquid into a gapless AFM pseudo-spin-1/2 chain with a clear jump in the critical exponent γ [164].

We have determined at $g = 0$ the critical value $\tilde{q}_{cr}^{MPS} \simeq -1.35$, in good agreement with the expected value. Our results are consistent with $1 - \tau \sim \sqrt{|\tilde{q}_{cr}| - |\tilde{q}|}$ when approaching the phase transition for growing $|q|$. Hence, at $g = 0$ and $\tilde{q}_{cr}$ there is a commensurate-incommensurate phase transition [165] between the two gapless phases. This particular point is depicted in the Fig. 5.8 by a black triangle. Moreover, $g = 0$ and $\tilde{q}_{cr}$ is a multi-critical point

for three phases: spin liquid, pseudo-spin-1/2 IHAFM, and the dimerized phase.
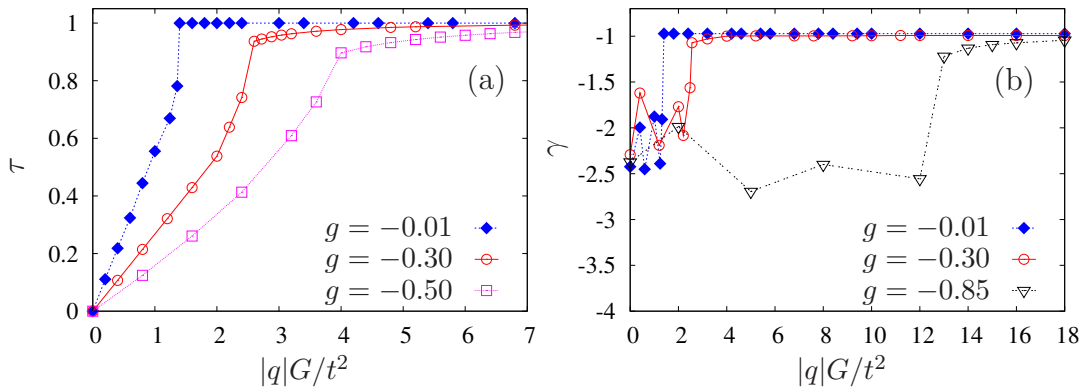
FIGURE 5.7: Chirality τ and critical exponent γ as a function of $\tilde{q}$ for several values of $g < 0$.

5.4.2 Commensurate-Incommensurate phase transition

The region $g < 0$ smoothly connects with $g = 0$ since perturbations from $g = 0$ into $g < 0$ are (marginally) irrelevant in the renormalization group sense [106] and the symmetry dynamically enlarges to SU(4). One could hence expect that the $g < 0$ region behaves similarly to the $g = 0$ case for growing $|q|$. There is, however, an important distinction, since for $g \neq 0$ τ is not a good quantum number, never saturating for finite q. A plausible scenario for $g \leq 0$ is that the QZE induces a commensurate-incommensurate phase transition, so that chirality-non-conserving processes remain irrelevant all the way and do not modify the nature of the transition that takes place at $g = 0$.

Numerical simulations must be performed to confirm this scenario. The phase transition cannot be identified by studying τ alone, and in addition we study the critical exponent γ of the spin-spin correlations. A jump in γ, if present, will confirm the commensurate-incommensurate nature of the phase transition. γ is relevant only for phases with algebraically decaying correlations, which excludes the dimerized phase.

Figure 5.7 shows the results for τ and γ obtained with the MPS method. In the figure, we see that contrary to the case of large $g > 0$ where τ converges smoothly to 1, for the case of $g < 0$ we observe a quasi-saturation of τ (Fig. 5.7(a)) and an abrupt jump of γ to -1 (Fig. 5.7(b)). At small $g < 0$, we indeed obtain that the transition retains the main features of that at $g = 0$, since the saturations are sharper.

Let us remark that for $g < 0$, $\langle \hat{S}_z^i \cdot \hat{S}_z^j \rangle$ oscillates with a period of 4 sites. Instead, one must study the decay of the bulk correlation envelope function [166].
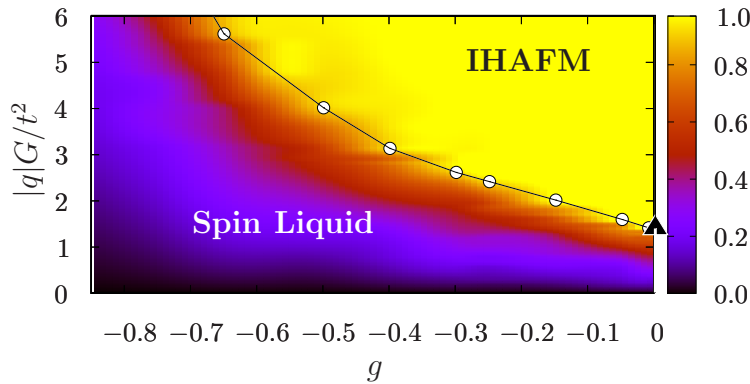
FIGURE 5.8: Phase transition from spin liquid to IHAFM for $g < 0$. We depict the chirality τ as a function of q and g (density plot), the jump of the critical exponent γ to -1 (circles) and the critical $\tilde{q}_{cr}$ expected from the two-band theory (triangle).

It means that one has first to calculate the bulk spin-spin correlation function given by

$$\langle \hat{S}_i^z \hat{S}_{i+j}^z \rangle_{bulk} \equiv \frac{1}{4} \sum_{k=0}^{3} \langle \hat{S}_{i+k}^z \hat{S}_{i+k+j}^z \rangle, \qquad (5.12)$$

and then take the envelope (each 4 sites). Finally, γ is obtained from the algebraic decay of this envelope function.

5.5   Spin-3/2 Mott insulator phase diagram

The complete Mott insulator phase diagram of spin-3/2 fermions in the presence of the quadratic Zeeman coupling is presented in Fig. 5.9. We have shown that at large QZE the system becomes a pseudo-spin-1/2 isotropic Heisenberg antiferromagnet (IHAF). Depending on the scattering lengths, the IHAF undergoes for decreasing QZE either a Kosterlitz-Thouless phase transition into a gapped dimerized spin-3/2 or a commensurate-incommensurate phase transition into a spin-liquid phase with three gapless spin modes.

5.6   Experimental feasibility

Finally, let us comment about the experimental requests needed for the observation of the phase diagram here we present. The observation of the dimerized phase requires a temperature (T) scale with an upper bound provided by the spin gap, which is maximal at $g \sim 1$ and $q = 0$, being from our results $\Delta \simeq t^2/g_0$. For gapless phases (and phase transition lines) the T scale, below which 1D spin correlations are relevant, is given by the peak in the T
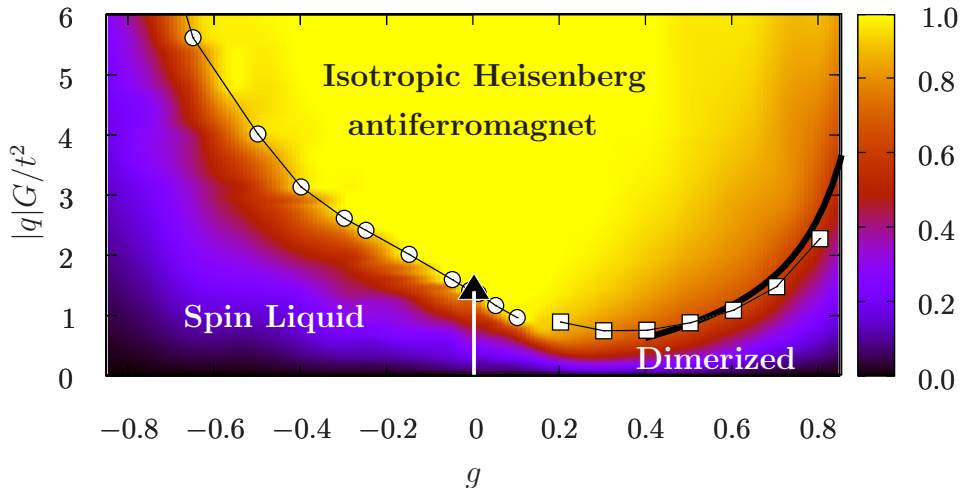
FIGURE 5.9: Phase diagram for spin-3/2 fermions as a function of the relative coupling constant g and the QZE q. We depict the chirality τ (density plot), the singlet-triplet crossing in the excitation spectrum (squares), the jump of the exponent γ to -1 (circles), the critical q_{cr} expected from two-band theory (triangle), and the $J_2/J = 0.25$ line resulting from a strong-coupling analysis (black curve). See text.

dependence of the magnetic susceptibility. Inferring the corresponding T for IHAFM [167] and spin-liquid phases [155], and using the T dependence of the entropy per site in these phases [168], we estimate the entropy per particle as $s \sim 0.4k_B$ and $0.5k_B$ for revealing the IHAFM and the spin-liquid phase, respectively. Note that these requirements for T and s are comparable to those demanded for the achievement of Néel order in spin-1/2 fermions in 3D lattices ($s \simeq 0.35k_B$) [52]. The different phases may be experimentally characterized by different means, including monitoring τ (taking Fig. 5.10 as a reference) in standard Stern-Gerlach-like experiments in time of flight, and using Faraday rotation, as recently proposed in Ref. [63]. Finally, note that with a shallow harmonic trap along the lattice, the MI phase occupies the central region, surface effects are negligible and our results apply.

5.7 Conclusions

In summary, spin-3/2 fermions present a rich diagram of Mott phases (Fig. 5.9) as a function of the scattering lengths and the QZE. Various types of phase transitions are predicted between a gapped dimerized phase, a gapless spin liquid, and an isotropic Heisenberg antiferromagnet. The latter phase occurs at large-enough QZE and is protected by a high $\mathrm{SU}(2) \otimes \mathrm{SU}(2)$ symmetry which
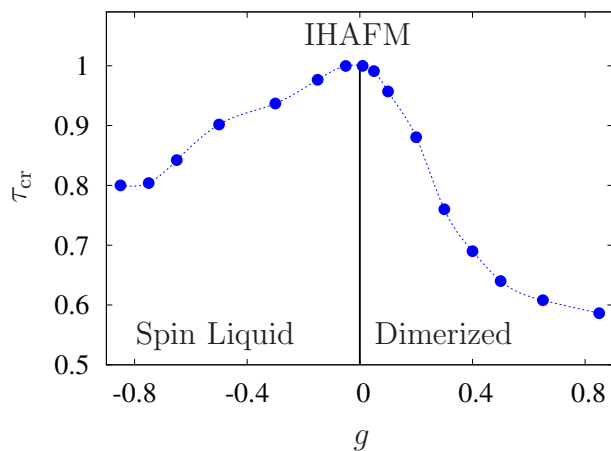
FIGURE 5.10: Critical chirality τ_{cr} at the field-induced phase transitions in Fig. 5.9 as a function of g.

remains at any QZE, contrary to the case of spinor bosons. These phases and phase transitions may be revealed in experiments with four-component fermions in optical lattices, under similar entropy and temperature requirements to those demanded for Néel ordering in spin-1/2 fermions in 3D lattices. We note, in particular, that four-component fermions constitute a unique scenario for experiments on a field-induced commensurate-incommensurate transition, which in a two-component case cannot be induced by a magnetic field due to the conservation of magnetization. Note that the spin-3/2 fermions are the smallest spin fermionic systems that exhibit spin-changing collisions (and hence sensitivity against QZE).

Field-induced phase transitions of repulsive spin-1 bosons

We study the phase diagram of repulsively interacting spin-1 bosons in optical lattices at unit filling, showing that an externally induced quadratic Zeeman effect may lead to a rich physics characterized by various phases and phase transitions. We performed numerical simulations in one-dimension to determine: the nature of the phase transitions for both antiferromagnetic and ferromagnetic interactions and the precise location of transition for the ferromagnetic case (the antiferromagnetic case is also discussed). Our numerical results are in excellent quantitative agreement with the analytical predictions from an effective field theory description which provides the precise location of the phase boundaries for any dimension. Our work provides a quantitative guide for the experimental analysis of various types of field-induced quantum phase transitions in spin-1 lattice bosons. These transitions, which are precluded in spin-1/2 systems, may be realized using an externally modified quadratic Zeeman coupling, similar to recent experiments with spinor condensates in the continuum.

6.1   Motivation

Spin-1 gases are the simplest spinor system beyond the two-component one. Depending on interparticle interactions [65, 67] (given by the s-wave scattering lengths $a_{0,2}$ for collisions with total spin 0 and 2), spin-1 BECs present a ferromagnetic (FM) ground state (for $a_0 > a_2$ as in ^{87}Rb $F = 1$ [71]) or an antiferromagnetic (AFM), also called polar, one (for $a_2 > a_0$, as in ^{23}Na [69]).

Most spin-1 species are naturally close to the $SU(3)$ point when $a_0 \approx a_2$, and where small external perturbations may have large effects in the quantum magnetic properties of the system. Since interactions preserve the magnetization, $\mathcal{M}$, the linear Zeeman effect (LZE) may be effectively gauged out, although the phase diagram depends on $\mathcal{M}$ [74, 78]. On the contrary, as we saw in previous chapters, the quadratic Zeeman effect plays a crucial role in spinor gases. In spite of its importance, the role of the QZE in the quantum phases of spin-1 lattice bosons remains to a large extent unexplored, with the sole exception of the recent 3D mean-field analysis of Ref. [78], where it was

shown that for finite $\mathcal{M}$ the QZE may lead to nematic-to-ferromagnetic (or partially magnetic) transitions.

This chapter discusses the phase diagram (Fig. 6.7) for MI phases at unit filling of repulsively interacting spin-1 bosons in the presence of QZE, for the experimentally relevant case of a balanced mixture, i.e. with $\mathcal{M} = 0$. We analyze in detail the magnetic phases and quantum phase transitions in 1D (and a short overview in 2D and 3D) around the multi-critical ferromagnetic SU(3). We combine and compare the 1D MPS calculations with an effective field theory (for any dimension) and the exact Lanczos diagonalization. Obtaining an excellent quantitative agreement between the different methods. We identify the nature of the phase transitions and we determine quantitatively the transition lines for the ferromagnetic case, finally the antiferromagnetic side is also regarded. We note that the QZE may be controlled by means of microwave and optical techniques [92, 93].

Hence, as recently demonstrated for spinor BECs in the continuum [86], our results show that a controlled quenching of the QZE may permit the observation of field-induced phase transitions in spin-1 lattice bosons, which are precluded by simple use of the LZE due to conservation of $\mathcal{M}$, and thus are absent in spin-1/2 systems. In addition, optical Feshbach resonances [94, 95] permit the modification of the ratio a_2/a_0, so that the full phase diagram discussed below may be explored with state of the art techniques.

6.2 Anisotropic Heisenberg Hamiltonian

Following the same spirit of Section 5.2, we want to analyze the limiting case when the magnetic field is much larger (but finite) than the critical values where the phase transitions are located, $|D_c|$. To do so, we start from the effective Hamiltonian derived previously, Eq. (4.33), which is valid for all field values, instead of starting from the Hamiltonian, Eq. (4.38), which is valid only up to $|q| \sim t^2$ which means $|D| \sim 1$.

The scenario in spin-1 bosonic systems is completely different from the one observed in spin-3/2 fermions. The case of $D \gg 1$, corresponds to the manifold $m = \pm 1$ behaving like pseudo-spin-1/2, while, the case of $D \ll -1$ corresponds to $m = 0$ which resembles spinless bosons. This fact, breaks the symmetry on the QZE and different behavior is expected.

Let us analyze first the case where the $m = \pm 1$ manifold is picked. We found that the Hamiltonian reduces to an anisotropic Heisenberg (AH) form

$$\hat{H}_{AH} = \sum_i \left(J \left[\hat{S}_i^x \cdot \hat{S}_{i+1}^x + \hat{S}_i^y \cdot \hat{S}_{i+1}^y \right] - (J - 8c_2)\hat{S}_i^z \cdot \hat{S}_{i+1}^z + \eta \hat{I}_{i,i+1} \right) \quad (6.1)$$

with

$$
\begin{aligned}
J &= 2\left[c_1 + c_{sc}\epsilon\right], \\
\eta &= \left[2m^2 + 2c_2 + J/2\right], \\
\epsilon &\equiv \frac{c_{sc}}{2q + 2c_1 - c_0} \ll 1,
\end{aligned}
\tag{6.2}
$$

where the coefficients c_1, c_0 and c_{sc} are defined in the set of Eq. (4.35). Particularly in the antiferromagnetic side, when $g_2 > g_0$, the Hamiltonian Eq. (4.38) reduces to an anisotropic Heisenberg antiferromagnet contrary to spin-3/2 systems.

On the other hand, for the case where $m = 0$ is chosen, the system has only one component (spinless) and the energy with correction is given by $E_{00} = c_0 - 2c_{sc}\epsilon$, where ϵ is defined in Eq. (6.2).

6.3 The effective spin-model

We consider *the effective spin-model* under the influence of an external field derived in Chapter 4. As already discussed, in the insulating state, fluctuations in the particle number on each site are suppressed but not frozen out completely. Then, virtual tunneling of atoms between neighboring lattice sites gives rise to effective spin-exchange interactions that determine the spin structure of the MI states. We recall that the effective Hamiltonian is given by

$$
\widehat{H} = -J\left[\sum_{\langle ij \rangle} \cos\theta \vec{S}_i \cdot \vec{S}_j + \sin\theta \sum_{\langle ij \rangle} \left(\vec{S}_i \cdot \vec{S}_j\right)^2\right] - DJ\sum_i \left(S_i^z\right)^2,
\tag{6.3}
$$

where $D = -q/J$ is the QZE strength and $J \equiv 1$. And θ is defined by

$$
\arctan(\theta) = \frac{-(g_0 + 2g_2)}{-3g_0}.
\tag{6.4}
$$

The angle θ takes values in the interval $[-\pi/2, -\pi + \arctan(1/3)]$ as the ratio g_0/g_2 of scattering lengths in $F = 2$ and $F = 0$ channels varies from 0 to $+\infty$. Hence, we focus on the MI magnetic properties using this effective model as a function of D and θ.

Ferromagnetic interactions, $\theta < -3\pi/4$: For $D \geq 0$ the ground state is a fully polarized ferromagnet in either $m = \pm 1$ (Ising-FM), and since $\mathcal{M} = 0$ phase separation into ferromagnetic $m = \pm 1$ domains is expected. At $D = 0$ an SU(2) symmetry spontaneously breaks and a Z_2 symmetry at $D > 0$.

For $D < 0$ the ground state for small values of $|D|$ is an XY-ferromagnet (XY-FM), i.e. the system fulfills $\langle S_i^z \rangle = 0$, but presents a non-zero transversal magnetization. This phase is ordered in dimensions $d \geq 2$, exhibiting in 1D a quasi-long-range order with leading power-law decay of xy spin correlations. For larger $|D|$ (keeping $D < 0$) there is a phase transition between the XY-FM and the so-called large-D phase (also called Ising-nematic), in which all atoms are in the $m = 0$ Zeeman substate, and hence all spin correlations decay exponentially. The field-induced phase transition between large-D and XY-FM is discussed in detail below.

Multi-critical point, $\theta = -3\pi/4$: In alkaline atoms the scattering lengths $a_{0,2}$ are naturally close to each other, which corresponds to the vicinity of the point $\theta = -3\pi/4$. This point exhibits an enlarged symmetry and corresponds to an SU(3) ferromagnet [79–81] that has highly degenerate ground state unifying many types of order [83]. In the vicinity of this multi-critical point the effect of an external magnetic field is especially drastic since it breaks the high symmetry and favors phases with different types of spin-nematic and ferromagnetic order.

Antiferromagnetic interactions, $\theta > -3\pi/4$: The dominant correlations are of spin-nematic (quadrupolar) type [79, 81]. A XY-nematic phase occurs for $D > 0$, characterized for $d \geq 2$ by $\langle (S^+)^2 \rangle \neq 0$ and $\langle \mathbf{S} \rangle = 0$, and in 1D by power-law correlations of the quadrupolar order parameter and exponentially decaying in-plane spin correlations.

On the contrary, for $D < 0$ the large-D phase is favored. In 1D, for $D = 0$ a dimer nematic phase is expected [66, 68, 72, 73, 76, 81, 82]. We show below that in 1D the QZE induces a phase transition from the dimer-nematic phase to either the XY-nematic for $D > 0$ or large-D for $D < 0$. Implying that this side of the phase diagram may contain up to three different phases, depending on the problem dimensionality.

6.4 Quantum phase transitions: numerical and theoretical treatment

Quantum systems can be analytically solved in suitable limiting cases. For the numerical solutions the panorama is not better in many ways, and very modern techniques have been developed to address correctly the ground state and the low-lying states properties. Let us summarized the tools we use in order to study our system.

Fidelity and fidelity-susceptibility calculations. Let us consider quantum phase transitions which are not induced by level crossings, either in the ground state or between low-lying excited states (considering a non-degenerate ground state). When the transition is achieved by the change of a parameter $\lambda \to \lambda + \delta\lambda$, where $\delta\lambda \ll \lambda$, a natural quantity to follow is the *fidelity* [147], already introduced in Chapter 3 between time-evolved states and a ground state. In the present context, we write the fidelity as

$$\mathcal{F}(\lambda, \delta\lambda) = |\langle\psi(\lambda)|\psi(\lambda + \delta\lambda)\rangle|^2. \tag{6.5}$$

$\mathcal{F}$ is defined as the Hilbert-space distance between the ground state $|\psi(\lambda)\rangle$ and the slightly shifted ground state $|\psi(\lambda + \delta\lambda)\rangle$. At the phase transition point, λ_c, the fidelity depends strongly on $\delta\lambda$. Therefore, the most relevant quantity in determining the fidelity changes is its second derivative. Hence, we use the *fidelity susceptibility* defined by

$$\chi_F(\lambda) = \lim_{\delta\lambda\to 0} \frac{-2\ln\mathcal{F}(\lambda + \delta\lambda)}{\delta\lambda^2} = -\frac{\partial^2\mathcal{F}}{\partial(\delta\lambda)^2}. \tag{6.6}$$

The fidelity susceptibility is an interesting figure of merit to describe the phase transitions with lack of level crossings. Contrary to other figures as correlation functions. $\chi_F(\lambda)$ behaves controllably sharp and shows the critical parameter value where the transition occurs λ_c. One should study this quantity scanning several steps and system sizes. Thereafter, a finite-size scaling should be performed to obtain reliable results.

Level spectroscopy. As in the previous chapter, here, the *Lanczos algorithm* to calculate the ground state and the low-lying excited states is very useful. By means of this method, A. Argüelles studied the phase transitions present in the antiferromagnetic region of the phase diagram [163], exploding the level crossings .

Effective field theory To study the phase diagram near the SU(3) point, A. K. Kolezhuk in collaboration with T. Vekua developed a low-energy effective field theory [132, 169] based on spin-1 coherent states

$$|\psi\rangle = \sum_{a=x,y,z} (u_a + iv_a)|t_a\rangle, \tag{6.7}$$

where $|t_a\rangle$ are three Cartesian spin-1 states

$$\begin{aligned}
|t_z\rangle &\equiv |m = 0\rangle, \\
|t_x\rangle &\equiv -\frac{1}{\sqrt{2}}\left(|m = +1\rangle - |m = -1\rangle\right), \\
|t_y\rangle &\equiv \frac{\imath}{\sqrt{2}}\left(|m = +1\rangle + |m = -1\rangle\right).
\end{aligned} \tag{6.8}$$
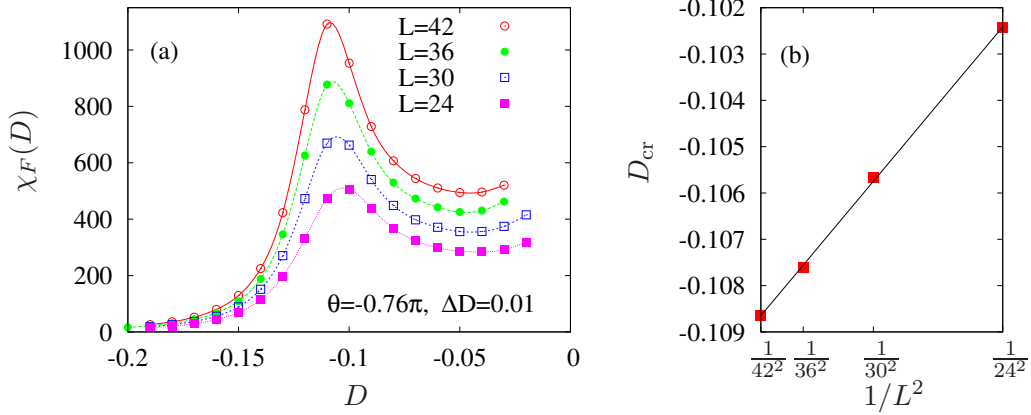
FIGURE 6.1: (a) Fidelity susceptibility $\chi_F(D)$ at $\theta = -0.76\pi$ for several system sizes. It shows the critical field at which the transition between XY-ferromagnetic and large-D phases occurs. The calculations has been done using MPS. (b) Peak position fitting to $1/L^2$ confirming the Kosterlitz-Thouless phase transition nature.

The real vectors $\vec{u}$, $\vec{v}$ (defined at each lattice site $\mathbf{n}$) satisfy the constraints $\vec{u}^2 + \vec{v}^2 = 1$, $\vec{u} \cdot \vec{v} = 0$. The vector $\vec{u}$ plays the role of director vector for the nematic phases discussed below. The average spin on a site fulfills $\vec{M} \equiv \langle \psi | \vec{S} | \psi \rangle = 2(\vec{u} \times \vec{v})$.

6.5 Ferromagnetic interactions ($\theta < -3\pi/4$)

6.5.1 XY-FM to Large-D phase transition ($D < 0$)

We have numerically evaluated the transition between the large-D phase to XY-ferromagnetic phase in 1D by means of MPS calculations for up to 42 sites. We locate the phase transition boundary studying the fidelity susceptibility, $\chi_F(D)$, between the ground states at two values of the QZE coupling, D and $D + \Delta D$. Figure 6.1(a) shows the peak developed in $\chi(D)$ while we scan the field D. The finite-size scaling of the peak position, as a function of the lattice size L, follows very accurately a $1/L^2$ law as it is shown in Fig. 6.1(b), confirming its Kosterlitz-Thouless character.

Interestingly, the fidelity susceptibility is an efficiency measurement to describe this Kosterlitz-Thouless transition, contrary to others, like correlation functions, because it behaves sharply and therefore, it shows clearly the critical field where the transition occurs. It is remarkable since in 1D only a quasi-long-range order is generated. We have used several scanning steps ($\Delta D = \{0.01, 0.02, 0.005, 0.002\}$) for several system sizes ($L = \{24, 30, 36, 42\}$) to extrapolate the peak position in the thermodynamic limit. The numerical data
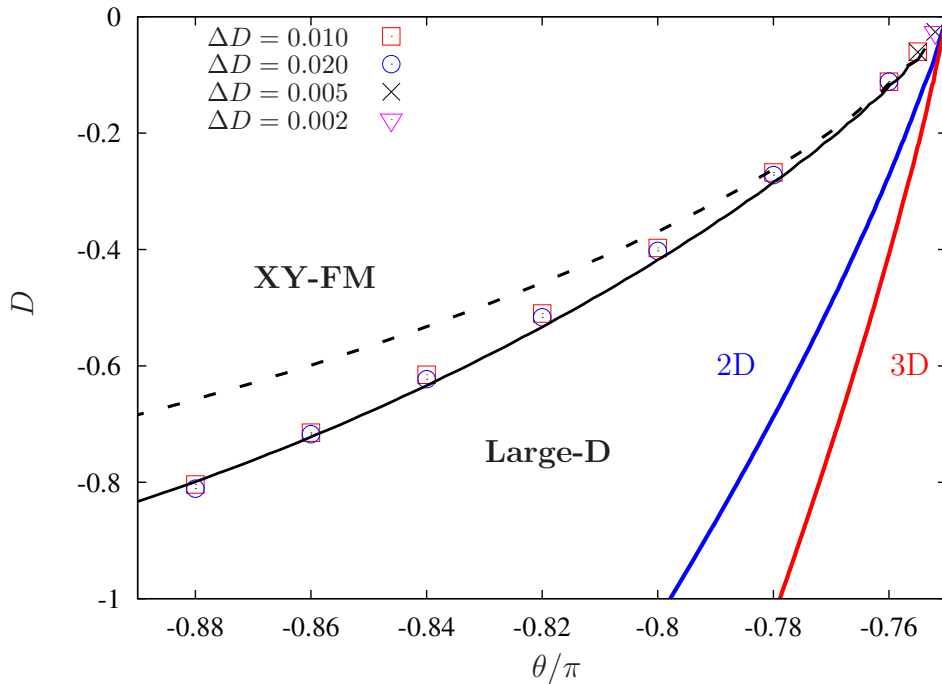
FIGURE 6.2: Phase transition between the XY-FM and large-D phases. The symbols denote the extrapolated MPS data for several ΔD. The solid line is obtained from the field theory description Eq. (6.10) for $d = 1$ with the fitting parameter $g_c \simeq 0.6$. Transition curves neglecting fluctuations: dashed line for $d = 1$ with $g_c \simeq 1.2$, blue line for $d = 2$ and red line for $d = 3$.

is shown in Fig. 6.2, which, agrees perfectly with the effective field-theoretical description after fitting the single parameter $g_c \simeq 0.6$, solid line (see the discussion below).

The low-energy effective field theory, developed by A. K. Kolezhuk and T. Vekua [132, 169], describes the phase transition between XY-FM and large-D phases. For $d = 1$, this is a Kosterlitz-Thouless (KT) transition, and the XY-FM phase has only a quasi-long-range order. For $d \geq 2$, the phase transition belongs to the $(d + 1)$-dimensional XY universality class given by the model

$$\mathcal{A}_{XY} = (\Lambda^{d-1}/2g) \int d^{d+1}x (\partial_\mu \varphi)^2, \qquad (6.9)$$

Λ is the ultraviolet lattice cutoff and the renormalized coupling constant g, acting as an effective temperature, reads

$$g^{-2} = \frac{1}{2Z} \left[\frac{1-\eta}{\eta} + \frac{\langle \delta^2 \rangle}{2\eta^4} \right] \left[\left(1 - \eta \right) \left(\lambda + 1 + \eta \right) + \langle \delta^2 \rangle \left(1 + \frac{\lambda}{2\eta^3} \right) \right], \quad (6.10)$$

where Z is the lattice coordination number and

$$\langle \delta^2 \rangle = g_\delta C_d \pi^{1-d} \int_0^\pi \frac{dk\, k^{d-1}}{\sqrt{m_\delta^2 + k^2}} \quad \text{is the longitudinal spin fluctuation strength,}$$

$$g_\delta^2 = (8Z\eta^4)/(\lambda + 2\eta^2) \quad \text{is the classical coupling constant,}$$

$$m_\delta^2 = 2Z(1 - \eta^2)/(\lambda + 2\eta^2) \quad \text{is the mass of the } \delta \text{ fluctuations, and}$$

$$C_d^{-1} = (4\pi)^{d/2}\Gamma(d/2).$$

The convenient variables η and λ are defined by

$$\lambda \equiv \tan\theta/(1 - \tan\theta) \quad \text{and} \quad \eta \equiv |D|/2Z(\sin\theta - \cos\theta). \tag{6.11}$$

The model of Eq. (6.9) establishes the transition at a non-universal coupling constant $g = g_c$. Once g_c is known, Eq. (6.10) constitutes an implicit equation to determine the transition function $D(\theta)$. The curve has a *universal slope* for $\lambda \to \infty$ ($\theta \to -3\pi/4$, $SU(3)$ point) given by $\eta = 1 - O(\lambda^{-1/2})$ or in other words

$$|D| = 2Z(\sin\theta - \cos\theta). \tag{6.12}$$

Figure 6.2 shows the curve (solid black line), for $d = 1$, obtained after adjusting the single fitting parameter g_c to the numerical results retrieved from the finite-size scaling of the fidelity susceptibility. An excellent agreement with the numerics is obtained for $g_c \approx 0.6$.

In higher dimensions, $d \geq 2$, one may expect the effect of fluctuations to become less important, so the transition line will be satisfactorily described by setting $\langle \delta^2 \rangle = 0$, i.e., by neglecting in Eq. (6.10) the longitudinal spin fluctuations,

$$g_{\langle \delta^2 \rangle \equiv 0}^{-2} = \frac{(1 - \eta)^2}{2Z\eta}(1 + \lambda + \eta) \tag{6.13}$$

and demanding the critical $|D|$ to match the Ising value which leads $g_c = (8Z/5)^{1/2}$. For $d \geq 2$, the XY-FM phase is ordered with a spontaneously broken $U(1)$ symmetry ($\varphi = \varphi_0$ where $\varphi \in [0, 2\pi]$), and the order parameter $\langle \cos\varphi_0 S^x + \sin\varphi_0 S^y \rangle \neq 0$. Whereas, for $d = 1$ only a quasi-long range order is obtained. In Fig. 6.2 we also plot the $D(\theta)$ transition line calculated without fluctuations for 1D (dashed line). As expected, the curve does not match the numerical data, nevertheless the overall shape of the transition line is not affected by the correction, particularly the universal slope. Figure 6.2 also shows, the corresponding transition curves obtained from the implicit Eq. (6.13) for 2D and 3D, blue and red curves, respectively.
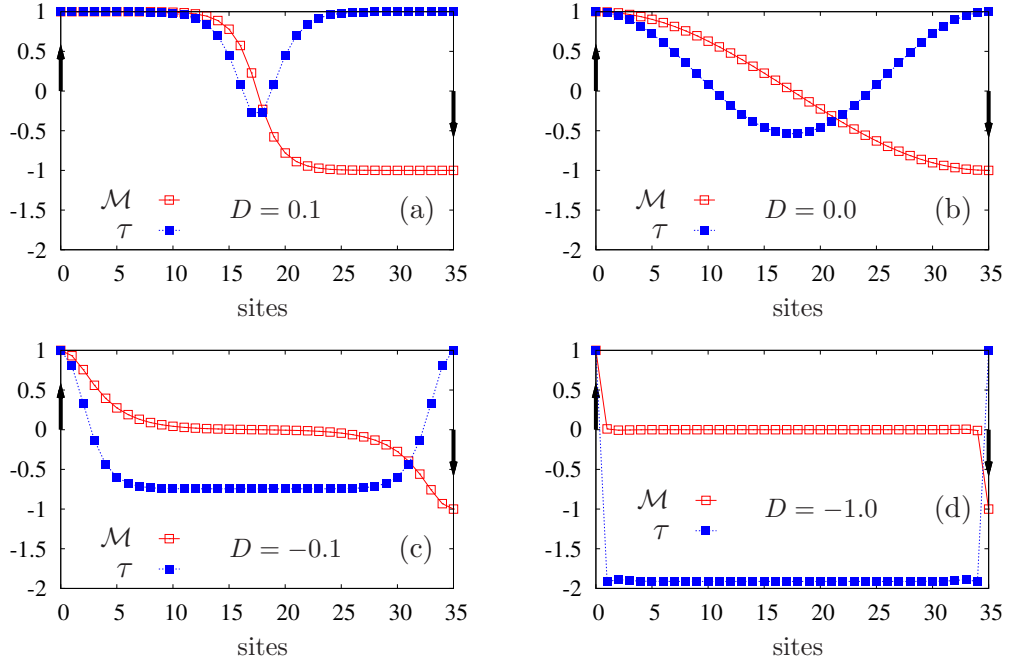
FIGURE 6.3: Chirality and magnetization profiles are presented for four specific cases. (a) Ising-FM phase, the $m = 0$ components are located where τ is depleted and $\mathcal{M}$ saturates to $m = \pm 1$ in the two halves while $\tau = 1$. (b) $D = 0$, maximal degeneracy where $1 \leq \tau \leq -0.5$ and $1 \leq \mathcal{M} \leq -1$ both behaving smoothly. (c) XY-FM phase, considerable reduction of $m = \pm 1$ population whereas (d) shows the large-D with total suppression of $m = \pm 1$ is presented.

6.5.2 Ising-FM to XY-FM $(D > 0)$

As it was commented before, for positive values of the QZE the system becomes a fully polarized ferromagnetic phase in either $m = 1$ or $m = -1$, the so-called Ising-ferromagnet. Nevertheless, since the system is prepared in a balanced mixture, $(\mathcal{M} = 0)$, domain walls appear throughout the lattice. In order to analyze this feature, we study the magnetization and chirality profiles. The chirality in spin-1 systems is defined by

$$\tau = \frac{1}{L} \sum_i (\hat{n}_{i,+1} + \hat{n}_{i,-1} - 2\hat{n}_{i,0}) = \frac{1}{L} \sum_i \left\{ 3(S_i^z)^2 - 2 \right\}, \qquad (6.14)$$

which can be easily monitored in Stern-Gerlach-like time-of-flight experiments.

To evidence the spin domains, we have added fields at the edges of the chain, left up and right down, as it is shown in Fig. 6.3 and scan the external field. In Fig. 6.3(a) the system is in the Ising-FM phase, where the left and right halves of the chain are polarized in $m = +1$ and $m = -1$, respectively, presenting a saturation in the chirality and a sign inversion in the magne-

tization. Moreover, in the mid part of the chain the population of $m = 0$ is located, generating a notable depletion in the chirality. Experimentally it is notable, since it constitute a way to measure the amount of a given hyperfine state, particularly $m = 0$ state. As soon as the QZE is decreased the population in $m = 0$ becomes more relevant, in the absence of the field, Fig. 6.3(b), the three components are totally degenerate and the τ evolves smoothly from 1 in the edges to -0.5 in the middle. $\mathcal{M}$ also inverts its sign smoothly. For negative values of D the system presents a strong reduction in the $m = \pm 1$ population, as it is shown in Figs. 6.3(c) and 6.3(d), where one finds the XY-FM and large-D phases, respectively.
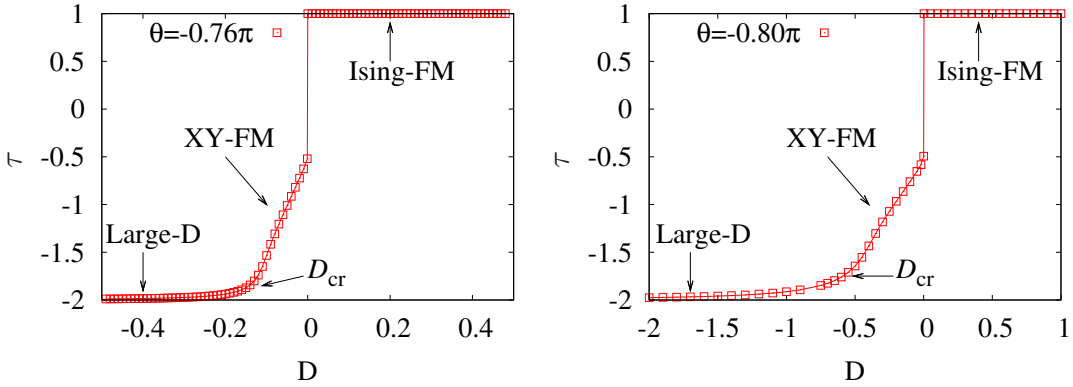
FIGURE 6.4: Chirality τ as a function of D for two angles $\theta = -0.76\pi$ and $\theta = -0.80\pi$. The different phases and the critical field are explicitly shown. The jump of the first order phase transition is also observed.

In this ferromagnetic side, the chirality as a function of the QZE shows a particular behavior for each involved phase. The numerical data is presented in Fig. 6.4 for two different values of θ. One can observe the discontinuity at $D = 0$ indicating the first-order character of the transition between the Ising-FM and the XY-FM. It is clear since for the Ising-FM phase $(D > 0)$ $\tau = 1$, while in the XY-FM phase $(D_{cr} < D < 0)$ for $D \to 0^-$, $\tau \to -\frac{1}{2}$.

This particular value of the chirality at $D \to 0^-$ is explained from the fact that the ground state energy is minimized by picking one of the eigenstates of the operator $\hat{S}^x(\hat{S}^y)$ with eigenvalue +1 or -1 per site (since $\mathcal{M}_i = \pm 1$ per site although $\mathcal{M} = 0$ in the whole lattice). Then, after solving

$$\hat{S}^{x,y}|\alpha_\pm^{x,y}\rangle = \pm 1|\alpha_\pm^{x,y}\rangle, \tag{6.15}$$

one can calculate

$$\langle \alpha_\pm^{x,y}|(S^z)^2|\alpha_\pm^{x,y}\rangle = 1/2, \quad \text{thus} \quad \langle \alpha_\pm^{x,y}|\tau|\alpha_\pm^{x,y}\rangle = -1/2. \tag{6.16}$$

In the XY-FM to large-D transition, where τ saturates to -2, the chirality behaves smoothly as the Kosterlitz-Thouless transitions usually are. Nonetheless, it presents a shoulder for values of D very close to the one obtained

previously by the fidelity susceptibility analysis (see Fig. 6.2). In Fig. 6.4, such value is depicted as D_{cr}. As it was already pointed out, these transitions could be revealed experimentally by Faraday rotation techniques [63] or those recently explored in Ref. [170].

6.6 Antiferromagnetic interactions

For the antiferromagnetic region, $\theta > -3\pi/4$, the effective theory can be formulated in terms of the nematic director $\vec{u}$, in the frame work of an effective field theory of A. K. Kolezhuk and T. Vekua [132, 169]. The director anisotropy is of the easy-plane (easy-axis) type for $D>0$ ($D<0$). It has been shown that for $d \geq 2$ there is a long range nematic order for any D, with a single transition at $D=0$, between a gapless XY-nematic phase with $\langle (S^+)^2 \rangle \neq 0$ at $D>0$ and a gapped Ising-nematic $\langle (S^z)^2 \rangle = 0$ at $D<0$. Whereas for $d=1$, a dimerized phase spontaneously appears between these two nematic phases.

Although the field theory cannot describe dimerization, it may be employed to determine the boundaries between the XY-Nematic and Ising nematic phases with the dimerized phase, at very small $|D|$. When $D > 0$, this transition is Kosterlitz-Thouless, and the transition line close to the $SU(3)$ point fulfills $D = CJ_2 \exp\{-4\pi(1 - J_1/J_2)^{-1/2}\}$, where $C > 0$ is a numerical constant. At $D < 0$ the phase transition is Ising-like, with a boundary similar as for $D > 0$, but a negative constant $\tilde{C}$. As shown below, this analysis provides a good insight on the dimer-to-nematic transitions.

6.6.1 Dimer to nematic transitions

To characterize the boundaries of the dimerized phase, one should perform numerical calculations. Unfortunately the fidelity susceptibility remains featureless in this region of the phase diagram. Moreover, level spectroscopy analysis should be employed [162], since the transition presents sharp level crossings.

Level spectroscopy. As discussed in previous chapters, in a finite chain, two dimerized ground states (degenerate in the thermodynamic limit) split in energy, so the lowest excited state in the dimerized phase is unique and belongs to the $\mathcal{M} = 0$ sector. In contrast, both in the large-D phase ($D < D_c^-$) and in the XY-nematic ($D > D_c^+$), the lowest excited states are twofold degenerate, having $\mathcal{M} = \pm 1$ and $\mathcal{M} = \pm 2$, respectively. Thus, in finite chains a level crossing between the lowest excited singlet and doublet states occurs when changing D. The extrapolated results, obtained by A. Argüelles [132, 163], for $D_c^\pm$, using Lanczos diagonalization for periodic systems of up to $L = 16$ sites, are shown in Fig. 6.7 with $\triangle \to D_c^+, \square \to D_c^-$. Note that when

approaching the $SU(3)$ point the numerical simulations cannot recover the exponentially small dimer region, which basically reduces to $D = 0$ line. The finite size extrapolation of D_c^+ follows $1/L^2$ law, confirming its Kosterlitz-Thouless nature.

Central charge. To determine the universality class of the $D = D_c^-$ transition, we have computed the central charge at $D = 0$, $\theta = -0.73\pi$. This value lies in the region where the XY-nematic and large-D phases meet each other at $D = 0$. Strictly speaking, this point is inside the dimerized phase, but since the correlation length is extremely large, the system can be considered as gapless.

The block entanglement entropy for an open 1D system of size L, divided into two pieces of size l (block) and $L - l$ (environment), behaves as

$$\mathcal{S} = \frac{c}{6} \log \left[\frac{L}{\pi} \sin \left(\frac{\pi l}{L} \right) \right] + A, \tag{6.17}$$

where c is the central charge and A is a non-universal constant [127, 171]. Setting $l = \frac{L}{2}$, following Ref. [172], and using MPS method to evaluate $\mathcal{S}$ for several L values, finally the central charge is obtained from the slope of the curve, as it is shown in Fig. 6.5. By this method, we obtain $c \simeq 1.5$. The $D = D_c^+$ Kosterlitz-Thouless line has $c = 1$; subtracting its contribution, we get $c = \frac{1}{2}$ for the $D = D_c^-$ line, confirming its Ising nature.
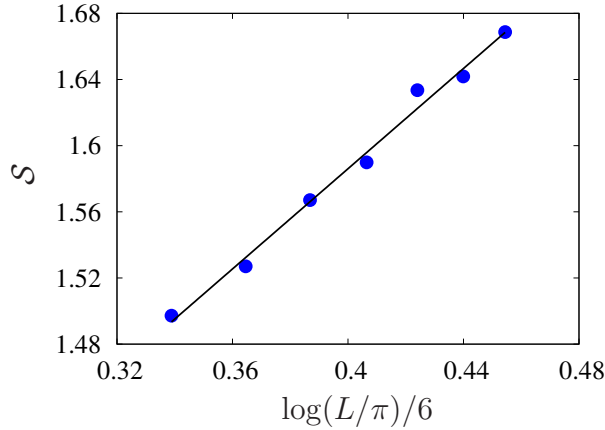
FIGURE 6.5: Central charge retrieved from the slope of the block entanglement entropy $\mathcal{S}$. The calculation has been performed at $\theta = -0.73\pi$ for several system lengths. The fitting curve is given by $f(x) = 1.51508x + 0.980015$ whose slope is $c = 1.515 \pm 0.065$.

Chirality. Finally, we study the chirality τ as a function of D for antiferromagnetic interactions. In this region, the dimer to nematic phase transitions

do not present any pronounced feature, neither for the limit $D \to 0$ where $\tau = 0$, nor for $D > 0$ and $D < 0$ where $\tau \to 1$ and $\tau \to -2$, respectively. A couple of examples are presented in Fig. 6.6. One can see the smooth behavior of the chirality for angles close to $\theta = -0.5\pi$ but as one approaches the SU(3) point, $\theta = -0.75\pi$, the chirality starts to show the sharp behavior we already saw in Fig. 6.4.
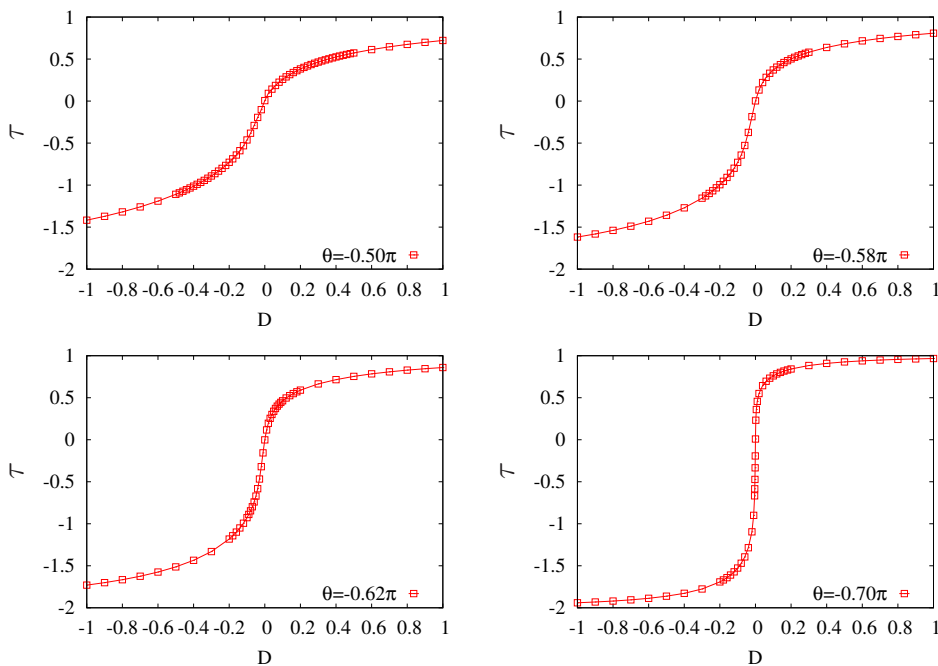
FIGURE 6.6: The chirality τ, as a function of D for several values of θ, for antiferromagnetic interactions.

6.7 Spin-1 Mott insulator phase diagram

The phase diagram of repulsively interacting spin-1 bosons in optical lattices at unit filling in the presence of an externally induced quadratic Zeeman field is presented in Fig. 6.7. We have obtained, using the MPS method for up to 42 sites, for ferromagnetic interactions and negative values of D, the phase transition line between the XY-ferromagnetic and large-D phases. It has been done by means of the fidelity susceptibility studies whose finite size extrapolation leads to $1/L^2$ law, confirming that this is a transition of the Kosterlitz-Thouless type.

For antiferromagnetic interactions, we have retrieved the critical field curves $D_c^{\pm}$, using Lanczos diagonalization for periodic systems of up to $L = 16$ sites. In the figure, the D_c^{+} curve (triangles) represents the transition between the

dimerized and the XY-nematic phases. Its finite size extrapolation follows a $1/L^2$ law, confirming the Kosterlitz-Thouless nature with central charge $c = 1$. The D_c^- curve (squares) shows the transition between dimerized and large-D phases. We showed by means of MPS calculations that this is an Ising-like transition since its central charge is $c = 0.5$. When approaching the $SU(3)$ point the numerical simulations cannot recover the exponentially small dimer region, which basically reduces to $D = 0$ line.
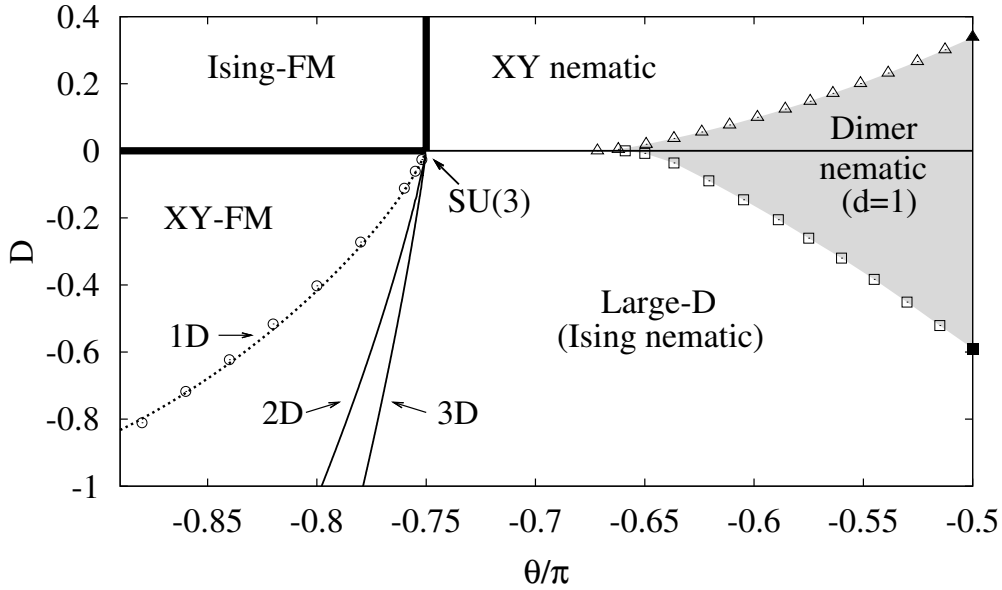
FIGURE 6.7: Mott phases of spin-1 lattice bosons at unit filling, as a function of θ and the QZE D. Thick solid bold lines correspond to first order phase transitions for any d. The symbols represent numerical data for $d = 1$. Kosterlitz-Thouless transition line in the FM side (circles), and in the AFM side: the Kosterlitz-Thouless transition for D_c^+ (triangles) and the Ising-like transition for D_c^- (squares), limits of the dimerized phase (Grey region only in 1D). The XY-FM to large-D transition lines retrieved from field-theory are represented by dashed line for 1D, and the solid lines correspond to 2D and 3D as it is shown.

6.8 Conclusions

In summary, we have obtained the complete phase diagram (for any dimension) for spin-1 lattice bosons in the MI phase (at unit filling) in the presence of quadratic Zeeman coupling. Our results provide hence a quantitative guide for the analysis of field-induced quantum phase transitions in lattice bosons, which, similar to recent experiments with spinor BECs in the continuum [86], may be realized modifying the QZE by means of microwave dressing. Starting

in the large-D phase, and dynamically modifying the QZE across the transitions discussed in this paper, should result in the FM regime in the appearance of XY-FM domains, similar to those observed in spin-1 BECs [86], whereas quenches in the AFM regime should lead to nematic domains with different $\langle (S_{x,y})^2 \rangle$ but homogeneous $\langle \vec{S} \rangle = 0$. We stress that such field-induced transitions are precluded for spin-1/2, constituting an interesting novel feature of lattice spinor gases.

Conclusions and outlook

In this Thesis we have discussed different topics related to ultra-cold lattice gases. We have first briefly introduced the main concepts related to the physics of ultra-cold gases, and in particular we have pointed out the importance of such systems as quantum simulators. Numerical methods are necessary to efficiently describe the different features of those models. We have reviewed in Chapter 2 those numerical methods used in this Thesis. Note, that most of the methods were developed in the course of this PhD thesis in strong collaboration with A. Argüelles [163].

In Part I, we have used the Hubbard model for the description of a cold atomic Bose gas loaded in a time-dependent optical lattice in the deeply correlated superfluid regime. We have shown that the evolution is characterized by a transient non-equilibrium state in which quasi-local correlation functions have already converged into a new equilibrium whereas long-range correlations and the quasi-condensate fraction present still a significant time dependence. Additionally, we have analyzed the formation at a longer time scale of a new equilibrium from an initial gas at zero temperature. By considering the fidelity with respect to the ground state of the final configuration we have shown that even rather mild ramps do not fully guarantee a perfect loading of the new ground state. We have however shown that contrary to the harmonic regime [145] progressively milder ramps lead to a more adiabatic transfers.

Part II was devoted to spinor lattice gases that offer interesting physics, most relevantly on the field of quantum magnetism. We have taken into account the crucial role that the quadratic Zeeman effect plays in the magnetic properties of ultra-cold spinor systems. In Chapter 4 we have introduced the external field and analyzed in detail the calculation of the low-energy effective spin Hamiltonian in the hard-core limit with super-exchange interactions, by means of perturbation theory and symmetry considerations, for both spin-3/2 fermions and spin-1 bosons. This effective model allowed us for the study of the magnetic phases inside the Mott regime, and the quantum phase transitions between the involved phases.

In Chapter 5, we have studied the rich MI phase diagram for spin-3/2 fermions as a function of the spin-changing collisions and the QZE. We have shown that the quadratic field preserves an $SU(2) \otimes SU(2)$ symmetry, leading for large-enough coupling to an isotropic pseudo-spin-1/2 Heisenberg antiferromagnetic phase. Decreasing the field this phase undergoes, depending on

the scattering lengths, either a Kosterlitz-Thouless transition into a gapped dimerized phase or a commensurate-incommensurate transition into a gapless spin liquid. This constitutes a unique scenario for experiments on a field-induced C-IC transition, which in a two-component case cannot be induced by a magnetic field due to the conservation of magnetization. This interesting phase diagram can be observed experimentally in four-component fermions in optical lattices under similar entropy constraints to those required for Néel order in spin-1/2 gases. We remark that the spin-3/2 fermions are the smallest spin fermionic systems that exhibit spin-changing collisions (and hence sensitivity against QZE).

In Chapter 6 we have studied the field-induced phase diagram of repulsively interacting spin-1 lattice bosons in the presence of quadratic Zeeman field for both ferro and antiferromagnetic interactions, for the average filling of one boson per site. We have performed 1D numerical simulations to determine the nature and the precise location of the phase transitions. Our numerical results are in excellent quantitative agreement with the analytical predictions of an effective field theory description which provides the location of the phase boundaries for any dimension. Our work provides a quantitative guide for the experimental analysis of various types of field-induced quantum phase transitions in spin-1 lattice bosons. These transitions, which are precluded in spin-1/2 systems, may be realized using an externally modified quadratic Zeeman coupling, similar to recent experiments with spinor condensates in the continuum.

Let us outline the potential of the system models and methods considered in this Thesis and point out possible further applications.

Extension of dimensionality.   A rich physics is also expected in ladder-like and square lattices loaded with spin-3/2 fermions. We have shown in Chapter 5 by means of strong coupling analysis that the spin-changing processes lead to an antiferromagnetic frustrating next-nearest-neighbor exchange of the order $\mathcal{O}(\tilde{q}^{-2})$. In dimensions higher than 1D, those terms induce frustrating diagonal and third neighbor exchanges. On ladders an Ising phase transition is expected from a rung-singlet phase to a columnar-dimer state with increasing frustration [173], while on a square lattice the Néel state may undergo a phase transition into a spin-disordered state possibly via a second-order transition showing deconfined quantum criticality [174]. By means of variational-MPS method together with Lanczos diagonalization, it may be possible to study the ground state properties of spin-3/2 systems in a ladder configuration.

Extension of the phase diagram.   We have study in Chapter 6 the interval of the angle $\theta \in [-\pi/2, -\pi + \arctan(1/3)]$ relevant for the current ultra-cold atoms experiments with Rb and Na. This limits the possible phases which

can be studied, recalling the phase diagram reviewed in Section 4.3. More elaborated ideas, involving arrange of electric and magnetic fields to vary at will the coupling constants [153], may allow for exploring all the values of the angle $\theta \in [0, 2\pi]$ and thus all the possible phases.

Particularly interesting is the extension of the phase transitions lines for the dimerized phase ($\theta > -0.5\pi$). Lanczos method proved to be a reliable method to study phase transitions where level crossings are involved. Figure 7.1 shows a preliminary result for a system size of $L = 10$.
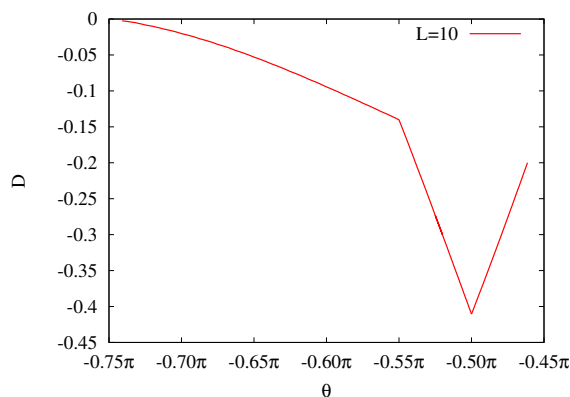
FIGURE 7.1: Extension of the dimerized to large-D phase transition line, for $\theta > -0.5\pi$ and system size $L = 10$. Results retrieved with Lanczos algorithm.

The ferromagnetic transition line between XY-FM and large-D phases would be also interesting to extend all the way through the ferromagnetic region until $\theta = \pi/2$ for the one-dimensional case. Figure 7.2 presents the respective lines for 2D and 3D obtained with the field theory discussed in Ref. [132].

Extension to the superfluid regime. In Ref. [175], a model of one dimensional spin-1 bosons with effectively repulsive density-density interactions and antiferromagnetic exchange is considered. They use a low-energy effective field theory (similar to the one mentioned in Chapter 6) to study the collective charge and spin excitations, respectively, allowing attraction in one channel. In such a way, they have conclude that the system is in a superfluid phase made of singlet pairs of bosons, like a molecular pair-superfluid.

By means of the Lanczos method, it is also possible to study the low-energy spectrum for the spin-1 system in the superfluid regime (allowing the charge degree of freedom). The methodology may be doping the system (with holes) gradually, and with the knowledge of the low-lying excited states as a function of the hopping rate and the coupling constants $g_{0,2}$, one may predict from the dominant excitations the ground state phases of the system in the
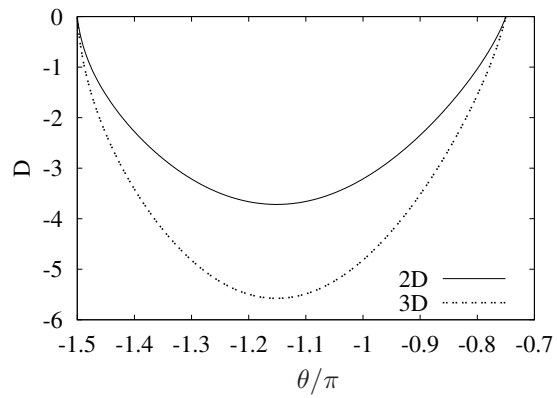
FIGURE 7.2: Extension of the XY-FM to large-D phase transition line, for $-1.5\pi < \theta < -0.8\pi$. Results for 2D and 3D obtained with an effective field theory [132].

thermodynamic limit. One could hence extend the analysis of Ref. [175] to the strongly-correlated regime.

Appendix MPS

A.1 Orthogonality of a MPS

According to the definition of orthogonal matrices, one can show that for any value of k we have

$$\langle \alpha_k | \alpha'_k \rangle = \delta_{\alpha_k \alpha'_k} \qquad \text{and} \qquad \langle \omega_{\alpha_k} | \omega_{\alpha'_k} \rangle = \delta_{\alpha_k \alpha'_k}.$$

Proof. The proof is made by induction, first of all, we should proof that this is true for the first term:

$$\langle \alpha'_2 | \alpha_2 \rangle = \sum_{n_1 n'_1} U^{n'_1 \star}_{\alpha'_2} U^{n_2}_{\alpha_2} \langle n'_1 | n_1 \rangle = \sum_{n_1} U^{n_1 \star}_{\alpha'_2} U^{n_1}_{\alpha_2} = \delta^{\alpha_2}_{\alpha'_2}, \qquad (A.1)$$

since the Fock basis is already an orthonormal basis. Then, we assume that the statement works for the k-th case: $\langle \alpha_k | \alpha'_k \rangle = \delta_{\alpha_k \alpha'_k}$. The last step is to show that the hypothesis is true for the subsequent term: $\langle \alpha'_{s+1} | \alpha_{s+1} \rangle = ?$, where the ket and the bra are given by

$$|\alpha_{s+1}\rangle = \sum_{\alpha_s n_s} U^{n_s}_{\alpha_s \alpha_{s+1}} |\alpha_s\rangle |n_s\rangle \quad \text{and} \quad \langle \alpha'_{s+1}| = \sum_{\alpha'_s n'_s} U^{n'_s \star}_{\alpha'_s \alpha'_{s+1}} |\alpha'_s\rangle |n'_s\rangle. \qquad (A.2)$$

Using Eq. (A.2), we calculate the dot-product by

$$\langle \alpha'_{s+1} | \alpha_{s+1} \rangle = \sum_{\alpha_s n_s} \sum_{\alpha'_s n'_s} U^{n'_s \star}_{\alpha'_s \alpha'_{s+1}} U^{n_s}_{\alpha_s \alpha_{s+1}} \underbrace{\langle \alpha'_s | \alpha_s \rangle}_{\delta^{\alpha_{s+1}}_{\alpha'_{s+1}}} \underbrace{\langle n'_s | n_s \rangle}_{\delta^{n_s}_{n'_s}} \qquad (A.3)$$

$$= \sum_{\alpha_s n_s} U^{n_s \star}_{\alpha_s \alpha'_{s+1}} U^{n_s}_{\alpha_s \alpha_{s+1}} = \delta_{\alpha'_{s+1} \alpha_{s+1}}. \qquad (A.4)$$

Where we were using the fact that $U^\dagger = U^{-1}$ and setting the indices $(n_s, \alpha_s) = \eta_s$, so

$$U^\dagger U = \mathbb{I} = \sum_{n_s \alpha_s} U^\star_{\alpha_{s+1} \alpha_s}{}^{n_s} U^{n_s}_{\alpha_s \alpha'_{s+1}} = \sum_{\eta_s} U^\star_{\alpha_{s+1} \eta_s} U_{\eta_s \alpha'_{s+1}} = \delta_{\alpha'_{s+1} \alpha_{s+1}}. \qquad \square$$

The same proof can be done for the $|\omega_{\alpha_k}\rangle$ states.

The state is orthonormalized in the sense that if all **U**-matrices to the left of some matrix $A^{n_k}_{\alpha_k \alpha_{k+1}}$ are orthogonalized in the left-hand sense, then the basis on the left-hand side of **A** is orthonormal. On the other hand, if all **V**-matrices to the right of $A^{n_k}_{\alpha_k \alpha_{k+1}}$ are orthonormal in the right-hand sense, then the basis of the right-hand side is orthonormal.

A.2   Variational MPS: recursion formulas

The recursion formulas depend on the Hamiltonian under consideration. Here, we consider the Bose-Hubbard Hamiltonian (Eq. 1.6) in a 1D lattice with L sites,

$$\hat{H} = \sum_i \left[-t \left(\hat{b}_i^\dagger \hat{b}_{i+1} + \hat{b}_{i+1}^\dagger \hat{b}_i \right) + \frac{U}{2} \hat{n}_i (\hat{n}_i - 1) - \mu \hat{n}_i \right]. \qquad (A.5)$$

We can describe our system as:
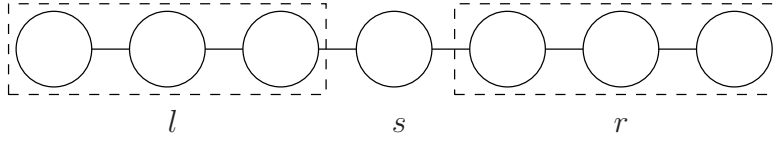
$$\hat{H} = \hat{H}_l + \hat{H}_{ls} + \hat{H}_s + \hat{H}_{sr} + \hat{H}_r, \qquad (A.6)$$

where L is the left part, R the right part of the lattice taking as a reference the site s, each term is defined as

$$
\begin{aligned}
\hat{H}_{\mathrm{l}} &= \sum_{i<s} \left[\frac{U}{2} \hat{n}_i(\hat{n}_i - 1) + -\mu \hat{n}_i \right] - t \sum_{i<s-1} \left[\hat{b}_i^\dagger \hat{b}_{i+1} + \mathrm{h.c.} \right], \\
\hat{H}_{\mathrm{ls}} &= -t \left(\hat{b}_{s-1}^\dagger \hat{b}_s + \mathrm{h.c.} \right), \\
\hat{H}_s &= \frac{U}{2} \hat{n}_s(\hat{n}_s - 1) + (\epsilon_s - \mu) \hat{n}_s, \\
\hat{H}_{sr} &= -t \left(\hat{b}_{s+1}^\dagger \hat{b}_s + \mathrm{h.c.} \right), \\
\hat{H}_{\mathrm{r}} &= \sum_{i>s} \left[\frac{U}{2} \hat{n}_i(\hat{n}_i - 1) + -\mu \hat{n}_i \right] - t \sum_{i>s} \left[\hat{b}_i^\dagger \hat{b}_{i+1} + \mathrm{h.c.} \right].
\end{aligned}
\qquad (A.7)
$$

The expected value of the Hamiltonian is given by

$$
\begin{aligned}
\langle \phi(\mathbb{A}^{\dagger s}) | \hat{H} | \phi(\mathbb{A}^s) \rangle &= \sum A_{\alpha_s \alpha_{s+1}}^{n_s} A_{\alpha_s' \alpha_{s+1}'}^{n_s' \star} \langle \alpha_s' | \langle n_s' | \langle \omega_{\alpha_{s+1}'}' | \hat{H} | \alpha_s \rangle | n_s \rangle | \omega_{\alpha_{s+1}} \rangle \\
&= \sum A_{\alpha_s \alpha_{s+1}}^{n_s} A_{\alpha_s' \alpha_{s+1}'}^{n_s' \star} [\mathcal{H}]_{\alpha_s \alpha_{s+1} n_s}^{\alpha_s' \alpha_{s+1}' n_s'}, \qquad (A.8)
\end{aligned}
$$

where the Hamiltonian matrix is defined as

$$
\begin{aligned}
[\mathcal{H}]_{\alpha_s \alpha_{s+1} n_s}^{\alpha_s' \alpha_{s+1}' n_s'} =& \langle \alpha_s' | \hat{H}_l | \alpha_s \rangle \delta_{n_s}^{n_s'} \delta_{\omega_{\alpha_{s+1}}}^{\omega_{\alpha_{s+1}'}} + \mathrm{Tr}_{\alpha_{s-1}} \left(\mathbb{E}^{s-1}(\hat{I}) \right) \langle n_{s-1}' n_s' | \hat{H}_{ls} | n_{s-1} n_s \rangle \delta_{\omega_{\alpha_{s+1}}}^{\omega_{\alpha_{s+1}'}} \\
&+ \langle n_s' | \hat{H}_s | n_s \rangle \delta_{\alpha_s}^{\alpha_s} \delta_{\omega_{\alpha_{s+1}}}^{\omega_{\alpha_{s+1}'}} + \mathrm{Tr}_{\alpha_{s+2}} \left(\mathbb{E}^{s+1}(\hat{I}) \right) \langle n_s' n_{s+1}' | \hat{H}_{sr} | n_s n_{s+1} \rangle \delta_{\alpha_s}^{\alpha_s} \\
&+ \langle \omega_{\alpha_{s+1}'} | \hat{H}_r | \omega_{\alpha_{s+1}} \rangle \delta_{n_s}^{n_s'} \delta_{\alpha_{s+1}}^{\alpha_{s+1}'}. \qquad (A.9)
\end{aligned}
$$

with

$$\langle n'_s|\hat{H}_s|n_s\rangle = \left[\frac{U}{2}n_s(n_s-1) + (\epsilon_s - \mu)n_s\right]\delta_{n_s}^{n'_s}, \qquad (A.10)$$

and

$$\langle n'_{s-1}n'_s|\hat{H}_{ls}|n_{s-1}n_s\rangle = -t\bigg(\sqrt{n_{s-1}}\sqrt{n_s+1}\delta_{n_{s-1}-1}^{n'_{s-1}}\delta_{n_s+1}^{n'_s}$$

$$+ \sqrt{n_{s-1}+1}\sqrt{n_s}\delta_{n_{s-1}+1}^{n'_{s-1}}\delta_{n_s-1}^{n'_s}\bigg),$$

$$\langle n'_sn'_{s+1}|\hat{H}_{sr}|n_sn_{s+1}\rangle = -t\bigg(\sqrt{n_s}\sqrt{n_{s+1}+1}\delta_{n_s-1}^{n'_s}\delta_{n_{s+1}+1}^{n'_{s+1}}$$

$$+ \sqrt{n_s+1}\sqrt{n_{s+1}}\delta_{n_s+1}^{n'_s}\delta_{n_{s+1}-1}^{n'_{s+1}}\bigg),$$

$$\qquad (A.11)$$

Using the expressions of the Eqs. (2.30), (2.34), the terms $\langle\alpha'_s|\hat{H}_l|\alpha_s\rangle$ and $\langle\omega_{\alpha'_{s+1}}|\hat{H}_r|\omega_{\alpha_{s+1}}\rangle$, assuming $i > s$, contains $\langle\hat{O}_i\rangle$

$$\langle\hat{H}_r\rangle = \delta_{n_s}^{n'_s}\left(\sum_{i>s}\delta_{n_{s+1}}^{n'_{s+1}}\ldots\delta_{n_{i-1}}^{n'_{i-1}}\left\{\langle n'_in'_{i+1}|\hat{H}_{ir}|n_in_{i+1}\rangle + \langle n'_i|\hat{H}_i|n_i\rangle\right\}\right). \qquad (A.12)$$

On the other hand, if $i < s$, $\hat{H}_l$ contains the information about $\langle\hat{O}_i\rangle$,

$$\langle\hat{H}_l\rangle = \left(\sum_{i<s}\left\{\langle n'_{i-1}n'_i|\hat{H}_{li}|n_{i-1}n_i\rangle + \langle n'_i|\hat{H}_i|n_i\rangle\right\}\delta_{n_{i+1}}^{n'_{i+1}}\ldots\delta_{n_{s-1}}^{n'_{s-1}}\right)\delta_{n_s}^{n'_s}. \qquad (A.13)$$

Effective spin models

B.1 Generalized effective model with no external fields

Our starting point is the strongly repulsive Hubbard Hamiltonian model, either for fermions or bosons interacting via s-wave scattering.

B.1.1 Spinless particles

First, we assume that the particles are spinless. The Hamiltonian of this system was reviewed in Chapter 1 in Eq. (1.6).

$$\hat{H} = -t \sum_{\langle i,j \rangle} \hat{b}_i^\dagger b_j + \sum_i \epsilon_i \hat{n}_i + \frac{U}{2} \sum_i \hat{n}_i (\hat{n}_i - 1) = \hat{H}_t + \hat{H}_U, \qquad (B.1)$$

At $t = 0$, the ground state has exactly one particle per site and has an energy of $E_0 = 0$ up to a constant. We want to calculate the ground state in the strong-coupling limit $U \ll t$ in the hard-core regime. To do so, we project into the manifold of only one particle per site, find the effective Hamiltonian acting in this subspace and solve the resulting eigensystem

$$\hat{H}_{eff} \hat{P} |\psi\rangle = \hat{P} |\psi\rangle. \qquad (B.2)$$

We have introduced the one-particle-per-site projector $\hat{P}$. We introduce as well the complementary operator $\hat{Q} = 1 - \hat{P}$. The projectors fulfill $\hat{Q}\hat{P} = \hat{P}\hat{Q} = 0$, $\hat{P}^2 = \hat{P}$ and $\hat{Q}^2 = \hat{Q}$.

Let us start from the eigensystem $\hat{H}|\psi\rangle = E|\psi\rangle$. We use the previous projector properties,

$$\hat{H}|\psi\rangle = E|\psi\rangle \rightarrow \hat{H}(\hat{P} + \hat{Q})|\psi\rangle = E(\hat{P} + \hat{Q})|\psi\rangle. \qquad (B.3)$$

We re-write the previous expression as:

$$-\hat{H}\hat{P}|\psi\rangle = (\hat{H}\hat{Q} - E(\hat{P} + \hat{Q}))|\psi\rangle, \qquad (B.4)$$

and multiply it by $\hat{Q}$ to the left

$$\hat{Q}(-\hat{H}\hat{P})|\psi\rangle = \hat{Q}(\hat{H}\hat{Q} - E\hat{Q})|\psi\rangle = (\hat{Q}\hat{H}\hat{Q} - E)\hat{Q}|\psi\rangle, \qquad (B.5)$$

where we have used that $\hat{Q}^2 = \hat{Q}$. We continue the derivation equating the expression for $\hat{Q}|\psi\rangle$, as follows

$$\hat{Q}|\psi\rangle = -(\hat{Q}\hat{H}\hat{Q} - E)^{-1}\hat{Q}\hat{H}\hat{P}|\psi\rangle,$$
$$\hat{H}\hat{Q}|\psi\rangle = -\hat{H}(\hat{Q}\hat{H}\hat{Q} - E)^{-1}\hat{Q}\hat{H}\hat{P}|\psi\rangle. \tag{B.6}$$

Let us now sum Eq. (B.4) and Eq. (B.6) and operating for $E(\hat{P} + \hat{Q})|\psi\rangle$ we retrieve

$$\hat{H}\hat{P}|\psi\rangle - \hat{H}(\hat{Q}\hat{H}\hat{Q} - E)^{-1}\hat{Q}\hat{H}\hat{P}|\psi\rangle = E(\hat{P} + \hat{Q})|\psi\rangle. \tag{B.7}$$

We multiply the previous expression by $\hat{P}$ at each sides and make use of $\hat{P}^2 = \hat{P}$, in that way we have

$$\left[\hat{P}\hat{H}\hat{P} - \hat{P}\hat{H}(\hat{Q}\hat{H}\hat{Q} - E)^{-1}\hat{Q}\hat{H}\hat{P}\right]\hat{P}|\psi\rangle = E\hat{P}|\psi\rangle,$$
$$\left[\hat{P}\hat{H}\hat{P} - \hat{P}\hat{H}(\hat{P} + \hat{Q})(\hat{Q}\hat{H}\hat{Q} - E)^{-1}\hat{Q}\hat{H}\hat{P}\right]\hat{P}|\psi\rangle = E\hat{P}|\psi\rangle. \tag{B.8}$$

Let us analyze the term $\hat{P}\hat{H}\hat{P} = \hat{P}(\hat{H}_t + \hat{H}_U)\hat{P}$. The part concerning the hopping $\hat{P}\hat{H}_t\hat{P} = 0$, since $\hat{H}_t$ links different occupation manifolds. On the other side $\hat{P}\hat{H}_U\hat{P} = \hat{P}[n_i(n_i - 1)]\hat{P} = 0$, since in the projected state there is exactly one particle per site. Moreover, the terms $\hat{P}\hat{H}_U\hat{Q} = \hat{Q}\hat{H}_U\hat{P}$, since $\hat{H}_U$ keeps the occupation number fixed per site. Thus, we simplify Eq. (B.8) as follows

$$-\hat{P}\hat{H}_t\hat{Q}(\hat{Q}\hat{H}\hat{Q} - E)^{-1}\hat{Q}\hat{H}_t\hat{P}\hat{P}|\psi\rangle = E\hat{P}|\psi\rangle, \tag{B.9}$$

The next step is to calculate the action of $(\hat{Q}\hat{H}\hat{Q} - E)^{-1}$ to the states $\hat{Q}\hat{H}_t\hat{P}\hat{P}|\psi\rangle$. We can consider for very small hopping $t \to 0$,

$$\lim_{t \to 0} = (\hat{Q}\hat{H}\hat{Q} - E)^{-1}\hat{Q}\hat{H}_t\hat{P}\hat{P}|\psi\rangle = (U)^{-1}\hat{Q}\hat{H}_t\hat{P}\hat{P}|\psi\rangle. \tag{B.10}$$

In this limit the ground state energy is not too different from $E_0 = 0$. Therefore, up to second order in t and taking into account that $\hat{P}\hat{H}_t\hat{P} = 0$, Eq. (B.9), up to second order in t, further simplifies as

$$-\hat{P}\hat{H}_t\frac{\hat{Q}}{U}\hat{H}_t\hat{P}\hat{P}|\psi\rangle = -\hat{P}\hat{H}_t\frac{\hat{Q} + \hat{P}}{U}\hat{H}_t\hat{P}\hat{P}|\psi\rangle = -\hat{P}\frac{\hat{H}_t^2}{U}\hat{P}\hat{P}|\psi\rangle = E\hat{P}|\psi\rangle \tag{B.11}$$

Finally, the effective Hamiltonian, using the permutation operator $\hat{\mathbb{P}}$, is written in the following way

$$\hat{H}_{eff} = -\hat{P}\frac{\hat{H}_t^2}{U}\hat{P} = -\frac{2t^2}{U}\sum_{<i,j>}\hat{I}_{ij} \pm \frac{2t^2}{U}\sum_{<i,j>}\hat{\mathbb{P}}_{ij} = \sum_{<i,j>}\hat{H}_{eff}^{ij}, \tag{B.12}$$

where $+$ corresponds to fermions while $-$ to bosons and $\hat{I}$ is the identity operator. And $\hat{H}_{eff}$ is a sum of two-site Hamiltonians.

B.1.2 Spinor systems

In the following, we analyze a system with similar characteristics as the one in the previous section. The main difference is that now we consider particles with internal degrees of freedom. Our aim again is to construct the effective Hamiltonian in the hard-core regime regarding the total spin of the two interacting particles by s-wave scattering.

Let us start with the result of Eq. (B.9) and introduce the two-site projector on the total spin F of the two particles given by $\hat{P}_{ij}(F)$ that fulfill

$$\sum_{F=0}^{2S} \hat{P}_{ij}(F) = 1. \tag{B.13}$$

Introducing the unity of Eq. (B.13) in Eq. (B.9)

$$-\hat{P}\hat{H}_t\hat{Q}(\hat{Q}\hat{H}\hat{Q} - E)^{-1}\hat{Q}\hat{H}_t\hat{P}\hat{P}|\psi\rangle = E\hat{P}|\psi\rangle,$$

$$-\hat{P}\hat{H}_t\hat{Q}(\hat{Q}\hat{H}\hat{Q} - E)^{-1}\hat{Q}\hat{H}_t\hat{P}\left(\sum_{F=0}^{2S}\hat{P}_{ij}(F)\right)\hat{P}|\psi\rangle = E\hat{P}|\psi\rangle,$$

$$-\sum_{F=0}^{2S}\hat{P}\hat{H}_t\frac{\hat{Q}}{U_F}\hat{H}_t\hat{P}\hat{P}_{ij}(F)\hat{P}|\psi\rangle = E\hat{P}|\psi\rangle, \tag{B.14}$$

where we have used the limit of Eq. (B.10) but considering the respective interaction strength U_F for particles colliding with total spin F.

We express $\hat{P}\hat{H}_t^2\hat{P}$ on the projected states, using the permutation operator,

$$\hat{P}\hat{H}_t^2\hat{P} = t^2 \sum_{<i,j>}\left(2\hat{I}_{ij} \pm 2\hat{\mathbb{P}}_{ij}\right). \tag{B.15}$$

Therefore, the two-site effective Hamiltonian is expressed as

$$\hat{H}_{eff}^{ij} = \sum_{F=0}^{2S}\frac{2t^2\left(-\hat{I}_{ij} \pm \hat{\mathbb{P}}_{ij}\right)}{U_F}\hat{P}_{ij}(F), \tag{B.16}$$

where $\hat{\mathbb{P}}_{ij}$ is the permutation operator given by

$$\hat{\mathbb{P}}_{ij} = \sum_{F=0}^{2S}(-\hat{I}_{ij} \pm (-1)^{F+2S})\hat{P}_{ij}(F). \tag{B.17}$$

The property $\hat{P}_{ij}(F')\hat{P}_{ij}(F'') = \delta_{F'F''}\hat{P}_{ij}(F')$ holds, and thus

$$(-\hat{I}_{ij} \pm \hat{\mathbb{P}}_{ij})\hat{P}_{ij}(F) = (-\hat{I}_{ij} \pm (-1)^{F+2S})\hat{P}_{ij}(F), \tag{B.18}$$

where $+$ corresponds to fermions while $-$ to bosons. Finally, the effective Hamiltonian for colliding particles with hyperfine structure is given by

$$\hat{H}_{eff}^{ij} = \sum_{F=0}^{2S} \frac{2t^2}{U_F} \left(-\hat{I}_{ij} \pm (-1)^{F+2S} \right) \hat{P}_{ij}(F), \tag{B.19}$$

and summing over of the pair sites one has

$$\hat{H}_{eff} = \sum_{<i,j>} \sum_{F=0}^{2S} \frac{2t^2}{U_F} \left(-\hat{I}_{ij} \pm (-1)^{F+2S} \right) \hat{P}_{ij}(F). \tag{B.20}$$

Let us consider the action of the neighboring spin operators $\hat{S}_i\hat{S}_j$ acting of the two-site state with total spin F as follows

$$\hat{S}_i\hat{S}_j|\psi(F)\rangle = \frac{1}{2}(F(F+1) - 2S(S+1))|\psi(F)\rangle. \tag{B.21}$$

The projectors can then be expressed in terms of the neighboring spin operators as:

$$\hat{P}_{ij}(F) = \alpha \prod_{s' \neq F} \left[\hat{S}_i\hat{S}_j - \frac{s'(s'+1)}{2} + S(S+1) \right],$$

where the normalization constant α is fixed by   (B.22)

$$\alpha \prod_{s' \neq F} \left[\frac{F(F+1)}{2} + 2S(S+1) - \frac{s'(s'+1)}{2} \right] = 1$$

B.1.3   Examples

As examples, we write the explicit effective Hamiltonian for spin-3/2 fermions and spin-1 bosons, since these are the systems we are interested in.

- Spin-3/2:

  Projectors:

  $$
  \begin{aligned}
  F = 3, \quad &(\hat{S}_i\hat{S}_j)|\psi(F=3)\rangle = \tfrac{9}{4}|\psi(F=3)\rangle \\
  F = 2, \quad &(\hat{S}_i\hat{S}_j)|\psi(F=2)\rangle = -\tfrac{3}{4}|\psi(F=2)\rangle \\
  F = 1, \quad &(\hat{S}_i\hat{S}_j)|\psi(F=0)\rangle = -\tfrac{11}{4}|\psi(F=1)\rangle \\
  F = 0, \quad &(\hat{S}_i\hat{S}_j)|\psi(F=1)\rangle = -\tfrac{15}{4}|\psi(F=0)\rangle
  \end{aligned}
  $$

  $$
  \begin{aligned}
  \hat{P}_{ij}(F=3) &= \alpha_3(\hat{S}_i\hat{S}_j + \tfrac{15}{4})(\hat{S}_i\hat{S}_j + \tfrac{11}{4}) + (\hat{S}_i\hat{S}_j + \tfrac{3}{4}); \quad \alpha_3 = \tfrac{8}{27 \times 25 \times 21} \\
  \hat{P}_{ij}(F=2) &= \alpha_2(\hat{S}_i\hat{S}_j + \tfrac{15}{4})(\hat{S}_i\hat{S}_j + \tfrac{11}{4}) + (\hat{S}_i\hat{S}_j - \tfrac{9}{4}); \quad \alpha_2 = \tfrac{8}{21 \times 19 \times 9} \\
  \hat{P}_{ij}(F=1) &= \alpha_1(\hat{S}_i\hat{S}_j + \tfrac{15}{4})(\hat{S}_i\hat{S}_j + \tfrac{3}{4}) + (\hat{S}_i\hat{S}_j - \tfrac{9}{4}); \quad \alpha_1 = \tfrac{8}{17 \times 11 \times 5} \\
  \hat{P}_{ij}(F=0) &= \alpha_0(\hat{S}_i\hat{S}_j + \tfrac{11}{4})(\hat{S}_i\hat{S}_j + \tfrac{3}{4}) + (\hat{S}_i\hat{S}_j - \tfrac{9}{4}); \quad \alpha_0 = \tfrac{8}{13 \times 9 \times 3}
  \end{aligned}
  $$

Using Eq. (B.20) we may then obtain the effective Hamiltonian:

$$
\hat{H}_{eff} = \sum_{<i,j>} \left[\frac{2t^2}{U_{F=0}} \left(-1 + (-1)^{0+3} \right) \hat{P}_{ij}(0) + \frac{2t^2}{U_{F=1}} \left(-1 + (-1)^{1+3} \right) \hat{P}_{ij}(1) \right.
$$

$$
\left. + \frac{2t^2}{U_{F=2}} \left(-1 + (-1)^{2+3} \right) \hat{P}_{ij}(2) + \frac{2t^2}{U_{F=3}} \left(-1 + (-1)^{3+3} \right) \hat{P}_{ij}(3) \right]
$$

$$
= \sum_{<i,j>} \left[-\frac{4t^2}{g_0} \hat{P}_{ij}(0) - \frac{4t^2}{g_2} \hat{P}_{ij}(2) \right]. \tag{B.23}
$$

Only the channels of $F = 0$ and $F = 2$ have survived, as it is expected for fermions colliding with s-wave scattering.

To write the Hamiltonian in terms of the spin operators, we replace the projectors from the list above.

$$
\hat{H}_{eff} = \sum_{<i,j>} \left[-\frac{4t^2}{g_0} \alpha_0 (\hat{S}_i \hat{S}_j + \frac{11}{4})(\hat{S}_i \hat{S}_j + \frac{3}{4})(\hat{S}_i \hat{S}_j - \frac{9}{4}) \right.
$$

$$
\left. - \frac{4t^2}{g_2} \alpha_2 (\hat{S}_i \hat{S}_j + \frac{15}{4})(\hat{S}_i \hat{S}_j + \frac{11}{4})(\hat{S}_i \hat{S}_j - \frac{9}{4}) \right] \tag{B.24}
$$

- Spin-1:

  Projectors:

  $$
  \begin{array}{ll}
  F = 2, & (\hat{S}_i \hat{S}_j)|\psi(F = 2)\rangle = 1|\psi(F = 2)\rangle \\
  F = 1, & (\hat{S}_i \hat{S}_j)|\psi(F = 0)\rangle = -1|\psi(F = 2)\rangle \\
  F = 0, & (\hat{S}_i \hat{S}_j)|\psi(F = 1)\rangle = -2|\psi(F = 2)\rangle
  \end{array}
  $$

  $$
  \begin{array}{ll}
  \hat{P}_{ij}(F = 2) = \alpha_2 (\hat{S}_i \hat{S}_j + 1)(\hat{S}_i \hat{S}_j + 2); & \alpha_2 = \frac{1}{6} \\
  \hat{P}_{ij}(F = 1) = \alpha_1 (\hat{S}_i \hat{S}_j - 1)(\hat{S}_i \hat{S}_j + 2); & \alpha_1 = \frac{1}{2} \\
  \hat{P}_{ij}(F = 0) = \alpha_0 (\hat{S}_i \hat{S}_j - 1)(\hat{S}_i \hat{S}_j + 1); & \alpha_0 = \frac{1}{3}
  \end{array}
  $$

  We calculate the effective Hamiltonian using Eq. (B.20):

  $$
  \hat{H}_{eff} = \sum_{<i,j>} \left[\frac{2t^2}{U_{F=0}} \left(-1 - (-1)^{0+2} \right) \hat{P}_{ij}(0) + \frac{2t^2}{U_{F=1}} \left(-1 - (-1)^{1+2} \right) \hat{P}_{ij}(1) \right.
  $$

  $$
  \left. + \frac{2t^2}{U_{F=2}} \left(-1 - (-1)^{2+2} \right) \hat{P}_{ij}(2) + \frac{2t^2}{U_{F=3}} \left(-1 - (-1)^{3+2} \right) \hat{P}_{ij}(3) \right]
  $$

  $$
  = \sum_{<i,j>} \left[-\frac{4t^2}{g_0} \hat{P}_{ij}(0) - \frac{4t^2}{g_2} \hat{P}_{ij}(2) \right]
  $$

  $$
  = \sum_{<i,j>} \left[-J_0 \hat{P}_{ij}(0) - J_2 \hat{P}_{ij}(2) \right]. \tag{B.25}
  $$

List of Figures

Bibliography

[1] M. Greiner, O. Mandel, T. Esslinger, T. W. Hansch and I. Bloch, Nature (London) **415**, 39 (2002).

[2] R. Jördens, N. Strohmaier, K. Günter, H. Moritz and T. Esslinger, Nature (London) **455**, 204 (2008).

[3] U. Schneider, L. Hackermuller, S. Will, T. Best, I. Bloch, T. A. Costi, R. W. Helmes, D. Rasch and A. Rosch, Science **322**, 1520 (2008).

[4] B. Paredes, A. Widera, V. Murg, O. Mandel, S. Fölling, I. Cirac, G. V. Shlyapnikov, T. W. Hänsch and I. Bloch, Nature(London) **429**, 277 (2004).

[5] F. Dalfovo, S. Giorgini, L. P. Pitaevskii and S. Stringari, Rev. Mod. Phys. **71**, 463 (1999).

[6] M. Inguscio, S. Stringari and C. E. Wieman, *Bose-Einstein Condensation in Atomic Gases* (IOS Press, Amsterdam, 1999).

[7] A. J. Leggett, Rev. Mod. Phys. **73**, 307 (2001).

[8] C. J. Pethick and H. Smith, *Bose-Einstein Condensation in Dilute Gases* (Cambridge University Press, 2001), ISBN 0-521-66580-9.

[9] L. P. Pitaevskii and S. Stringari, *Bose-Einstein Condensation* (Oxford University Press, Oxford, 2003).

[10] Bose, Zeitschrift für Physik A Hadrons and Nuclei **26**, 178 (1924).

[11] A. Einstein, Sitzungsberichte der Preussischen Akademie der Wissenschaften **3**, 18 (1925).

[12] M. H. Anderson, J. R. Ensher, M. R. Matthews, C. E. Wieman and E. A. Cornell, Science **269**, 198 (1995).

[13] K. B. Davis, M. O. Mewes, M. R. Andrews, N. J. van Druten, D. S. Durfee, D. M. Kurn and W. Ketterle, Phys. Rev. Lett. **75**, 3969 (1995).

[14] C. C. Bradley, C. A. Sackett, J. J. Tollett and R. G. Hulet, Phys. Rev. Lett. **75**, 1687 (1995).

[15] E. A. Cornell and C. E. Wieman, Rev. Mod. Phys. **74**, 875 (2002).

[16] W. Ketterle, Rev. Mod. Phys. **74**, 1131 (2002).

[17] B. DeMarco and D. S. Jin, Science **285**, 1703 (1999).

[18] F. Schreck, L. Khaykovich, K. L. Corwin, G. Ferrari, T. Bourdel, J. Cubizolles and C. Salomon, Phys. Rev. Lett. **87**, 080403 (2001).

[19] A. G. Truscott, K. E. Strecker, W. I. McAlexander, G. B. Partridge and R. G. Hulet, Science **291**, 2570 (2001).

[20] C. J. Myatt, E. A. Burt, R. W. Ghrist, E. A. Cornell and C. E. Wieman, Phys. Rev. Lett. **78**, 586 (1997).

[21] H. T. C. Stoof, M. Houbiers, C. A. Sackett and R. G. Hulet, Phys. Rev. Lett. **76**, 10 (1996).

[22] F. A. van Abeelen, B. J. Verhaar and A. J. Moerdijk, Phys. Rev. A **55**, 4377 (1997).

[23] F. Schreck, G. Ferrari, K. L. Corwin, J. Cubizolles, L. Khaykovich, M.-O. Mewes and C. Salomon, Phys. Rev. A **64**, 011402 (2001).

[24] S. L. Cornish, N. R. Claussen, J. L. Roberts, E. A. Cornell and C. E. Wieman, Phys. Rev. Lett. **85**, 1795 (2000).

[25] E. A. Donley, N. R. Claussen, S. L. Cornish, J. L. Roberts, E. A. Cornell and C. E. Wieman, Nature **412**, 295 (2001).

[26] C. Orzel, A. K. Tuchman, M. L. Fenselau, M. Yasuda and M. A. Kasevich, Science **291**, 2386 (2001).

[27] M. Lewenstein, A. Sanpera, V. Ahufinger, B. Damski, A. Sen and U. Sen, Advances in Physics **56**, 243 (2007).

[28] I. Bloch, J. Dalibard and W. Zwerger, Rev. Mod. Phys. **80**, 885 (2008).

[29] S. Peil, J. V. Porto, B. L. Tolra, J. M. Obrecht, B. E. King, M. Subbotin, S. L. Rolston and W. D. Phillips, Phys. Rev. A **67**, 051603 (2003).

[30] Z. Hadzibabic, S. Stock, B. Battelier, V. Bretin and J. Dalibard, Phys. Rev. Lett. **93**, 180403 (2004).

[31] M. Greiner, I. Bloch, O. Mandel, T. W. Hänsch and T. Esslinger, Phys. Rev. Lett. **87**, 160405 (2001).

[32] H. Moritz, T. Stöferle, M. Köhl and T. Esslinger, Phys. Rev. Lett. **91**, 250402 (2003).

[33] T. Kinoshita, T. Wenger and D. S. Weiss, Science **305**, 1125 (2004).

[34] B. L. Tolra, K. M. O'Hara, J. H. Huckans, W. D. Phillips, S. L. Rolston and J. V. Porto, Phys. Rev. Lett. **92**, 190401 (2004).

[35] D. Jaksch, C. Bruder, J. I. Cirac, C. W. Gardiner and P. Zoller, Phys. Rev. Lett. **81**, 3108 (1998).

[36] J. Hubbard, Proceedings of the Royal Society of London. Series A, Mathematical and Physical Sciences **276**, pp. 238 (1963).

[37] P. W. Anderson, Science **235**, 1196 (1987).

[38] N. W. Ashcroft and N. D. Mermin, *Solid State Physics* (Holt, Rinehardt and Winston, New York, 1976).

[39] M. P. A. Fisher, P. B. Weichman, G. Grinstein and D. S. Fisher, Phys. Rev. B **40**, 546 (1989).

[40] R. J. Glauber, Phys. Rev. **131**, 2766 (1963).

[41] C. Cohen-Tannoudji, B. Diu and F. Laloe, *Quantum Mechanics*, vol. 1 (John Wiley and Sons Inc, 1977).

[42] O. Mandel, *Ph.D. Thesis: Entanglement with quantum gates in an optical lattice.* (Ludwig-Maximilians-Universität Mnchen, Munich, 2005).

[43] S. Fölling, *Ph.D. Thesis: Probing Strongly Correlated States of Ultracold Atoms in Optical Lattices.* (Johannes Gutenberg-Universität, Mainz, 2008).

[44] T. D. Kühner, S. R. White and H. Monien, Phys. Rev. B **61**, 12474 (2000).

[45] O. Penrose and L. Onsager, Phys. Rev. **104**, 576 (1956).

[46] T. Stöferle, H. Moritz, C. Schori, M. Köhl and T. Esslinger, Phys. Rev. Lett. **92**, 130403 (2004).

[47] I. B. Spielman, W. D. Phillips and J. V. Porto, Phys. Rev. Lett. **98**, 080404 (2007).

[48] J. M. Kosterlitz and D. J. Thouless, Journal of Physics C: Solid State Physics **6**, 1181 (1973).

[49] J. M. Kosterlitz, Journal of Physics C: Solid State Physics **7**, 1046 (1974).

[50] D. S. Rokhsar and B. G. Kotliar, Phys. Rev. B **44**, 10328 (1991).

[51] H. Yokoyama and H. Shiba, J. Phys. Soc. Jpn. **56**, 1490 (1987).

[52] R. Jördens, L. Tarruell, D. Greif, T. Uehlinger, N. Strohmaier, H. Moritz, T. Esslinger, L. De Leo, C. Kollath, A. Georges, V. Scarola, L. Pollet, E. Burovski, E. Kozik and M. Troyer, Phys. Rev. Lett. **104**, 180401 (2010).

[53] P. Medley, D. M. Weld, H. Miyake, D. E. Pritchard and W. Ketterle, arXiv: **1006.4674** (2010).

[54] W. Heisenberg, Zeitschrift für Physik **49**, 619 (1928).

[55] D. M. Stamper-Kurn, M. R. Andrews, A. P. Chikkatur, S. Inouye, H.-J. Miesner, J. Stenger and W. Ketterle, Phys. Rev. Lett. **80**, 2027 (1998).

[56] E. Altman, E. Demler and M. D. Lukin, Phys. Rev. A **70**, 013603 (2004).

[57] S. Fölling, F. Gerbier, A. Widera, O. Mandel, T. Gericke and I. Bloch, Nature **434**, 481 (2005).

[58] T. Rom, T. Best, D. van Oosten, U. Schneider, S. Flling, B. Paredes and I. Bloch, Nature **444**, 733 (2006).

[59] M. Schellekens, R. Hoppeler, A. Perrin, J. V. Gomes, D. Boiron, A. Aspect and C. I. Westbrook, Science **310**, 648 (2005).

[60] M. Lewenstein, Nature **445**, 372 (2007).

[61] A. Öttl, S. Ritter, M. Köhl and T. Esslinger, Phys. Rev. Lett. **95**, 090404 (2005).

[62] A. M. Rey, V. Gritsev, I. Bloch, E. Demler and M. D. Lukin, Phys. Rev. Lett. **99**, 140601 (2007).

[63] K. Eckert, O. Romero-Isart, M. Rodriguez, M. Lewenstein, E. S. Polzik and A. Sanpera, Nat. Phys. **4**, 50 (2008).

[64] R. W. Cherng and E. Demler, New Journal of Physics **9**, 7 (2007).

[65] T.-L. Ho, Phys. Rev. Lett. **81**, 742 (1998).

[66] F. Zhou and M. Snoek, Ann. Phys. **308**, 692 (2003).

[67] T. Ohmi and K. Machida, J. Phys. Soc. Jpn. **67**, 1822 (1998).

[68] A. Imambekov, M. Lukin and E. Demler, Phys. Rev. A **68**, 063602 (2003).

[69] J. Stenger, S. Inouye, D. M. Stamper-Kurn, H.-J. Miesner, A. P. Chikkatur and W. Ketterle, Nature **396**, 345 (1998).

[70] C. V. Ciobanu, S.-K. Yip and T.-L. Ho, Phys. Rev. A **61**, 033607 (2000).

[71] M. D. Barrett, J. A. Sauer and M. S. Chapman, Phys. Rev. Lett. **87**, 010404 (2001).

[72] E. Demler and F. Zhou, Phys. Rev. Lett. **88**, 163001 (2002).

[73] S. K. Yip, Phys. Rev. Lett. **90**, 250402 (2003).

[74] A. Imambekov, M. Lukin and E. Demler, Phys. Rev. Lett. **93**, 120405 (2004).

[75] M. Snoek and F. Zhou, Phys. Rev. B **69**, 094410 (2004).

[76] M. Rizzi, D. Rossini, G. De Chiara, S. Montangero and R. Fazio, Phys. Rev. Lett. **95**, 240404 (2005).

[77] K. Harada, N. Kawashima and M. Troyer, J. Phys. Soc. Jpn. **76**, 013703 (2007).

[78] M.-C. Chung and S. Yip, Phys. Rev. A **80**, 053615 (2009).

[79] N. Papanicolaou, Nucl. Phys. B **305**, 367 (1988).

[80] A. V. Chubukov, J. Phys.: Condens. Matter **2**, 1593 (1990).

[81] A. V. Chubukov, Phys. Rev. B **43**, 3337 (1991).

[82] G. Fáth and J. Sólyom, Phys. Rev. B **51**, 3620 (1995).

[83] C. D. Batista, G. Ortiz and J. E. Gubernatis, Phys. Rev. B **65**, 180402 (2002).

[84] M.-S. Chang, C. D. Hamley, M. D. Barrett, J. A. Sauer, K. M. Fortier, W. Zhang, L. You and M. S. Chapman, Phys. Rev. Lett. **92**, 140403 (2004).

[85] H. Schmaljohann, M. Erhard, J. Kronjäger, M. Kottke, S. van Staa, L. Cacciapuoti, J. J. Arlt, K. Bongs and K. Sengstock, Phys. Rev. Lett. **92**, 040402 (2004).

[86] L. E. Sadler, J. M. Higbie, S. R. Leslie, M. Vengalattore and D. M. Stamper-Kurn, Nature (London) **443**, 312 (2006).

[87] C. Klempt, O. Topic, G. Gebreyesus, M. Scherer, T. Henninger, P. Hyllus, W. Ertmer, L. Santos and J. J. Arlt, Phys. Rev. Lett. **103**, 195302 (2009).

[88] T. Lahaye, T. Koch, B. Frohlich, M. Fattori, J. Metz, A. Griesmaier, S. Giovanazzi and T. Pfau, Nature **448**, 672 (2007).

[89] F. Deuretzbacher, G. Gebreyesus, O. Topic, M. Scherer, B. Lücke, W. Ertmer, J. Arlt, C. Klempt and L. Santos, Phys. Rev. A **82**, 053608 (2010).

[90] A. Widera, F. Gerbier, S. Fölling, T. Gericke, O. Mandel and I. Bloch, Phys. Rev. Lett. **95**, 190405 (2005).

[91] A. Widera, F. Gerbier, S. Flling, T. Gericke, O. Mandel and I. Bloch, New Journal of Physics **8**, 152 (2006).

[92] F. Gerbier, A. Widera, S. Fölling, O. Mandel and I. Bloch, Phys. Rev. A **73**, 041602 (2006).

[93] L. Santos, M. Fattori, J. Stuhler and T. Pfau, Phys. Rev. A **75**, 053606 (2007).

[94] P. O. Fedichev, Y. Kagan, G. V. Shlyapnikov and J. T. M. Walraven, Phys. Rev. Lett. **77**, 2913 (1996).

[95] D. J. Papoular, G. V. Shlyapnikov and J. Dalibard, Phys. Rev. A **81**, 041603 (2010).

[96] W. Hofstetter, J. I. Cirac, P. Zoller, E. Demler and M. D. Lukin, Phys. Rev. Lett. **89**, 220407 (2002).

[97] T. Paananen, J.-P. Martikainen and P. Törmä, Phys. Rev. A **73**, 053606 (2006).

[98] A. N. Wenz, T. Lompe, T. B. Ottenstein, F. Serwane, G. Zürn and S. Jochim, Phys. Rev. A **80**, 040702 (2009).

[99] G. Modugno, F. Ferlaino, R. Heidemann, G. Roati and M. Inguscio, Phys. Rev. A **68**, 011601 (2003).

[100] L.-W. He, C. E. Burkhardt, M. Ciocca, J. J. Leventhal and S. T. Manson, Phys. Rev. Lett. **67**, 2131 (1991).

[101] T. Weber, J. Herbig, M. Mark, H.-C. Nagerl and R. Grimm, Science **299**, 232 (2003).

[102] T. Fukuhara, Y. Takasu, M. Kumakura and Y. Takahashi, Phys. Rev. Lett. **98**, 030401 (2007).

[103] M. A. Cazalilla, A. F. Ho and M. Ueda, New Journal of Physics **11**, 103033 (2009).

[104] C. Honerkamp and W. Hofstetter, Phys. Rev. Lett. **92**, 170403 (2004).

[105] C. Wu, J.-p. Hu and S.-c. Zhang, Phys. Rev. Lett. **91**, 186402 (2003).

[106] C. Wu, Phys. Rev. Lett. **95**, 266404 (2005).

[107] C. Wu, Mod. Phys. Lett. B **20**, 1707 (2006).

[108] P. Lecheminant, E. Boulat and P. Azaria, Phys. Rev. Lett. **95**, 240402 (2005).

[109] D. Controzzi and A. M. Tsvelik, Phys. Rev. Lett. **96**, 097205 (2006).

[110] H.-H. Tu, G.-M. Zhang and L. Yu, Phys. Rev. B **74**, 174404 (2006).

[111] K. Eckert, . Zawitkowski, M. J. Leskinen, A. Sanpera and M. Lewenstein, New Journal of Physics **9**, 133 (2007).

[112] G. Vidal, Phys. Rev. Lett. **91**, 147902 (2003).

[113] M. Troyer, F. Alet, S. Trebst and S. Wessel, AIP Conference Proceedings **690**, 156 (2003).

[114] F. Alet, P. Dayal, A. Grzesik, A. Honecker, M. Körner, A. Läuchli, S. R. Manmana, I. P. McCulloch, F. Michel, R. M. Noack, G. Schmid, U. Schollwöck, F. Stöckli, S. Todo, S. Trebst, M. Troyer, P. Werner and S. W. collaboration, J. Phys. Soc. Jpn. **74S**, 30 (2005).

[115] S. R. White and R. M. Noack, Phys. Rev. Lett. **68**, 3487 (1992).

[116] S. R. White, Phys. Rev. Lett. **69**, 2863 (1992).

[117] S. R. White, Phys. Rev. B **48**, 10345 (1993).

[118] U. Schollwöck, Rev. Mod. Phys. **77**, 259 (2005).

[119] G. Vidal, Phys. Rev. Lett. **93**, 040502 (2004).

[120] F. Verstraete, D. Porras and J. I. Cirac, Phys. Rev. Lett. **93**, 227205 (2004).

[121] F. Verstraete, J. J. García-Ripoll and J. I. Cirac, Phys. Rev. Lett. **93**, 207204 (2004).

[122] F. Verstraete and J. I. Cirac, Phys. Rev. B **73**, 094423 (2006).

[123] S. Östlund and S. Rommer, Phys. Rev. Lett. **75**, 3537 (1995).

[124] A. E. Feiguin and S. R. White, Phys. Rev. B **72**, 220401 (2005).

[125] G. Vidal, Phys. Rev. Lett. **98**, 070201 (2007).

[126] D. Porras, F. Verstraete and J. I. Cirac, Phys. Rev. B **73**, 014410 (2006).

[127] V. E. Korepin, Phys. Rev. Lett. **92**, 096402 (2004).

[128] E. Schmidt, Math. Ann. **63**, 433 (1907).

[129] M. Suzuki, Physics Letters A **146**, 319 (1990).

[130] E. Dagotto, Rev. Mod. Phys. **66**, 763 (1994).

[131] K. Rodríguez, A. Argüelles, M. Colomé-Tatché, T. Vekua and L. Santos, Phys. Rev. Lett. **105**, 050402 (2010).

[132] K. Rodriguez, A. Argüelles, A. K. Kolezhuk, L. Santos and T. Vekua, arXiv: **1009.3875** (2010).

[133] P. Calabrese and J. Cardy, Phys. Rev. Lett. **96**, 136801 (2006).

[134] M. A. Cazalilla, Phys. Rev. Lett. **97**, 156403 (2006).

[135] M. Rigol, V. Dunjko, V. Yurovsky and M. Olshanii, Phys. Rev. Lett. **98**, 050405 (2007).

[136] C. Kollath, A. M. Läuchli and E. Altman, Phys. Rev. Lett. **98**, 180601 (2007).

[137] S. R. Manmana, S. Wessel, R. M. Noack and A. Muramatsu, Phys. Rev. Lett. **98**, 210405 (2007).

[138] A. M. Läuchli and C. Kollath, J. Stat. Mech.: Theory Exp. p. P05018 (2008).

[139] M. Moeckel and S. Kehrein, Phys. Rev. Lett. **100**, 175702 (2008).

[140] S. R. Manmana, S. Wessel, R. M. Noack and A. Muramatsu, Phys. Rev. B **79**, 155104 (2009).

[141] T. Kinoshita, T. Wenger and D. S. Weiss, Nature (London) **440**, 900 (2006).

[142] P. B. Blakie and J. V. Porto, Phys. Rev. A **69**, 013603 (2004).

[143] A. M. Rey, G. Pupillo and J. V. Porto, Phys. Rev. A **73**, 023608 (2006).

[144] L. Pollet, C. Kollath, K. van Houcke and M. Troyer, New J. Phys. **10**, 065001 (2008).

[145] A. Polkovnikov and V. Gritsev, Nat. Physics **4**, 477 (2008).

[146] A. J. Leggett, Rev. Mod. Phys. **73**, 307 (2001).

[147] W.-L. You, Y.-W. Li and S.-J. Gu, Phys. Rev. E **76**, 022101 (2007).

[148] C. Klempt, O. Topic, G. Gebreyesus, M. Scherer, T. Henninger, P. Hyllus, W. Ertmer, L. Santos and J. J. Arlt, Phys. Rev. Lett. **104**, 195303 (2010).

[149] B. Sutherland, Phys. Rev. B **12**, 3795 (1975).

[150] A. V. Gorshkov, M. Hermele, V. Gurarie, C. Xu, P. S. Julienne, J. Ye, P. Zoller, E. Demler, M. D. Lukin and A. M. Rey, Nature Physics **6**, 289 (2010).

[151] L. Gerland, L. Frankfurt, M. Strikman, H. Stöcker and W. Greiner, Phys. Rev. Lett. **81**, 762 (1998).

[152] J. H. Van Vleck, Phys. Rev. **33**, 467 (1929).

[153] J. J. García-Ripoll, M. A. Martin-Delgado and J. I. Cirac, Phys. Rev. Lett. **93**, 250405 (2004).

[154] I. Affleck, T. Kennedy, E. H. Lieb and H. Tasaki, Phys. Rev. Lett. **59**, 799 (1987).

[155] J. Damerau and A. Kümper, Journal of Statistical Mechanics: Theory and Experiment **2006**, P12014 (2006).

[156] L. A. Takhtajan, Physics Letters A **87**, 479 (1982), ISSN 0375-9601.

[157] H. M. Babujian, Physics Letters A **90**, 479 (1982), ISSN 0375-9601.

[158] A. Klümper, EPL (Europhysics Letters) **9**, 815 (1989).

[159] M. N. Barber and M. T. Batchelor, Phys. Rev. B **40**, 4621 (1989).

[160] A. Kolezhuk, Phys. Rev. B **78**, 144428 (2008).

[161] G. Wellein, H. Fehske and A. P. Kampf, Phys. Rev. Lett. **81**, 3956 (1998).

[162] K. Okamoto and K. Nomura, Physics Letters A **169**, 433 (1992).

[163] A. Argüelles, *Ph.D. Thesis: Multicomponent gases in 1D optical lattices* (Leibniz Universität Hannover, 2010).

[164] T. Itakura and N. Kawakami, J. Phys. Soc. Jpn. **64**, 2321 (1995).

[165] T. Giamarchi, *Quantum Physics in One Dimension* (Oxford University Press, 2003).

[166] Y. Yamashita, N. Shibata and K. Ueda, Phys. Rev. B **58**, 9114 (1998).

[167] A. Klümper and D. C. Johnston, Phys. Rev. Lett. **84**, 4701 (2000).

[168] B. Frischmuth, F. Mila and M. Troyer, Phys. Rev. Lett. **82**, 835 (1999).

[169] B. A. Ivanov and A. K. Kolezhuk, Phys. Rev. B **68**, 052401 (2003).

[170] Y.-A. Trotzky, Stefan andChen, U. Schnorrberger, P. Cheinet and I. Bloch, arXiv: **1009.2415** (2010).

[171] P. Calabrese and J. Cardy, Journal of Statistical Mechanics: Theory and Experiment **2004**, P06002 (2004).

[172] L. Tagliacozzo, T. R. de Oliveira, S. Iblisdir and J. I. Latorre, Phys. Rev. B **78**, 024410 (2008).

[173] T. Vekua and A. Honecker, Phys. Rev. B **73**, 214427 (2006).

[174] T. Senthil, A. Vishwanath, L. Balents, S. Sachdev and M. P. A. Fisher, Science **303**, 1490 (2004).

[175] F. H. L. Essler, G. V. Shlyapnikov and A. M. Tsvelik, Journal of Statistical Mechanics: Theory and Experiment **2009**, P02027 (2009).

Acknowledgements

Lovely thanks I would like to give also to my parents, Cecilia and Mario and my brother Javier. Although geographically far from here, their love and support were always the biggest stimulus. *You are closer to me than you think, you live in my heart.*

Curriculum Vitae

Address	: Marienstr. 7, 30171 Hannover, Germany
Phone	: +49(0)511 762 4836(office)
	+49(0)176 93110854(mobile)
Email	: karen.rodriguez@itp.uni-hannover.de
Homepage	: http://www.itp.uni-hannover.de/karen/

Personal profile

Date of Birth	: 1st November 1980
Place of Birth	: Bogotá, Colombia
Gender	: Female
Marital Status	: Married
Nationality	: Colombian
Language	: Spanish, English

Education

2007 - 2010	PhD
	Leibniz Hannover University, Hannover, Germany
2005 - 2006	Master of science - Physics
	Stuttgart University, Stuttgart, Germany
1998 - 2004	B. Sc. Physics
	National University of Colombia, Bogotá, Colombia
1989 - 1997	Primary and Secondary school
	Nuestra Señora del Buen Consejo, Bogotá, Colombia

List of publications

1. K. Rodríguez, A. Argüelles, A. K. Kolezhuk, L. Santos and T. Vekua, *Field-induced phase transitions of repulsive spin-1 bosons in optical lattices*, arXiv:1009.3875v1 [cond-mat.quant-gas] (2010).

2. K. Rodríguez, A. Argüelles, M. Colomé-Tatché, T. Vekua and L. Santos, *Mott-Insulator Phases of Spin-3/2 Fermions in the Presence of Quadratic Zeeman Coupling*, Phys. Rev. Lett. **105**, 050402 (2010).

3. K. Rodríguez, A. Argüelles and L. Santos, *Correlation dynamics of strongly-correlated bosons in time-dependent optical lattices*, arXiv:0905.3312 [cond-mat.quant-gas] (2009).

Other publications of the author:

1. S. Manmana, K. Rodríguez, S. Wessel, and A. Muramatsu, *Simulations of Strongly Correlated Quantum Systems out of Equilibrium*, High Performance Computing in Science and Engineering 2007, Springer (2007).

2. K. Rodríguez, S. R. Manmana, M. Rigol, R. M. Noack, and A. Muramatsu, *Coherent matter waves emerging from Mott-insulators*, Invited paper to a special issue on Cold Atoms in Optical Lattices, New J. Phys. 8, 169 (2006), cond-mat/0606155.

3. K. Rodríguez, A. M. Guzmn, *Beam propagation in magnetic atomic guides*, Proc. SPIE, Vol. 5622, 486 (2004), SPIE Vol. 5622.

4. K. Rodríguez, A. M. Guzmn, *Beam propagation in a symmetric magnetic atomic guide*, Frontiers in Optics, OSA(2004), paper FWH20, FiO 2004/LS XX.

Selbstständigkeitserklärung

Hiermit versichere ich, die vorliegende Doktorarbeit selbstständig und unter ausschließlicher Verwendung der angegebenen Hilfsmittel angefertigt zu haben.

Hannover, den 02. Februar 2011

_____

Karen Rodríguez